Radio Measurement of Extensive Air Showers at the Pierre Auger Observatory

Event Selection and Reconstruction comparison

Masterarbeit
zur Erlangung des akademischen Grades
Master of Science

dem Fachbereich Physik
der Bergischen Universität Wuppertal

vorgelegt von
Jens Neuser

22. Dezember 2010

Betreuender Professor:	Prof. Karl-Heinz Kampert
Zweitkorrektor:	Prof. Klaus Helbing

Contents

Chapter 1

Introduction

Since the detection of cosmic rays about one century ago, scientists from all over the world are trying to find answers on the fundamental questions they arise. Where do they come from? How do they reach the highest energies? Although we are bombarded by thousands of them every second, these and several other questions are not understood in detail or at all. Measuring the particle flux, the arrival directions and the composition is of central importance to get a hint of the answers. Gaining more insight to this subject would also lead to a better understanding of the high energy Universe.
In this context the Piere Auger Observatory has been conceived to study extensive air showers induced by primary particles at energies above 10^{18} eV in order to solve the mystery of the origin and nature of the highest energy particles. Its design combines the most advanced detection techniques and the largest exposure, to provide high quality data at the same time with unprecedented statistics. The surface detectors are used to study secondary particles and their lateral distribution at ground level, whereas the fluorescence detectors, measuring light coming from nitrogen molecules, excited by shower particles, can be used for reconstruction of the longitudinal shower development and energy deposit. The synergy of these techniques is able to reduce systematic uncertainties, improves the reconstruction and provides the possibility for cross-checking the gathered information.
A new, revived detection technique is currently under construction at the observatory, making it a super-hybrid-detector. The Auger Engineering Radio Array will provide additional information by measuring the radio emission of air showers in the MHz range. Also the Wuppertal astroparticle group is involved in this new project, mostly contributing to monitoring issues and analysis purposes. This work is focused on analysis of data coming from a former test setup at the observatory site which was used for R&D. It is shown that by improvement of the reconstruction and event selection for the surface detectors a large gain in statistics can be achieved, leading to a better understanding of the gathered information of coincident radio events. Also some results of first studies with the radio data itself are presented.

The second chapter gives an introduction to some important aspects of cosmic ray physics including a part focused on air showers. The physics behind radio emission is discussed by visiting two different model approaches and showing some simulation results. Chapter 3 yields a brief summary of the Pierre Auger Observatory and its detectors. The Auger Engineering Radio Array is introduced, giving a short motivation and an overview of the setup components. In chapter 4 the main analysis framework OffLine is presented with a short preface on the reconstruction algorithms for surface detectors and radio. Chapter 5 shows the changes made for improving the event selection process and compares the results of different surface detector reconstructions. Also the results of the analysis of radio events in coincidence with the surface detector are presented. Chapter 6 deals with basic studies of the stand-alone data from the radio test setup. Additionally some first results of the data taken with the Auger Radio Engineering Array are shown. The last chapter yields a summary and some conclusions as well as suggestions for further analysis.

Chapter 2

Cosmic rays

The long history of astroparticle physics started almost a century ago due to an experiment by the Austrian physicist Victor Franz Hess. In August 1912 he started a balloon ascent to measure the ionization of the atmosphere at different heights. Up to then most of the ionization was traced to radioactive effects inside the Earth. Using an improved detector, in that case an electroscope, Hess wanted to demonstrate the decrease of the ionization effect with increasing distance from the ground. The result was quite irritating. Up to a height of around 1000 meters he could measure the decrease almost as expected, but going to higher altitudes the amount of ionization started to rise again up to a maximum at about 3000 meters. At this height the effect was as strong as on the Earth surface. As his measurement was explainable in no way with the normal radioactivity of the Earth, Hess concluded that the atmosphere must be penetrated by some unknown energetic radiation from outer space and called it „Höhenstrahlung“ [Hes12]. This discovery was decorated with the nobel price in physics in 1936.

Dimitry Skobelzyn was the first to detect secondary particles of the cosmic radiation using a cloud chamber in 1927. In subsequent experiments with these secondaries the thitherto unknown positrons (1932), muons (1936) and pions (1947) were discovered. In the year 1938 the French physicist Pierre Victor Auger started an experiment in the Swiss Alps. Putting several detectors at a distance of roughly 300 m to each others, he measured coincident events in neighbouring stations and hence stated the existence of „extensive air showers“ induced by cosmic rays hitting nuclei in the upper atmosphere [Aug39].

In 1965 John Jelley et al. discovered the radio emission of extensive air showers [Jel65] by using 72 dipole antennas triggered by a simple array of three Geiger-Müller counters. Inspired by theories of Askaryan about Cherenkov radiation of electrons and positrons in air showers [Ask62] he measured strongly pulsed emission at frequencies around 44 MHz which were initiated by high-energy cosmic rays.

2.1 Energy spectrum and composition

One of the most discussed quantities of cosmic rays is the energy spectrum which can be used as a probe for various properties of the primary particles. The spectrum has been measured over 11 decades in energy with a flux spanning more than 30 orders of magnitudes. It can be described very well by a simple power law

$$\frac{dN}{dE} \propto E^{-\alpha}. \tag{2.1}$$

The flux drops rapidly from about one particle per m^2 per second at around 100 GeV to one particle per km^2 per year above 10 EeV (see Fig. 2.1).

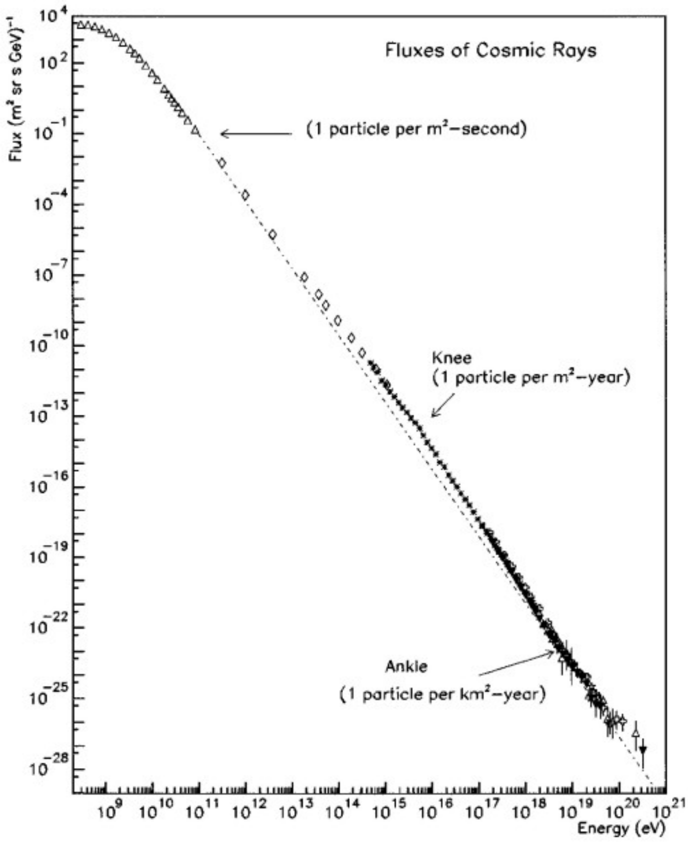

Figure 2.1: All particle spectrum of the cosmic rays [CSG97].

The first feature of this spectrum appears at approximately $3{\cdot}10^{15}$ eV where the index decreases from $\alpha \approx 2.6$ below this energy to $\alpha \approx 3$ resulting in a steeper spectrum, the so called „knee". There are several indications for a further steepening, which is named the „second knee", with an index of $\alpha \approx 3.3$ at energies of about $5{\cdot}10^{17}$ eV [Bir93]. At roughly

10^{19} eV a very pronounced flattening with $\alpha \approx 2.7$ appears, which is called the „ankle“. Up to these energies cosmic rays are believed to be mainly of galactic origin, whereas the appearance of the ankle is interpreted as the rise of domination of extragalactic cosmic-rays. But there is still a need of more high-quality data to seperate between different scenarios as the point and description of this transition is heavily model dependent. The last feature of the spectrum is an overall cut-off at highest energies (E $> 10^{20}$ eV), the so called GZK-effect, which might be already visible in the scaled flux spectra measured by different experiments (see Fig. 2.2), but can not be proclaimed as discovered due to the large uncertainties which arise from the limited exposure. This effect will be discussed in more detail in section 2.3.

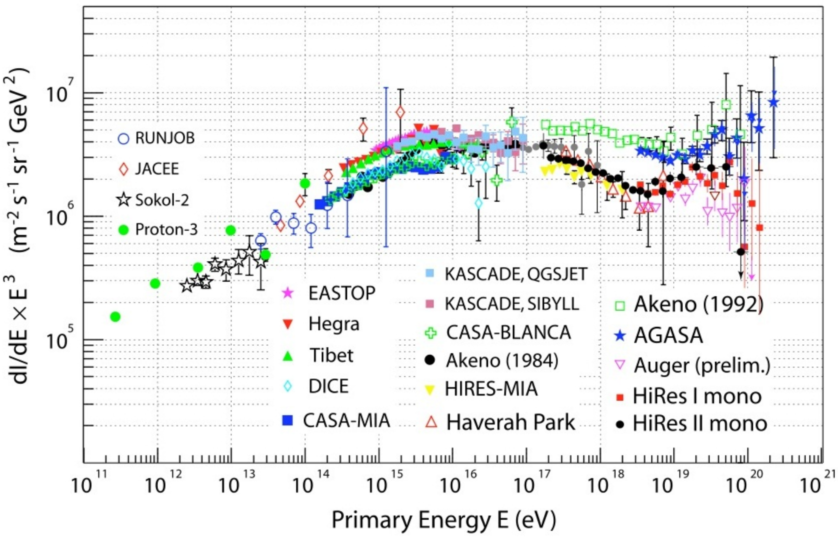

Figure 2.2: Primary flux of cosmic rays scaled with E^3 [Kam07].

An interesting property of the cosmic rays is the chemical composition of the primaries (maybe also as a function of energy). Comparing the actual measured composition with the abundance of elements in the stellar material (see Fig. 2.3) the agreement is quite good. Nevertheless there are some differences which could be discussed. One is the over-abundance of Hydrogen and Helium in the solar matter which might correspond to the overabundance of Lithium, Beryllium and Boron in cosmic rays. This can be understood by the propagation of the cosmic rays through the interstellar space. Assuming an equivalent composition of solar matter at the origin they can interact with gas or dust particles which could force a spallation into lighter nuclei.

The mass composition of the cosmic rays at very high energies is also important to manifest the origin of the ankle in the energy spectrum. Berezinsky proposed a model with pure proton composition in this energy range [Ber04], where the dip is due to e^+e^--pair production of extragalactic protons hitting the cosmic microwave background. Going from

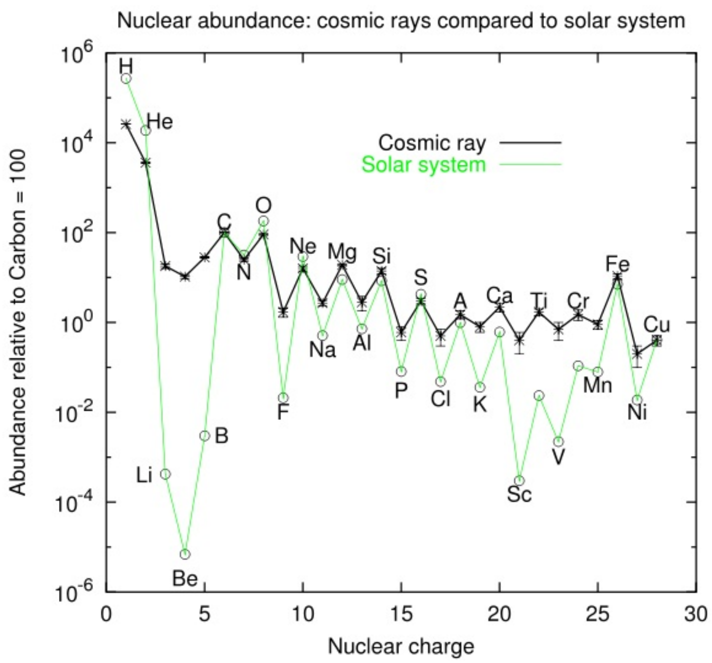

Figure 2.3: Relative abundance of elements for solar material and cosmic rays [GS05].

galactic to extragalactic origin could be the explanation for a change in the composition from heavier to light nuclei.

2.2 Origin of cosmic rays

One of the most striking, but also most challenging question in the research of astroparticles is the question on the possible sources of ultra high energy cosmic rays (UHECRs). Both, experimentalists and theorists, have proposed several ideas to explain these energies, but the model building is not so easy, as the acceleration of particles needs more and more time, increasing potentials or more space. There are two theoretical approaches, containing several models themselves, which adress this crucial question.

The first class, the so-called „top-down“ models, explains the UHECRs by a production process via decay of very massive particles. These massive particles could be a relict from the early Universe or emitted by a defect in the early Universe. Other models deal with predictions of super-symmetric (SUSY) particles or non-standard neutrinos. All these models have in common that the high energy source is nearby which results in a reduced interaction probability with the cosmic microwave background (CMB) or interstellar matter.

Instead the second class of theories, consistently called „bottom-up“, uses the standard model of particle physics for explanation. Classic extra-galactic sources as gamma ray bursts (GRB) or active galactic nuclei (AGN) are considered as producers and accelerators of UHECRs with the acceleration itself taking place in strong shocks contained in moving magnetized plasma. These sources will be focused in the next subsection.

2.2.1 Astrophysical sources

As already mentioned the acceleration of cosmic rays demands the interplay of several components as space, potential, etc. Therefore, the maximum energy of a particle can be estimated by requiring that the complete gyro-radius of the particle is contained in the specific region of acceleration:

$$\left(\frac{E_{max}}{EeV}\right) = \frac{1}{2} Z \cdot \beta \cdot \left(\frac{B}{\mu G}\right) \cdot \left(\frac{R}{kpc}\right) \tag{2.2}$$

with Z being the charge of the particle, β its velocity, B the magnetic field in and R the size of the acceleration region which holds for strong shocks and/or for relativistic particles. The Hillas plot in Fig. 2.4 shows the dependencies of the maximal achievable energy of astrophysical sources with respect to size and magnetic field. It is clearly visible that one either needs a large field or a huge size of the acceleration region. Only a few astronomical objects satisfy this conditions and could be candidates for accelerating particles up to 10^{20} eV.

A short characterization:

- *Active Galactic Nuclei (AGN):* One of the most favoured sources of UHECRs. Having a typical size of $R \approx 10^{-2}$ pc and a magnetic field of $B \approx 5$ G they fulfill the criteria for pushing protons up to the highest energies. They purchase their power by accreting matter into a supermassive black hole with about $10^6 - 10^8$ solar masses. Unfortunately there is also a huge energy loss in regions of high field density which limits the maximum energy for protons and prohibits the escape of heavier nuclei at all. Considering AGNs as sources one can look for anistropies in the arrival direction of CRs and correlate them with the position of nearby AGNs. This was done e.g. with data from the Pierre Auger Observatory (see [Pie07a] & [Pie10b]).

- *Gamma Ray Bursts (GRBs):* The collapse of a massive star or the merging of black holes could be a possible explantion for the detected huge bursts of gamma rays up to GeV energies. These gamma rays are emitted via synchroton radiation and inverse Compton scattering by highly relativistic electrons. Therefore, it is necessary to accelerate electrons and also protons to the highest energies. The energy release

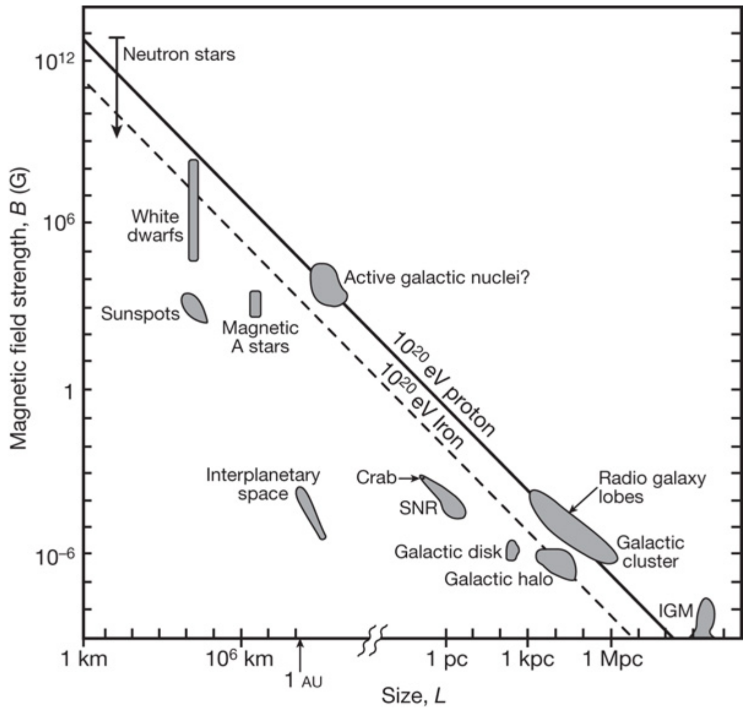

Figure 2.4: Hillas plot: Possible accelerator candidates for particles with their size and magnetic field. Objects below the lines can not accelerate the indicated particles to the given energy of $E = 10^{20}$ eV [BM09].

in the burst time is consistent with the required luminosity for cosmic rays above 10^{19} eV. But also here a limitiation, namely the huge distance of GRBs (up to $z = 5$), gives constraints on this model.

- *Neutron stars:* Rotating neutron stars or pulsars could accelerate particles to very high energies. For a magnetic field of $B \approx 10^{12}$ G, a star radius of $R \approx 10$ km and an angular velocity of about 50 Hz we end up with a maximal energy of about 10^{18} eV.

2.2.2 Acceleration models

As we have a list of several candidates for the acceleration of UHECRs now, we will discuss the acceleration mechanism itself in this section. In 1949 Fermi postulated a method to accelerate particles to the highest energies generating an energy spectrum which follows a power law [Fer49]. Considering a test particle with energy E traveling through interstellar space and colliding with objects like magnetic clouds gaining an average amount $\Delta E = \xi E$ with every „hit". Starting with an energy E_0 the particle's energy after n hits is

$$E_n = E_0(1+\xi)^n \tag{2.3}$$

$$n = \frac{ln(E_n/E_0)}{ln(1+\xi)} \tag{2.4}$$

If we now assume a probability P_{esc} for this particle to escape from the magnetic cloud region, the probabilty for the particle to reach the energy E_n goes with $(1 - P_{esc})^n$. Therefore, the amount of particles which stay longer in this region and hence gain more energy is proportional to the number of particles which remain in the cloud for more than n hits

$$N(> E_n) = N_0 \sum_{m=n}^{\infty} (1 - P_{esc})^m \propto \frac{1}{P_{esc}} \left(\frac{E_n}{E_0}\right)^{-\gamma} \tag{2.5}$$

with

$$\gamma \approx \frac{P_{esc}}{\xi}. \tag{2.6}$$

We see that pure stochastic acceleration leads to the power law spectrum in energy.

The general argument of Fermi was that the probability for head-on collisions of particles in magnetized clouds is larger than for head-tail collisions and so the particles are accelerated in average. If we take a particle entering the cloud with energy E_i under an angle of θ_i relative to the cloud's direction and emerges at an angle θ_o with energy E_o after a lot of diffuse scattering on the magnetic irregularities, the gain in energy can be obtained by Lorentz transformation (lab. frame: unprimed, cloud frame: primed).

$$E_i' = \Gamma E_i(1 - \beta \cdot \cos(\theta_i)) \tag{2.7}$$

$$E_o = \Gamma E_o'(1 - \beta \cdot \cos(\theta_o)). \tag{2.8}$$

The fractional gain in energy can then described by

$$\xi = \frac{\Delta E}{E} = \frac{E_o - E_i}{E_o}. \tag{2.9}$$

Averaging over θ_i one can show that

$$\xi \propto \frac{4}{3}\beta^2 \tag{2.10}$$

where the square leads to the name of the mechanism: *Second order Fermi acceleration* [Gai90].

Unfortunately this accerelation is a very slow process. Therefore, Blandford and Ostriker proposed a more efficient mechanism realized in plane shock fronts [BO78]. We start with a huge shock wave with velocity $-u_1$ and relative to it a downstream shocked gas with velocity u_2, where $|u_2| < |u_1|$. To calculate the energy gain per crossing one proceeds similar to Fermi's idea and ends up with a rate $< \cos(\theta_i) >= -2/3$ for particles going from downstream to upstream and $< \cos(\theta'_o) >= 2/3$ vice versa. This yields an fractional energy change of

$$\xi \propto \frac{4}{3}\beta. \tag{2.11}$$

As this equation goes with the first order of β, thus it is the *First order Fermi acceleration*, it is more efficient than the original Fermi proposal [Gai90]. Note that for strong shocks the acceleration meachnism leads naturally to an E^{-2} spectrum [Sok04].

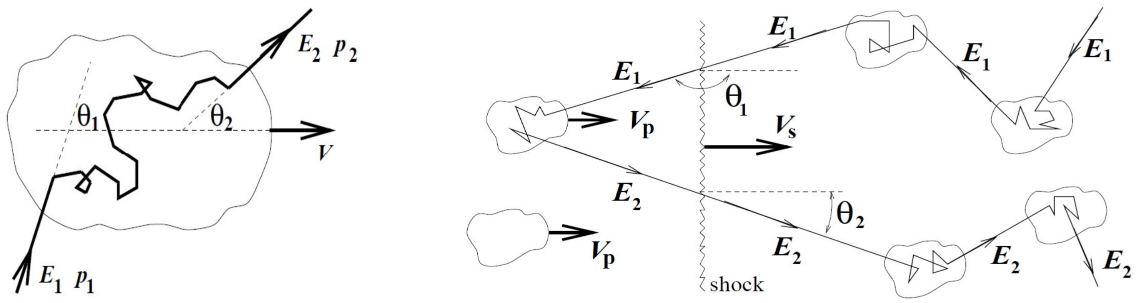

Figure 2.5: Left: Second order Fermi acceleration in moving magnetic cloud. Right: First order Fermi acceleration in strong plane shocks. Both sketches from [Pro99].

2.3 Propagation of cosmic rays

On their way from the sources to the Earth, cosmic rays are deflected by magnetic fields which intensity e.g. can be estimated by measuring the rotation of the polarization plane of the emitted radiation from extragalactic sources like pulsars. Regular intergalactic fields are settled at values lower than 10^{-9} G, galaxy clusters may have a strong coherent field on Mpc scale. The Milky Way's magnetic field is known to have a regular large scale structure with a field strengh of typically few μG. The field lines follow the spiral arm's of our Galaxy.

The gyro-radius for a 1 EeV proton in a field of 3 μG is approximately 300 pc, which corresponds to the the thickness of the Galactic disc. Fortunately the gyro-radius for a particle with rigidity E/Z above 10 EeV is of the same order as the traveled distance which means that the motion itself is not significantly affected by the magnetic field and the incoming direction is conserved.

To determine the angular deflection one needs to know the Larmor radius of the investigated particle $r_L \cong E/(Z \cdot B_\perp)$. If the magnetic field is constant over the traveled distance d, we have:

$$d\theta(E,d) \cong \frac{d}{r_L} \cong 0.52^\circ \cdot Z \cdot \left(\frac{E}{10^{20}\,eV}\right)^{-1} \cdot \left(\frac{B}{10^{-9}\,G}\right) \cdot \left(\frac{d}{Mpc}\right), \tag{2.12}$$

which results in a deviation of less than 1° of the original direction for a 10^{20} eV proton in a magnetic field of 1 μG on a distance of about 1 kpc. A more realistic scenario, which includes the coherence length and spread of the magnetic fields leads to:

$$d\theta(E,d) \cong 0.8^\circ \cdot Z \cdot \left(\frac{E}{10^{20}\,eV}\right)^{-1} \cdot \left(\frac{B}{10^{-9}\,G}\right) \cdot \left(\frac{d}{10\,Mpc}\right)^{1/2} \cdot \left(\frac{\lambda}{Mpc}\right)^{1/2}. \tag{2.13}$$

While their propagation through the universe the primaries can also interact with the radiation fields like the cosmic microwave background (CMB), the infrared background (IR) and the radio background (RB). The CMB, eventhough already predicted in the 1940s, was first measured by Penzias and Wilson in 1964 [PW65]. Using this information Greisen, Zatsepin and Kuzmin predicted, that the spectrum of the cosmic rays should show a step cut-off at $5 \cdot 10^{19}$ eV due to pion production on the CMB (therefore it is named GZK-Effect) [Gre66], [ZK66]. The following processes are the major ones at this energy range:

$$p + \gamma_{CMB} \rightarrow \Delta \rightarrow p + \pi^0 \tag{2.14}$$

$$p + \gamma_{CMB} \rightarrow \Delta \rightarrow n + \pi^+ \tag{2.15}$$

The threshold energy for pion production on the CMB photons in a head-on collision is given by

$$E_{th} = \frac{m_\pi}{4\epsilon}(2m_p + m_\pi) \cong 7 \cdot 10^{16} \left(\frac{\epsilon}{eV}\right)^{-1} eV, \tag{2.16}$$

which, assuming an average photon energy of $5 \cdot 10^{-4}$ eV, yields a cut-off energy of about 10^{20} eV. The mean free path for protons can be estimated to roughly 8 Mpc using a CMB photon density of n $\approx$ 400 cm^{-3}. The energy loss per interaction is about 1/5 and according to this the attenuation lenght is of the order of some tenths of Mpc, hence the proton energy drops below the GZK-threshold rather rapidly. So they concluded, that the sources of the highest energy cosmic rays must be within a sphere of that radius.

At lower energies the Bethe-Heitler pair production $p + \gamma_{CMB} \rightarrow p + e^+ + e^-$ becomes dominant with a threshold energy of $5 \cdot 10^{17}$ eV and a mean free path of about 1 Gpc. Nuclei with higher mass undergo photo-disintegration and pair-production on the CMB and the IR. Since the energy is shared between the nucleons, the threshold for this processes increases. For gamma rays the dominant interaction is pair production with a threshold of about $3 \cdot 10^{14}$ eV, whereas electrons and positrons mainly do inverse Compton scattering. Neutrinos as the last component of cosmic ray primaries are associated with the proton acceleration as they mostly originate from the decay of charged pions or subsequent muons. Therefore, their spectrum in some sense mirrors the proton spectrum with a cut-off at lower energies. As they are insignificantly affected by interactions with background radiation and not at all by magnetic fields their flux and arrival directions give important hints about the sources.

2.4 Extensive air showers

An Extensive Air Shower (EAS) is a cascade of particles generated by the interaction of an initial high energy primary particle penetrating the Earth's atmosphere. After the particle has transversed a particle- and energy-dependent mean atmospheric depth it hits a nucleus of the atmosphere producing secondary particles which themselves then move on and initiate further sub-cascades. The leading particle front propagates with almost the (vacuum) speed of light through the atmosphere, evolving to a maximum number of particles and then decreasing again. One important property of EAS is the concentration of shower particles in a thin disc, the so-called „pan-cake “, with a thickness of only a few meters. The lateral extent is mostly due to multiple scattering of the particles.

As the flux of cosmic rays drops rapidly with energy, direct detection of cosmic rays becomes unpractical and the measurement of EAS is the only way of (senseful) observation above 10^{15} eV. Quantities like longitudinal development, lateral distribution, arrival time distribution or energy deposit can be determined experimentally. There are several ways to measure these parameters which will be discussed in section 2.4.2 and in more detail in chapter 3 for the Pierre Auger Observatory. In the next subsection we will focus on the different components during the shower development.

2.4.1 Shower development

The first interaction of the primary with the atmosphere typically occurs at a height of 20-30 km. Assuming a primary cosmic ray nucleon, mostly kaons and muons together with a leading baryon are produced sharing the primary energy. The resulting shower is composed of three main components (see Fig. 2.6):

- The *electromagnetic part*, e^+, e^- and γ, which has 95% of the energy
- The *muonic part*, μ^+ and μ^-, which carries about 4% of the energy
- The *hadronic part*, mainly π^+, π^- and π^0, with approximately 1% of the energy

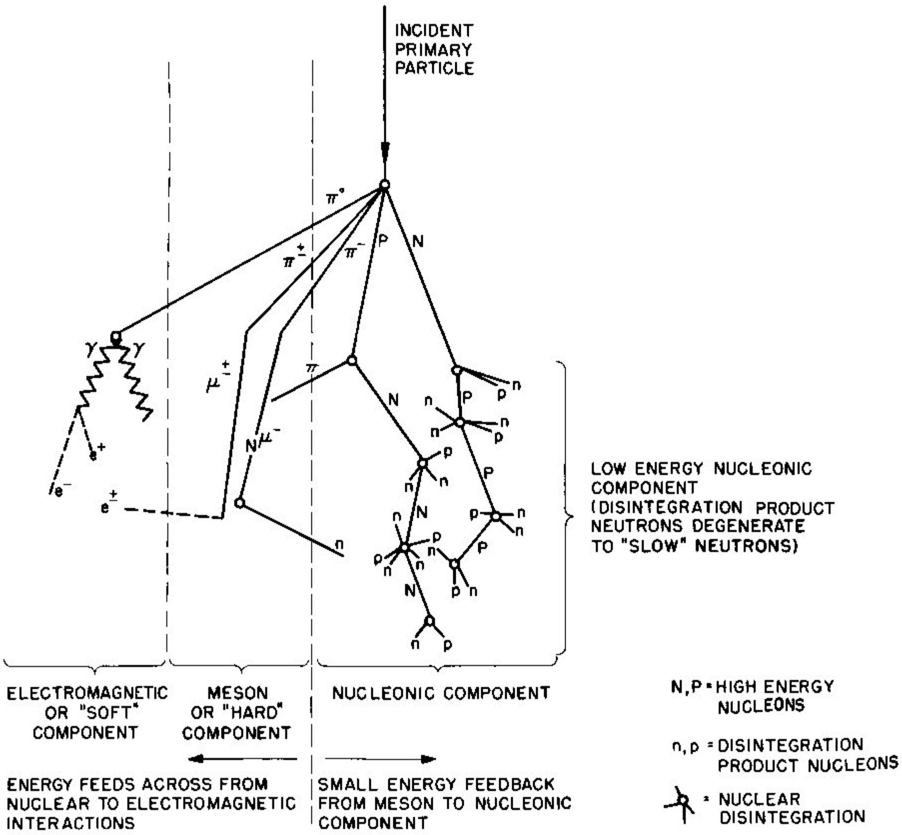

Figure 2.6: Shower development with the three major components [Uni10].

An important parameter of the longitunal shower development is the matter transversed by the shower particles, formally known as slant depth X. This quantity is measured in g/cm^2 starting from the top of the atmosphere along the direction of the incident nucleon, related to the density profile $\rho(h)$ of the atmosphere by

$$X = \frac{X_\nu}{\cos\theta} \tag{2.17}$$

with the vertical atmospheric depth X_ν given by

$$X_\nu = \int_h^\infty \rho(h')dh'. \tag{2.18}$$

A rather simplified way to understand the most important features of the cascade has been introduced by Heitler [Hei44]. The model itself is extremely simple, but it describes the development qualitatively correctly up to the shgwer maximum. In a cascade of particles of the same type two new particles are created after an interaction length λ, each carrying half of the primary particle energy $E = E_0/2$ as shown in Fig. 2.7. Each interaction process doubles the number of particles and halves the energy of each produced particle.

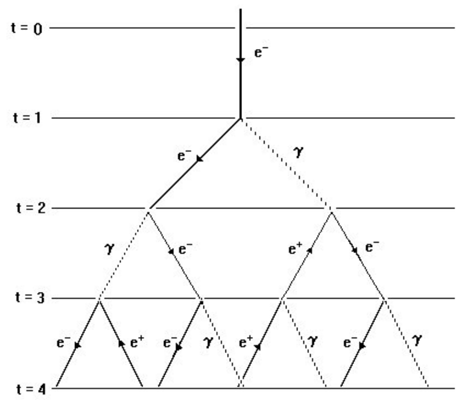

Figure 2.7: Heitler's toy model of cascade development (here for an incoming e^-) [Tea10].

This sequence continues until a critical energy E_c is reached where the splitting stops and the particles only lose energy, get absorbed or decay. Therefore, the maximum number of particles is given by

$$N_{max} = E_0/E_c \tag{2.19}$$

and the depth of the maximum as

$$X_{max} = \lambda \frac{\ln(E_0/E_c)}{\ln 2}. \tag{2.20}$$

Using the relation $X_{max} \propto \ln(E_0)$ one can also draw some conclusions rolling back to the chemical composition of the primaries. Assuming that for heavier nuclei of mass A the total energy E_0 is distributed equivalent to the A independent nucleons, equation 2.20 becomes

$$X_{max} \propto \ln\left(\frac{E_0}{A \cdot E_c}\right) \tag{2.21}$$

The dependence on A implies that on average showers generated by heavier primaries develop more rapidly than proton showers with the same energy. Another feature to distinguish between different primiaries are the fluctuations in the longitudinal development as heavy nucleons tend to have smaller fluctuations.

An EAS consists of three components which can be distinguished by means of particle physics detection. The hadronic component adds particles to the electromagnetic and muonic component. Nevertheless, all components have their typical evolution processes:

Hadronic component

Assuming a nucleon or nucleus as cosmic ray primary, the cascade starts with a hadronic interaction. The basic components in hadron showers are pions and kaons, which are produced either in collisions or via decay of resonances. The depth of the first interaction depends on the interaction length which varies between 70 g/cm^2 for protons and 15 g/cm^2 for iron. Addionally, this position also influences the point of the shower maximum X_{max} and precise measurement of this parameter can help identifying the primary of the shower.

A parametrization of the longitudinal development of hadronic showers was done by Gaisser and Hillas [GH77]:

$$N(X) = N_{max} \left(\frac{X - X_0}{X_{max} - \lambda} \right)^{\frac{X_{max}-\lambda}{\lambda}} \exp\left(-\frac{X - X_0}{\lambda} \right), \tag{2.22}$$

where X_0 is the point of the first interaction, X_{max} the shower maximum with its size N_{max} and the mean free path λ. This *Gaisser-Hillas* formula is used as standard fit for the longitudinal shower development.

Muonic component

The major part of the charged pions and kaons from the hadronics shower core decays into the muonic (hard) component:

$$\pi^{\pm} \rightarrow \mu^{\pm} + \nu_{\mu}(\bar{\nu}_{\mu}) \;\; (BR : 99.99\%) \tag{2.23}$$

$$K^{\pm} \rightarrow \mu^{\pm} + \nu_{\mu}(\bar{\nu}_{\mu}) \;\; (BR : 63.51\%) \tag{2.24}$$

Although the resulting muons are unstable with a typical lifetime of about 2.2 μs, almost all of them reach the ground due to time dilatation effects (for $E_{\mu} >$ GeV). As their way through the atmosphere is not much disturbed by multiple scattering and their path is mostly rectilinear, ground detection of muons is a good way to reconstruct the early shower development and gaining information about the nature of the primary particle.

Electromagnetic component

The decay of the neutral mesons on the other hand starts the electromagnetic (soft) component of an EAS:

$$\pi^0 \rightarrow \gamma + \gamma \;\; (BR : 98.8\%) \tag{2.25}$$

$$\pi^0 \rightarrow \gamma + e^+ + e^- \;\; (BR : 1.2\%) \tag{2.26}$$

Additionally these cascades can directly be started by high energy photons or electrons using an interplay of pair production and bremsstrahlung:

$$\gamma + N \rightarrow N + e^+ + e^- \tag{2.27}$$

$$e^{\pm} + N \rightarrow N + e^{\pm} + \gamma. \tag{2.28}$$

This chain continues until a critical threshold energy of $E_c = 85.1$ MeV in air is reached where the ionization energy loss starts to dominate the bremsstrahlung and the electron is attenuated within one radiation length.

2.4.2 Detection techniques

Several techniques for the detection of EAS have been approved to date using special shower features. The most common approach is the direct measurement of shower particles reaching the ground with an array of detectors which are distributed over a large area due to the low flux of cosmic rays. These arrays consist of particle detectors like Cherenkov radiators or plastic scintillators, which are placed in a regular spacing. Measuring the deposited energy of the shower as a function of time it is possible to estimate the energy and the direction of the primary cosmic ray. Necessary for this reconstruction is the fitting of the lateral distribution function of particles, which is mainly determined by Coulomb scattering of the dominant electromagnetic component. It can be approximated by the Nishimura-Kamata-Greisen (NKG) function

$$\rho(r) = k \left(\frac{r}{r_M}\right)^{-\alpha} \left(1 + \frac{r}{r_M}\right)^{-(\eta-\alpha)}, \tag{2.29}$$

where r_M is the Moliere radius (roughly 78 m at sea level), η, α are experiment-dependent parameters and k is proportional to the shower size.

Another well-suited method is the reconstruction of the longitudinal shower development by collection of fluorescence light which is produced by charged particle interacting with nitrogen in the atmosphere. As the seconday cascade evolves the ionized particles can excite the 2P and 1N bands of the N_2 and N_2^+ molecules. During the de-excitation process ultraviolett radiation ($\lambda \approx 300 - 400$ nm) is emitted istropically. Therefore, the detectors can see showers even at large distances, with the shower development appearing as a rapidly moving spot of light across the night-sky. Since the ratio of energy emitted as fluorescence light to the total energy deposited is less than 1% low energy showers (E$<10^{17}$ eV) are rather hard to detect. Unfortunately, the duty-cycle for these kind of measurements is only of the order of 10% as the necessary background discrimination limits them to clear moon-less nights.

As both kinds of measurement are combined in the hybrid-detector of the Pierre Auger Observatory the more technical parts of the detection techniques will be skipped to the concerning sections 3.1 and 3.2.

2.5 Radio emission in EAS

A more recent technique to detect air showers utilizes the effect that EAS also emit energy at radio frequencies. Already in 1965 Jelley et al. discovered that EAS, initiated by high-energy cosmic rays, produce strongly pulsed radio emission at frequencies around 40 MHz. [Jel65]. In the following years a number of experiments established the presence of radio emission over a frequency-range from a few to a few hundred MHz. In parallel also a lot of work was spent into the theoretical interpretation of the process. But due to the upcoming promising results from other techniques the radio detection fell more and more into oblivion. In the context of next-generation digital telescopes the great potential of this kind of measurement was re-discovered and several small-scale projects have proven the feasibility of EAS detection with radio [HAB05]. Sharing the main advantage of optical fluorescence detectors, namely a very direct view into the shower development, they are not hindered by the need of superb observing conditions at the same time. For a purely radio-triggered array with a low number of antennas radio detection shoud be possible for energies $\geq 10^{17}$ eV. In combination with external triggering or a huge array of ground detectors the study of EAS ranging from 10^{15} eV up to ultra-high energies would be possible.

The first postulated process for radio emission from air showers was Cherenkov radiation. The particles in the air shower travel faster than the speed of light in air and so they emit Cherenkov radiation. The physical thickness of the air shower disk is smaller than the wavelength at radio frequencies so the emission is coherent. In a neutral shower which contains as many electrons as positrons the emission of both would cancel each other out. Askaryan proposed that an air shower would develop a negative charge excess because the atmosphere or any other matter contains many electrons but no positrons. The net charge then allows an air shower to emit Cherenkov radiation at radio wavelengths.

Another emission mechanism is due to the deflection of charged particles in the earth's magnetic field. There are two ways to look at this, both are expected to be equivalent:

A prominent representation of a macroscopic approach is given by the transverse current description originally proposed by Kahn & Lerche [KL66], which has recently been implemented in a modern fashion, called the model of geo-magnetic radiation (MGMR) by Scholten and Werner [SW09]. These approaches describe the bulk motion of secondary electrons and positrons in the geomagnetic field leading to transverse currents and ensuing effects such as moving dipoles leading to radio emission from an air shower (see Fig. 2.8, left). Also the effect of radiation due to the charge excess in the shower has to be considered, but in general this is shown to give only a small correction. However, for certain geometries the finite index of refraction of air may give rise to a sharp Cherenkov-like pulse. Due to the more analytical description, this approach is particularly well suited to relate the time structure of the radio pulses to the air-shower evolution profile. The same is true for a simplified description for radio emission at large impact parameters which tries to incorporate also the geosynchrotron picture.

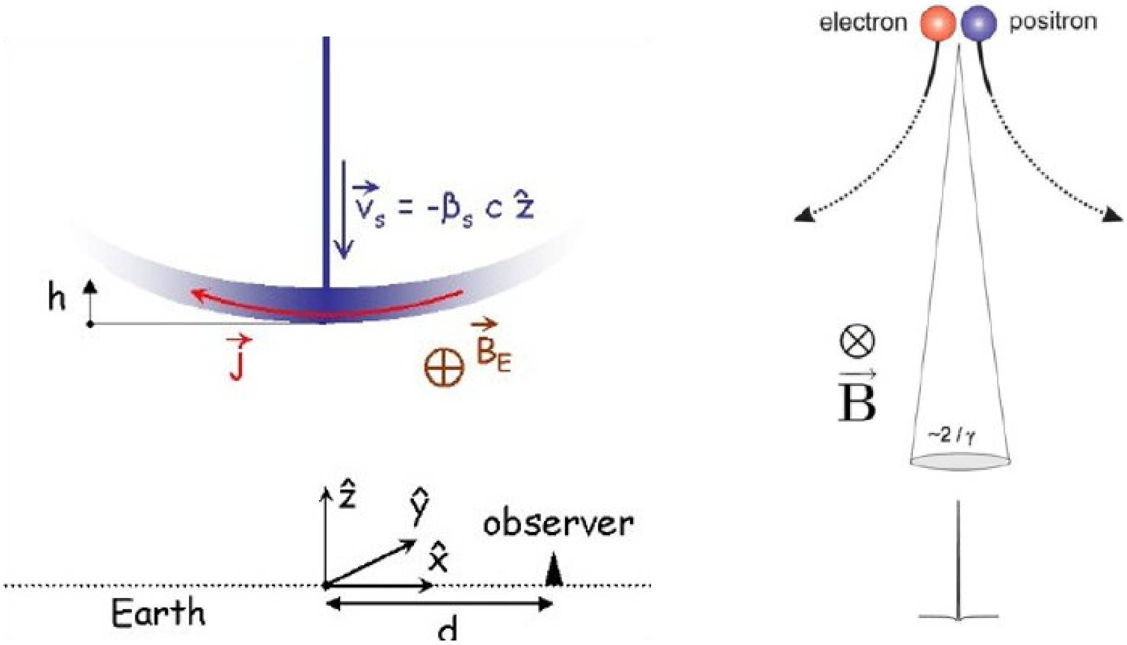

Figure 2.8: Model of MGRM emission (left) and geo-synchrotron emission (right) [SWR08].

In the group of the microscopic approaches, the geo-synchrotron model describes the radio emission as being due to the deflection of relativistic secondary electrons and positrons in the Earth's magnetic field. This approach was mostly driven by the work of Falcke and Gorham [GF03] and later by Falcke and Huege [FH05]. The large eletromagnetic component of the air shower that moves through the geomagnetic field is subjected to the Lorentz force

$$\vec{F} = q(\vec{v} \times \vec{B}) \tag{2.30}$$

with the charge q, the velocity v and the magnetic field B. The positive and negative charges are deflected, leading to synchrotron-like radio emission as sketched in Fig. 2.8, right side. For highly relativistic particles with a high Lorentz factor γ the original dipole emission is focused into a norrow emission cone with an opening angle of the order of $2/\gamma$. The emission is coherent at frequencies of 1 MHz to 150 MHz and leads to strong radio pulses of some 10 ns length. For a closer analytical description see [FH05].

A prominent implementation of the geo-synchrotron approach is given by REAS (for further information see [HUE07]), a publicly available Monte-Carlo code simulating the radio emission from air showers that themselves have been simulated with the full complexity of the shower-simulation CORSIKA. The properties of radio emission from air showers have been studied in detail with various implementations of the REAS code in the recent years. As a short impression the figures below show some results of the simulation of both models

[Hue10]. The electric field strength as a function of time for REAS (left) and MGRM (right) is depicted in Fig. 2.9. Both models predict bipolar pulses with matching field strength better than a factor 2 (note the different scalings for the different core distances). Also the spectra for different distances to the core in Fig. 2.10 look rather similar with small differences near the shower axis. This really good overall agreement for the two different approaches is a huge success and progress in radio emission theory.

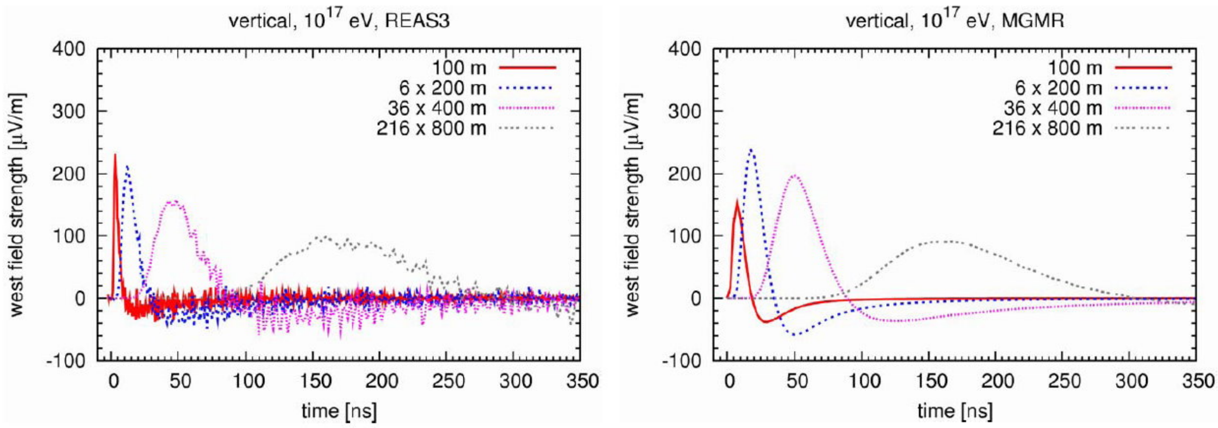

Figure 2.9: Electric field strength as a function of time for REAS (left) and MGRM (right) for different core distances [Hue10].

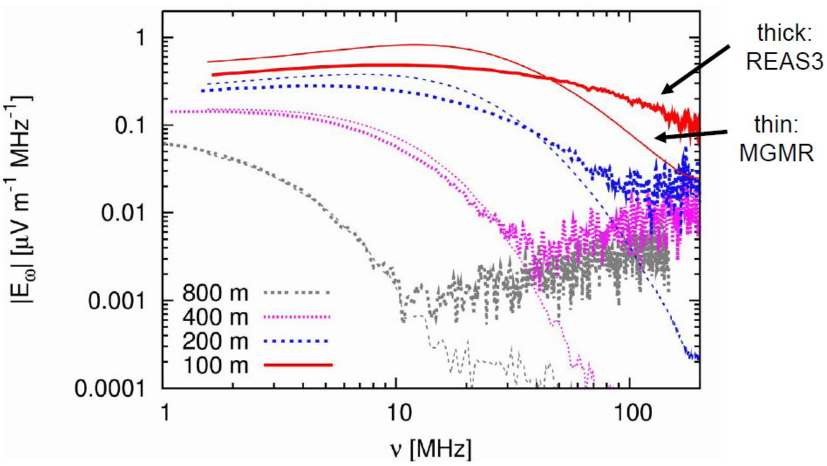

Figure 2.10: Spectra for REAS (thick) and MGRM (thin) for different core distances [Hue10].

Chapter 3

The Pierre Auger Observatory

The Pierre Auger Observatory (PAO) is situated in the Pampa Amarilla in Mendoza, Argentina near the city Malargue, about 1400 m above sea level. Spread over an area of about 3000 km^2 it is the worldwide largest detector array for the detection of cosmic rays at the highest energies. A very important asset to the existing setups is the hybrid design. The observatory combines (at the moment) two independent ways of detection. The array consists of 1600 water-Cherenkov tanks, the so called surface detectors (SD), measuring the lateral distribution of an EAS, which are overlooked by the four „eyes“ of the fluorescence detectors (FD), each containing six optical telescopes. Figure 3.1 gives an overview over the array. Building started in 2002 and since 2004 the observatory is taking scientific data, the last tank for now has been deployed in June 2008. At present the project has gathered more than 400 scientists from over 94 institutes coming from 18 different countries. For a full-sky coverage another, even larger observatory in the northern hemisphere is planned to be build in the near future.

3.1 The surface array

The full setup of the SD array contains 1600 autonomous, solar-powered detector stations placed on a triangular grid with 1500 m distance. Each station is build up of a 120 cm high, cylindric tank with a base area of 10 m^2. The tank height is designed to absorb almost completly the electromagnetic component. It is filled with 12 tons of pure water which is monitored by three 9 inch photomultiplier tubes (PMTs). The readout is performed by digital electronic modules, FADCs with 40 MHz sampling and 10 bits resolution, digitizing a dynamic range matched by a low and a high gain channel and storing the data in a ring buffer memory. The stations host a GPS receiver to synchronize triggered data as well as a radio communication system, which sends data to the central data acquisition system (CDAS). A schematic drawing of the SD tank is shown on the left of Fig. 3.2.

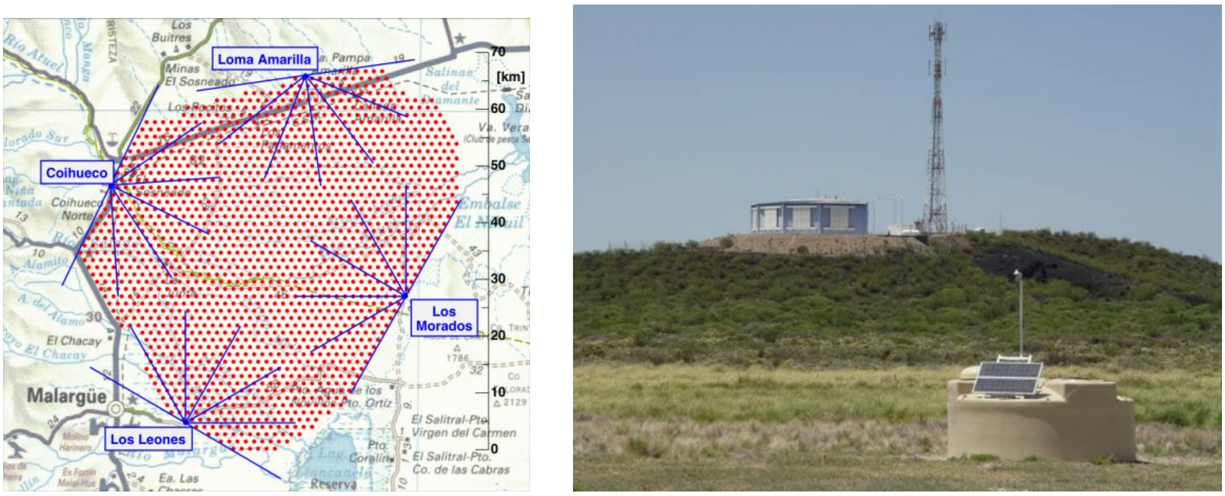

Figure 3.1: Right: Map view of the southern Pierre Auger Observatory with the 1600 tanks (red dots) and the field of view of the 24 telescopes (blue lines). Left: A surface detector in front of a telescope building in the pampa.

If a high-energy particle passes through the tank with a velocity v, which is larger than the speed of light c_n in the media (here: water) with refraction index n, it emits Cherenkov-radiation under an angle $\theta_c = \arccos \frac{1}{\beta n}$ with respect to the particle track. This light is then detected by the PMTs in the tank. A typical signal is of the order of a few microseconds, but duration and amplitude vary strongly as a function of distance from the shower core. Usually the number of particles in each tank is given in units of vertical equivalent muons (VEM) defined as the average charge signal produced by a penetrating down-going muon. Also the calibration is done by atmospheric muons, which are known to form a uniform background.

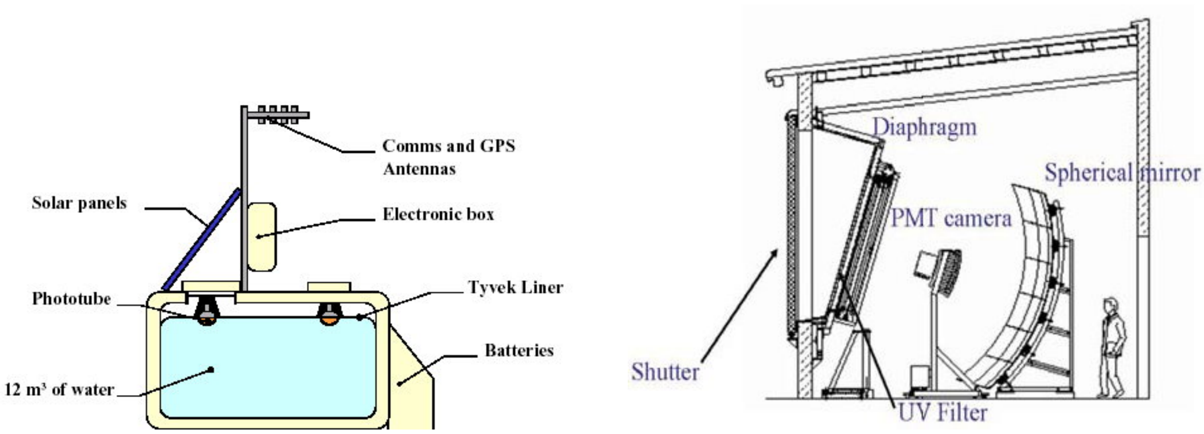

Figure 3.2: Sketch of a water tank [Anc04](left) and a fluorescence telescope [Pie01] (right).

3.2 The fluorescence telescopes

The FD is designed to detect fluorescence light, emitted by de-excitation processes of nitrogen molecules. The yield is very low, but large imaging telescopes are able to detect this during clear, almost moonless nights, resulting in a duty cycle of $\approx 10 - 15\%$. The setup is composed of 4 different eyes (named Los Leones, Los Morados, Loma Amarilla and Coihueco) as shown in Fig. 3.1 located at the perimeter of the SD, which enables detection of EAS simultaneously by both detectors („hybrid"). Each eye consists of six independent Schmidt telescopes, each made of a 440 pixel camera, one covering a field of view of $1.5° \times 1.5°$. They are arranged in a 22×20 matrix to give a total field of view of 30° in azimuth and 28.6° in elavation, adding to a 180° view inwards the array on one eye. The fluorescence light is collected by a 12 m^2 spherical mirror with a curvature of 3.4 m and reflected to the camera, located at the focal surface of the mirror. The telescopes use a Schmidt optics design with a diaphragm at the center of curvature of the mirror. To avoid interfering background light a UV transparent filter is used that restricts the incoming light to wavelengths between 300 nm and 420 nm, where the main fluorescence emission lines are found. To avoid signal losses at the PMT boundaries, the gaps are filled with small light reflectors. The PMT signals are continuously digitized at 10 MHz sampling rate with a dynamic range of 15 bits in total. The major components of the telescopes are sketched on the right of Fig. 3.2.

An absolute calibration, using a large homogenous light source in front of the diaphragm, is done three to four times a year and provides the conversion between the digitized signal and the incident photon flux. Additionally relative calibrations are done to monitor short and long term changes with respect to the absolute calibration and the overall stability of the FD. An extensive atmospheric monitoring is necessary as the measured light has to be corrected due to aerosol (Mie) and molecular (Rayleigh) scattering in the atmosphere. Several methods are utilized to fulfil this purpose using laser systems located at each eye (LIDAR), a central laser facility (CLF) in the center of the array and probe balloons started at the balloon lauching station (BLS) in the south-west part of the array.

3.3 Extensions for the Pierre Auger Observatory

Two additional extensions will drive the development of the PAO towards a super-hybrid detector as shown in Fig. 3.3:

The first one is the *Auger Muons and Infill for the Ground Array* (AMIGA). Close to the telescope building Coihueco the grid spacing of the regular array will be reduced to 433 m respectively 750 m by the deployment of 85 additional tanks. By increasing the detector density the acceptance for showers in the energy range of 10^{17} to 10^{18} eV grows significantly. Plastic scintillators with an area of 40 m^2 each will be buried underground in immediate vicinity to these tanks with a shielding of 3 m of soil. This independent measurement of the moun number shall give further indications for the mass of the primary particle.

The second extension is called *High Elevation Auger Telescopes* (HEAT) and consists of three additional telescopes which are also build near Coihueco and therefore overlook the infill array as shown in Fig. 3.3. The main feature of the new telescope is the possibility to tilt the detectors to a field of view from 30° to 58.6° in elevation. This allows them to detect showers at higher atmospheric depths closer to the detector and extends the energy range of the FD by one decade to lower energies.

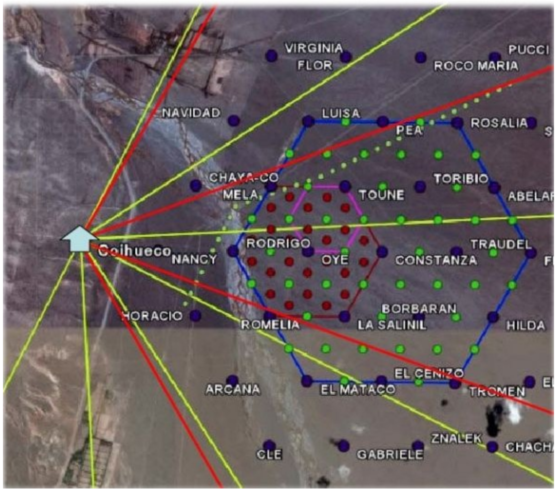

Figure 3.3: The infill area with the regular grid (blue points) and the AMIGA tanks (green and red points) overlooked by Coihueco (yellow lines) and HEAT (red lines) [EFW09].

3.4 The Auger Engineering Radio Array

3.4.1 Motivation

There are a number of worldwide efforts to develop and establish new detection techniques that promise a cost-effective extension of currently available apertures to even larger dimensions. These are, for example, large arrays of radio detectors. As demonstrated by Jelley [Jel65], the radiation emitted by the secondary particles can be measured with really simple antennas. An improvement in technology has led to a recent revival of the technology and projects like LOPES [Hau09] and CODALEMA [Lau09] have produced promising results at energies beyond 10^{17} eV. Therefore also the Auger Collaboration has started an R&D project to study UHECRs using the detection of coherent radio emission from air showers in the atmosphere. The Auger Engineering Radio Array (AERA) [AER09] will have a dimension of about 20 km^2, which will lead to an event rate of about 5000 identified radio events per year. The data gathered with these events will adress scientific as well as technological questions. On the technological site such an array will test concepts of hardware deployment and also the operation and monitoring of hardware and software issues. AERA shall fulfill three science goals which will be executed sequentially in time of operation and analysis:

- Thorough investigation of the radio emission which includes understanding of the dependence of the radio signal on shower parameters and geometry. This will also lead to an improved insight into the underlying emission mechanism.
- Exploration of the capability of the radio technique. Determination of the extend and accuracy of stand-alone radio-detection to provide information on the most important physics quantities of UHECRs.
- Composition measurements in the transition region of CRs with a unrivaled precision to study the energy spectrum.

Up to now two test setups have gathered data, one near the BLS and one at the CLF. Several antenna types and electronics were tested, increasing the experience needed for the build-up of such a large scale array. As the data from the BLS setup will be used in chapter 4.1 some more details will follow at that point.

3.4.2 Site information

AERA will be co-located with AMIGA, which is overlooked by HEAT, in the north-western part of the Observatory near the Coihueco fluorescence building. This connection to a super-hybrid detector will provide the worldwide unique possibility to study the details of radio emission from air showers in a timely manner [AER09]. The complete array will include 161 stations distributed over an area of about 20 km^2. The first 24 stations, named the core, are already deployed in a triangular grid of 150 m spacing including one triplet-station with a 30 m baseline. The core is about 4 km east of Coihueco and provides an excellent overlap for events which will be observed with both detection systems. Around this core, there will be 52 stations on a triangular grid with a baseline of 250 m. Finally, the outer region of AERA will have 85 stations with a distance of 375 m. The extension of the fully equipped array is about 6 km in east-west and 3 km in north-south. Left side of Fig. 3.4 gives an overview of the AERA layout.

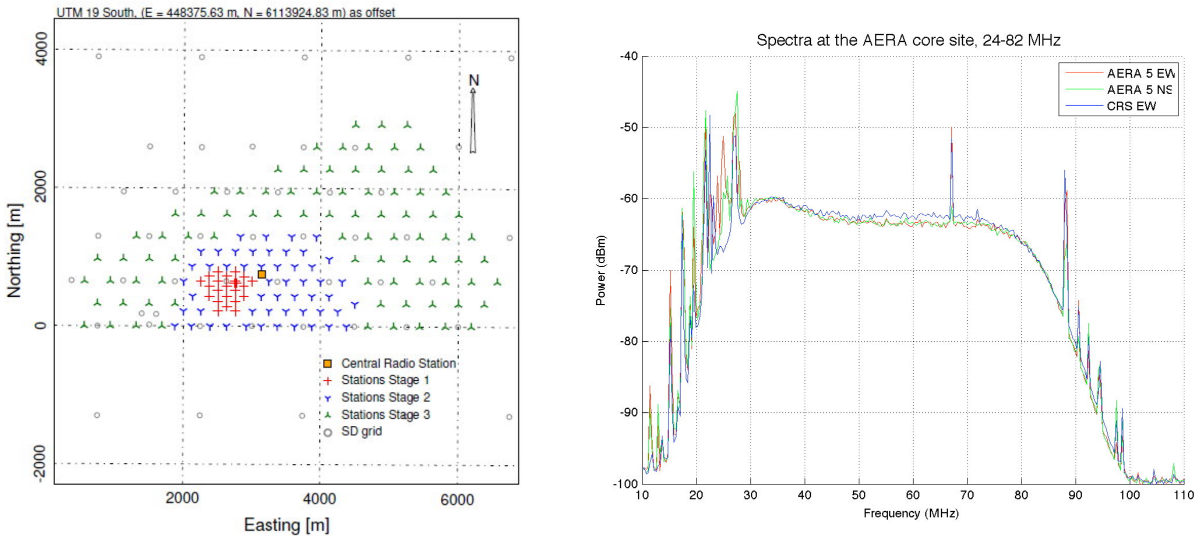

Figure 3.4: Overview of the AERA layout (left) and noise spectrum at AERA station 5 and the CRS (right) [Dal10].

Due to the rural landscape at the Auger site, this area is a rather perfect place for radio detection. In contrast to the setup of the LOPES experiment, which is located at the Karlsruhe Institute of Technology, Campus North, in between an industrial environment, several noise studies have shown that the condititions in Argentina are almost optimal in the used frequency range. A noise spectrum from the AERA site is shown in Fig. 3.4 (right) [Dal10]. The spectrum is almost flat in the measurement region of AERA except for a line at 67 MHz which appeared in December 2009. It is likely that this line comes from a TV transmitter, showing a central frequency line surrounded by sidebands. But knowing the existence of such bands one can easily filter them out in the digital electronics. The sensitivity of AERA to cosmic-rays radio pulses has been simulated for different energies. For pulses from showers with energies of $10^{19.5}$ eV the effective area is more than 75% of the total array. For smaller energies of about $10^{17.5}$ eV the core is still almost 100% efficient, but the remaining effective area shrinks to roughly 10% of the array.

3.4.3 Setup characteristics

The first 24 stations have already been deployed in the second half of 2010, one of them can be seen in Fig. 3.5. The log-periodic dipole antenna (LPDA) named „Small Black Spider“ and solar panels are visible while the electronics and digitizer are placed in the metal box (for details see [AER09]). The AERA stations are divided into subsystems which are briefly introduced. The LPDAs and analogue electronics (including a low noise amplifier (LNA) [Ste10]) are especially designed to detect radio pulses from 30-80 MHz.

The antennas are aligned with the magnetic north at the AERA site [Erd10]. Each antenna is sensitive to north-south and east-west polarization and has a low- and a high-gain channel for both polarizations. The filtered signal is digitized with 12-bit ADCs at a sampling rate of 180 MHz with an event size of 2048 samples per channel and is stored in the local-station electronics 2 GByte RAM memory. Assuming a raw data rate of 540 Mb/s this leads to a storage capacity of about 3 seconds. A Field-Programmable Gate Array (FPGA) which runs with a μLinux is used for managing the data storage and triggering, which filters the incoming data stream for interesting events. Selected data are then collected by a data acquisition system at the central radio station (CRS).

Figure 3.5: A radio-detector station installed at the AERA site. Visible is the „Small Black Spider“ LPDA, the GPS antenna and the solar panels above the electronics box.

The GPS antenna is used for time synchronization between stations. For communication between the stations and the CRS, fiber optics are used for the initial phase. A high-speed, low-power wireless communication system is under development for subsequent phases. Using this system, a data rate of 100-200 kbps between stations will be possible. A reference beacon will be used, which brings the timing accuracy between stations below 1 ns [Sch10]. The local stations broadcast only the time stamps of their individual trigger decisions to the CRS. The DAQ combines these information from different stations and their locations in the detector array. It searches for signal patterns that match radio signals which have been recorded by multiple detector stations. Only if this second-level trigger is fulfilled the CRS demands the transfer of the full waveform data which is still in the 2 GByte ring buffer. As local weather conditions might affect the reception and generation of radio signals, a weather monitoring system is installed at the CRS. The monitoring of the static electric field of the atmosphere is of special interest which serves to identify thunderstorms that occur close to the AERA site.

Chapter 4

The Offline framework

Within the Pierre Auger collaboration, a general purpose software framework has been designed in order to provide an infrastructure to support a variety of distinct computation tasks needed to analyze data gathered by the observatory [Pie07b]. The requirements of this project place strong demands on the software framework underlying data analysis. Therefore, it is implemented in C++ taking advantage of object-oriented design and common open source tools.

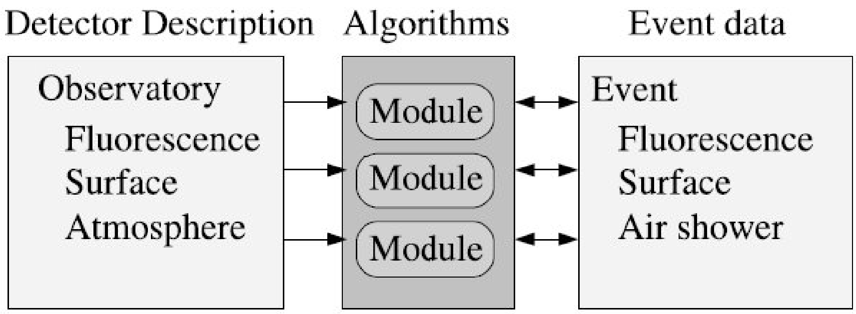

Figure 4.1: General structure of the OffLine framework.

In general the framework consists of three major parts as shown in Fig. 4.1:

- **Detector description**: The detector description is a read-only information. It provides a unified interface from which module authors can retrieve static (XML-based) or relatively slowly varying information (MySQL-based) about detector configuration and performance at a particular time. The requested data is passed to a registry of managers, each capable of extracting a specific part of information from a special data source.

- **Event structure**: The event data structure acts as the principal backbone for communication between modules. It contains all raw, calibrated reconstructed and Monte

Carlo data, which change for every event. Therefore, the event structure is build up dynamically, and is instrumented with a protocol allowing modules to interrogate the event at any point to discover its current constituents.

- **Processing modules**: Most tasks of interest can be reasonably factorized into sequences of self containend processing steps. In the framework this is done with *modules* which can be inserted via a registration card. The advantage is to exchange code, compare algorithms and build up a wide variety of applications combining modules in various sequences. In order to steer different modules a XML-based run controller was constructed for specifying instructions. This user friendly environment allows to choose which modules to use and to implement completly new modules without compiling the executable. XML files are also used to store parameters and configuration instructions used by modules or the framework itself. A central directory points modules to their configuration files which are created from a bootstrap file which has to be passed on the commmand line at run time.

In parallel a new ROOT based file format for summarizing the output of event reconstruction was developed which contains all the necessary event variables [Ulr06]. In reminiscence of the „Data Summary Tapes“ once popular in high energy physics experiments, it is called ADST standing for „Advanced Data Summary Tree“. The ADSTs were designed to contain all high level variables needed for physics analysis and (if desired) a fair amount of low level data to facilitate the development of new data selection cuts and to debug the reconstruction. Choosing ROOT over a simple ASCII format allows to handle more complicated data structures. Additonally a graphical showcase, the EventBrowser, for viewing the information stored in these ADST files was implemented.

4.1 SD reconstruction

The order of the modules executed by the SD reconstruction chain is defined in the ModuleSequence.xml control file. Typical content of the file for events recorded by the SD is:

```
<sequenceFile>
  <moduleControl>
    <loop numTimes="unbounded">
      <module> EventFileReaderOG </module>
      <module> SdCalibratorOG    </module>
      <module> SdEventSelectorOG </module>
      <module> SdPlaneFitOG      </module>
```

```
      <module> LDFFinderOG        </module>
      <module> SdRecPlotterOG     </module>
    </loop>
  </moduleControl>
</sequenceFile>
```

First necessary task is of course to read the input files which shall be used for the reconstruction. This is done by the *EventFileReader*. It is aware of several file formats as the standard format for Auger In- & Output *IoAuger* or input from shower simulations like CORSIKA or AIRES. The *SdCalibrator* has been developed by reverse engineering the CDAS equivalent *Ec*. Next to the calibration of the real events this module is offering an equivalent calibration procedure for simulated events.

The Offline implementation of the *SdEventSelector* is based on the official event selection description [Pie05]. A multitude of steps is done in that module which will shortly be described in the following. First one is the station selection where stations are passed or sortet out from the event for some criteria like lightning removal or if they are part of the engineering array. Also treatment of doublets and the infill is done during processing of this module. A new feature for selection of special parts of the array via the station IDs was implemented in this work and will be described in chapter 5.1. After that the trigger building starts with all the level 4 triggers (level 1-3 are done by the stations and the DAQ), like checking the signal in the first crown, meaning the hexagon around the tank with the highest signal. In order to perform a rejection of stations based on timing compatibility, a rudimentary geometrical reconstruction of the shower arrival direction is needed. This is the so called bottom-up selection. From the set of stations which passed the trigger cuts the triangle with the largest sum of station signals is selected and used as a seed. Using this seed and requiring compatibility with a planar shower front propagating with speed of light one can get a provisional shower axis. This again can be used for checking the timing compatibility of the other stations. Stations, which do not pass a specified condition for the arrival time, are flagged as accidential and not used for further reconstruction issues. For a detailed overview on the seed geometry calculations see [VR05]. Several other trigger levels are checked subsequent, cutting on this events can be switched on or off in the module.

The final reconstruction is done in the *SdPlaneFit*. The signal-weighted barycenter $\vec{b}$ of the stations involved in the fit is set as the origin from where all the distances are measured. Similarly, the weighted bary-time is set as the time origin. A shower track can be visualized as a point $\vec{x}(t)$ moving with the speed of light c along the straight line with axis $\vec{a}$ and passing the origin at t_0,

$$\vec{x}(t) - \vec{b} = -c(t - t_0)\vec{a}. \tag{4.1}$$

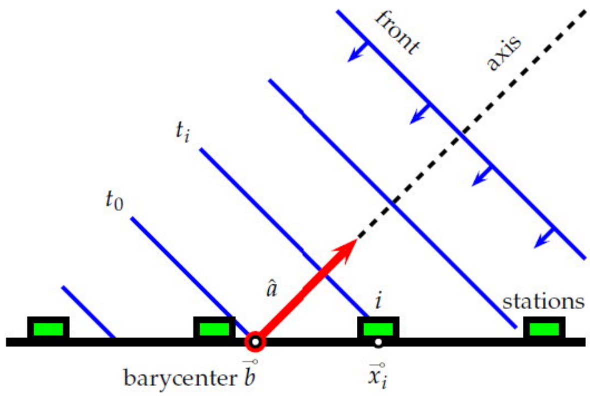

Figure 4.2: Schematic of the plane front arrival [VR05].

The shower plane is a plane perpendicular to the shower axis, moving along with the same speed. To infer on the time $t(\vec{x})$ when the shower plane is passing through some chosen point $\vec{x}$ on the ground, the point has to be projected to the shower axis.

$$ct/(\vec{x}) = ct_0 - (\vec{x} - \vec{b})\vec{a}. \tag{4.2}$$

Assuming that the deviations come only from timing uncertainties one ends up with a χ^2 function containing the measured time differences and the model predictions. This function has to be minimized. For further details on the approximate linear solution, see [VR05].

We are left over with the *LDFFinder*. The lateral dependence of the signal measured in a tank is modeled as

$$S(r) = S_{1000} \cdot f_{LDF}(r), \tag{4.3}$$

where f_{LDF} is a particular shape parametrization and S_{1000} the signal at 1 km distance from the shower core. There are currently two types of LDF that are supported by the module. A modified power-low and a slightly modified NKG function. For the concrete formulas and initial parameters see [VR05]. Again a minimization problem and a maximum-likelihood fit lead to a rather good estimate for the shower plane. The last thing done by the module is an analytic approximation of the curvature of the shower front.

The *SdRecPlotter* module mentioned in the above sequence is just for graphical issues and therefore not discussed here.

4.2 Radio reconstruction

Intuitively the reconstruction for radio events works rather similar to the one for SD, but additionally includes some more technical stuff, like hardware corrections. A rather standardised reconstruction sequence can be seen below:

```
<sequenceFile>
  <moduleControl>
    <loop numTimes="unbounded">
      <module> EventFileReaderOG              </module>
      <module> RdChannelADCToVoltageConverter </module>

      ... lots of RdChannelModules ...

        <loop numTimes="10">
          <module> RdAntennaChannelToStationConverter </module>
          <module> RdStationHilbertEnveloper          </module>
          <module> RdStationSignalReconstructor       </module>
          <moudle> RdDirectionConvergenceChecker      </module>
          <module> RdPlaneFit                         </module>
        </loop>

      <module> RdLDFFitter                    </module>
      <module> RecDataWriter                  </module>
    </loop>
  </moduleControl>
</sequenceFile>
```

First, the *EventFileReader* reads in the data in the appropriate format. Afterwards, concerning real data, one has to convert the measured ADC counts to voltages which are needed for the calculation of the electric field vector. It follows a lot of stuff handling the impact of the hardware and/or noise to the data like the removal of the pedestal, surpression of narrow-band radio interferences applying some filters or data upsamling for a better reconstruction.

The crucial point starts with the actual direction reconstruction in the inner loop. A usual plane fit is based on the signal arrival times which then yield the incident direction. The problem here is that the measured arrival times are heavily influenced by the response function of the antenna. Therefore, the plane fit needs the response corrected timeseries, but to correct the timeseries for the antenna response the incident direction is needed.

The solution for this kind of vicious circle is an iterative reconstruction of direction and correction for the response at once. At the first launch of the loop an initial test direction (zenith: 5°, azimuth: 45°) is used to correct for the response in the *RdAntennaChannel-ToStationConverter*. After the signal has been reconstructed a plane fit is done on the corrected timeseries which then is used as new estimate for the incoming direction. To avoid unnecessary waste of CPU time the *RdDirectionConvergenceChecker* is joined up in the loop which keeps a record of the last reconstructed directions. After each iteration a check is performed if the direction has changed significantly. If a pre-defined convergence level (standard: 0.5°) is reached, the module breaks the loop and continues with the outer sequence, if not, it continues the iterations. If no convergence is reached after 10 iterations, the event is skipped.

Fitting the lateral distribution of the radio signal, e.g. with an exponential function (done in the *RdLDFFitter*), the primary energy can be estimated. This is possible because the energy of the primary particle is correlated with the electric field strength at the core. In addition, according to simulations, the slope of the lateral distribution function carries information about the depth of the shower maximum and thus the mass of the primary particle. If this is experimentally confirmed, e.g. by comparing radio to FD or SD mass sensitive parameters, all primary quantities can be reconstructed by measuring the amplitude and arrival time of the radio pulse at each antenna position.

For more information about the radio functionality in Offline and the contained modules, the reader is refered to [Pie10d]. Figure 4.3 shows a tyipcal radio event as displayed in the Event Browser, where some general event informations like ID, angles, timestamp, the core position in the array and the ADC traces are displayed.

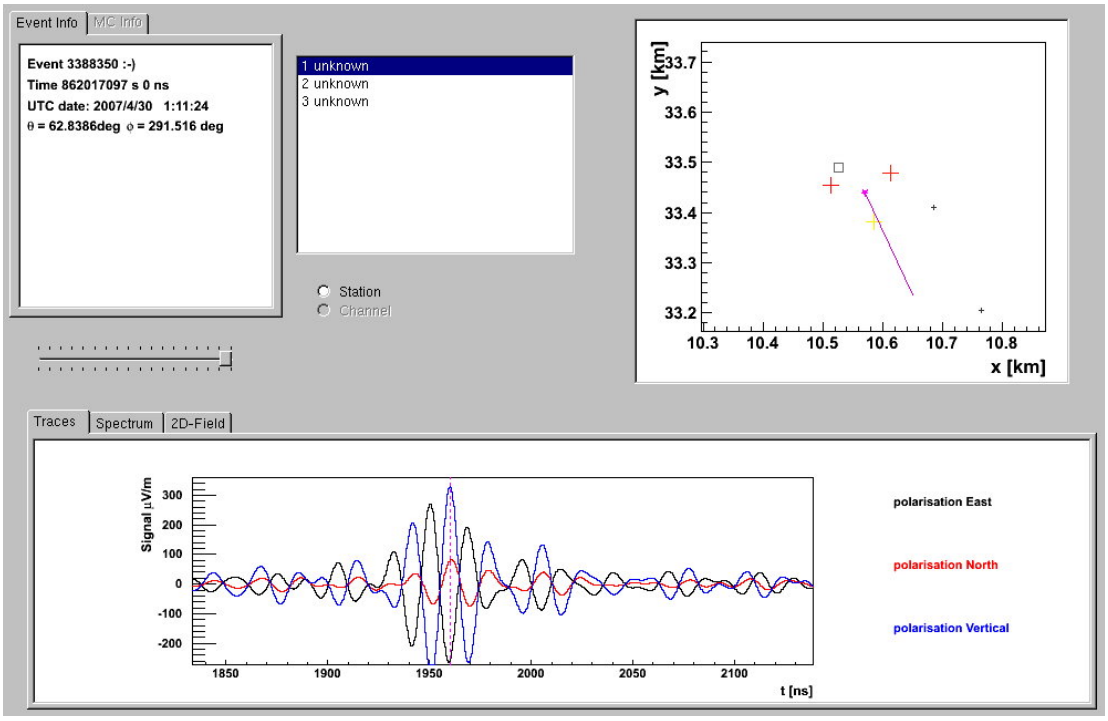

Figure 4.3: Radio event # 3388350 in the Offline EventBrowser. The different frames show inter alia some general event informations like ID, angles or timestamp (top left), the core position in the array (top right) and the ADC traces (bottom).

Chapter 5

An improved SD Reconstruction

The first part of this work deals with the improvement of the existing SD reconstruction as introduced in chapter 4.1. As already mentioned in chapter 3.4 two test setups were constructed at different positions in the PAO array for R&D purposes before building AERA. The setup which will be focused in this thesis is the one at the BLS. To increase the reconstruction accuracy and to lower the energy threshold in this specific area an additional SD tank, named 'Olaia', was deployed in the middle of the triangle which also contains the radio setup. Figure 5.1 gives an overview of the situation near the BLS with the antennas at P1 - P3.

Figure 5.1: Google Earth images of the BLS setup. Yellow dots indicate the SD tanks including the additional deployed 'Olaia', P1-P3 are the positions of the radio antennas.

The setup was dedicated for testing hardware. Several changes of systems occured during the measurement period. The first setup was build up of two standard LPDAs (P1 and P2) and one prototype wired-LPDA (P3). For more detailed informations on the antennas see [vdB07] and [Krö09]. Additionally, two scintillator panels were installed inside the fence of the BLS. The center-to-center distance between these plates was 6.5 m; each plate had an effective area of about 0.5 m^2. The readout of the antennas was triggered by a time-coincident signal from these scintillator detectors. This setup took data in this (outer) configuration for about one year from April 2007 to May 2008, which is also the time period for this part of analysis.

5.1 Changes in the Observer reconstruction

As already announced by the title of this chapter the main goal of this analysis was to improve the existing SD reconstruction, named SD-Olaia from now on. Therefore, some changes in the existing code had to be done. The first „problem "in the standard reconstruction is, that tanks which are not placed in the normal triangular grid spacing are flagged as *OffGrid* and therefore not used for further reconstruction issues (see Fig. 5.2). Fortunately, some effort in implementing the treatment of the infill stations was already put into the code by Jan Weseler (Karlsruher Institute of Technology), like the input of the different grid spacings which results in varying parameters for the crown distances and the seed time delay. A parameter comparison is depicted in table 5.1. The selection works via the variable *ArrayMode* in the SdEventSelector xml-card.

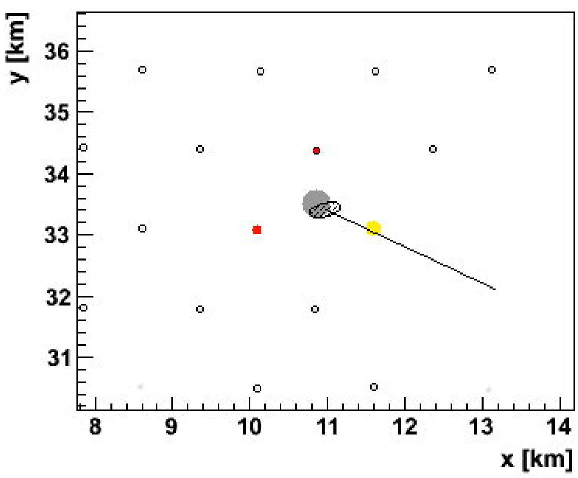

Figure 5.2: Event Browser view of a SD Event containing 'Olaia' (grey dot) which is flagged as OffGrid.

Additional code was implemented which allows the user to insert a list of stations (via their ID) in the xml-card. This list is used to reduce the number of reconstructions by cutting events which do not contain at least one of these stations before doing the plane fit, etc. The concerning c-code can be found in the Appendix. So for the further analysis the SD-Olaia reconstruction was restricted to events which contain 'Olaia' (ID = 1325).

Parameter	**Offline SD**	**Offline SD-Olaia**
C1MinDistance	1200 m	500 m
C1MaxDistance	2000 m	1000 m
SkewMaxDistance	2800 m	1600 m
SeedTimeDelayEarly	-1000 ns	-800 ns
SeedTimeDelayLate	2000 ns	1500 ns

Table 5.1: Comparison of reconstruction input-parameters for Offline SD and SD-Olaia.

The upcoming sections deal with the comparison of the analysis done with different reconstructions and also different data sets. As mentioned, the externally triggered setup took data for about one year in 2007/2008. In this period also a coincidence search with the SD setups was done. Therefore, we call the data set for the full period „cointime ", the data set which contains all the coincident events measured in that period is accordingly called „coindata ".

5.2 Comparison SD/SD-Olaia

The starting-point is the comparison of the standard Offline SD reconstruction with the improved SD-Olaia. This yields first information of the perfomance of the new version (or if working at all) and the improvement obtained. The main parameter for the gain in statistics is certainly the number of successfully reconstructed events. The full data period Offline SD-Olaia yields 3003 events, whereas SD reconstructs 837 events (out of these which were successful with SD-Olaia), which is only about 28%. So just by adding 'Olaia', we gain almost a factor 4 in statistics, which of course is a huge improvement for analysis. Explanation is rather easy as the usage of an additional tank in the trigger building, a lot events, which would not pass the criteria before due to two candidate stations only, now contain the needed triangle for seed construction with the addition of 'Olaia'.

The information about the core positions gives a nice overview over the reconstructed events and should show any artificial systematics in the determination process. Figure 5.3 shows the core positions for SD-Olaia (left, named SD*) and SD (right). The expected „Mercedes"-patter due to the higher detection efficiency right in the middle between two detectors is clearly visible for both reconstructions. The distribution for SD-Olaia is quite more expressive as we gain an additional increase in efficiency between the corner tanks and 'Olaia', which falls partly into the area where the efficiency is already increased due to the corner tanks, and of course due to the higher number of entries.

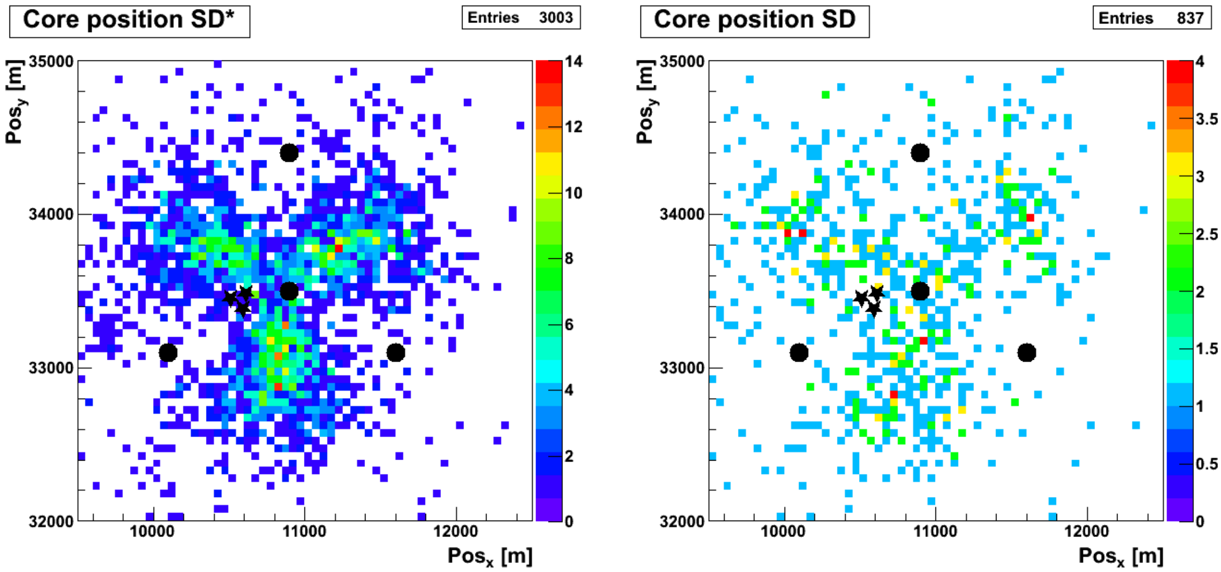

Figure 5.3: Core position for SD-Olaia (left) and SD (right).

The next interesting quantity is the angular residual of the two reconstructions which can be calculated as

$$\Omega = \arccos(\hat{r}_1 \cdot \hat{r}_2) \tag{5.1}$$

with

$$\hat{r}_i = (\sin\theta_i \cdot \cos\phi_i,\ \sin\theta_i \cdot \sin\phi_i,\ \cos\theta_i), \quad \text{for } i = 1, 2, \tag{5.2}$$

where 1 and 2 are the considered reconstructions. The resulting graphs can be seen in Fig. 5.1. About 98% of all events have angular residuals $\Omega < 5°$, the outliers are very inclined ($\theta > 60°$) and/or have large uncertainties on the reconstructed angles. The fit in the zoomed plot on the right is a Rayleigh function of the form

$$f(x, \alpha, \beta) = \alpha \frac{x}{\beta^2} \cdot exp^{-x^2/2\beta^2}, \tag{5.3}$$

where α is a normalization parameter and β is connected to the mean and the variance of the distribution. Here the function is just a guide to the eye as the overall residual is determined with the 68% quantile as $\Omega \approx 0.94°$, which means an excellent agreement of the reconstructions.

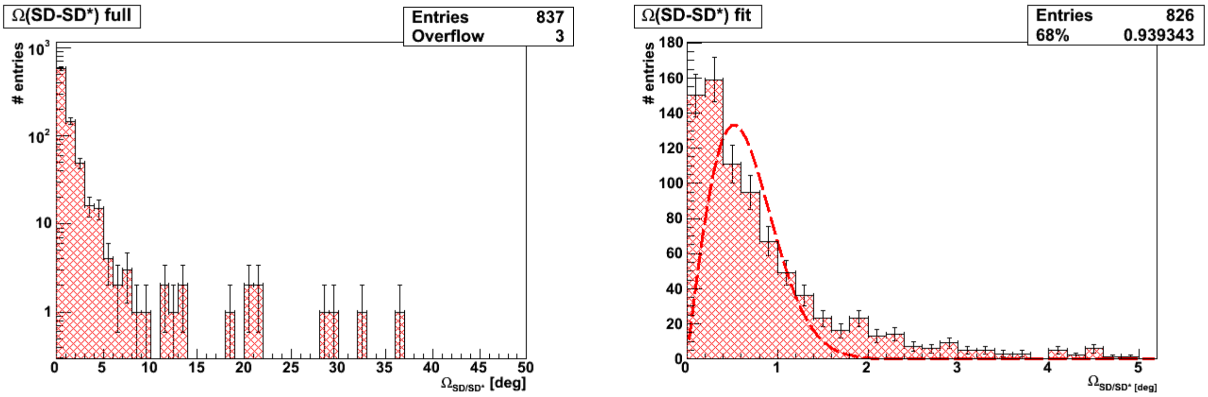

Figure 5.4: Angular residuals between SD-Olaia and SD for a large Ω range (left) and a zoomed plot with Rayleigh-fit (right).

Two additional variables of physics analysis are of special interest for efficiency studies. The first one is the radial distance of the shower core to 'Olaia', which, as it is the mean of the core position distribution, can be seen as the center of the considered area. Figure 5.5, left side, shows the number of events as a function of their radial distance, whereas the right side is the ratio of both histograms, giving the efficiency of the SD reconstruction in comparison to SD-Olaia. For events below 800 m distance, which is almost the baseline of the inner detector triangles, the efficiency is about 20 - 35 %. For events above this distance, the core falls outside the triangle and therefore the chance to be seen by other detectors around is definitely increased. This is the reason for the strong catch up in efficiency for the SD. Additionally events which have a larger distance to 'Olaia' and are still seen by the detector, must, in general, have a high energy and therefore a wider lateral distribution. This also leads to an increased detection probability for outer tanks, which will then contribute to the number of SD reconstructable events.

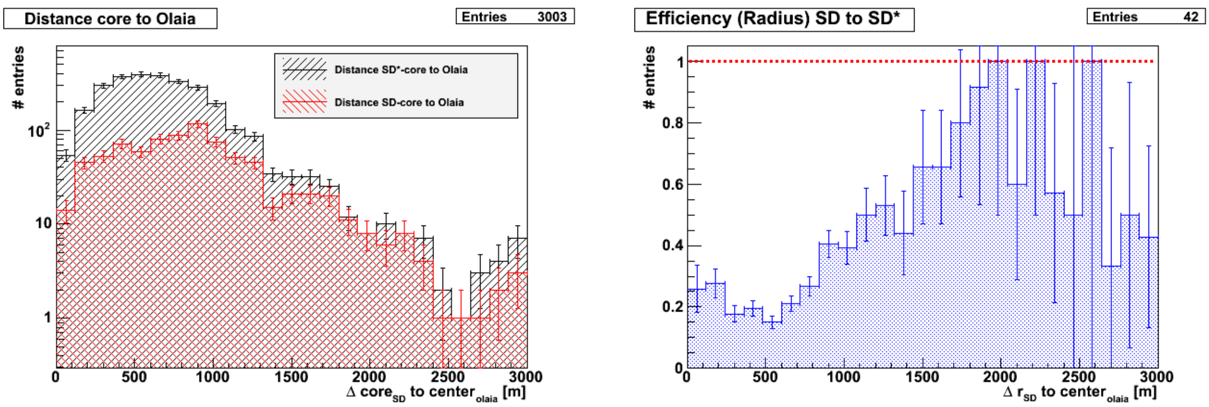

Figure 5.5: Radial distance of the shower core to 'Olaia': Absolute values for SD-Olaia (black) and SD (red) (left) and efficiency (right).

The second and last quantity to be considered in this comparison is the energy. Like above, Fig. 5.6 shows the absolute values for both reconstruction on the left and the efficiency of SD to SD-Olaia on the right. As expected the energy for events reconstructed with SD-Olaia already starts at values $E < 10^{17}$ eV, which is also the range for the infill, whereas SD does not have events below $E \approx 10^{17.3}$ eV. The efficiency plot follows remarkably well the parametrization of the standard array [AB09], leading to a approximate full efficiency at 3 EeV.

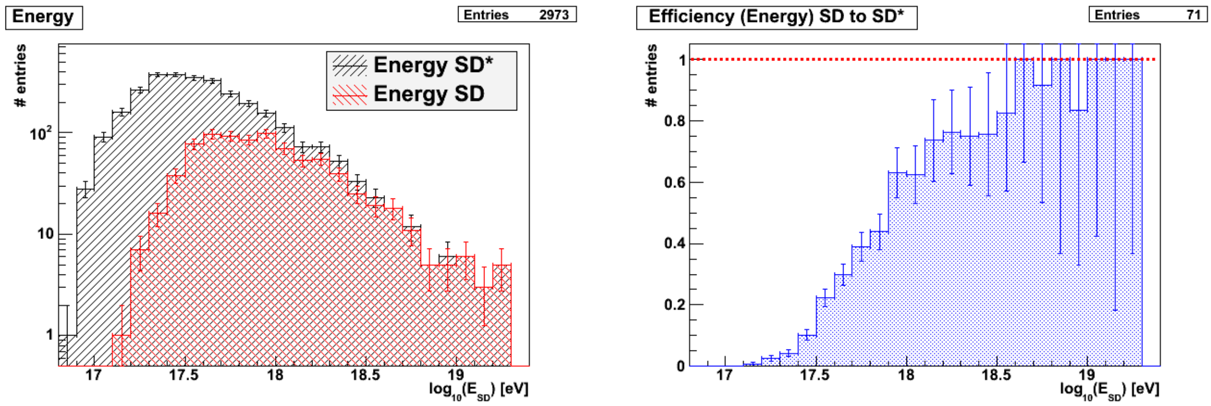

Figure 5.6: Energy (logarithmic) of the shower: Absolute values for SD-Olaia (black) and SD (red) (left) and efficiency (right).

5.3 Comparison SD-Olaia/Herald-RD

As we know now that the SD-Olaia reconstruction works really well and massively increases the statistics we can compare it to another reconstruction used at the PAO, namely CDAS Herald [Pie10a]. Several datafiles for this reocontruction method exist including one which just contains events where also 'Olaia' was triggered. As it was also used for analysis in the context of radio measurements it is called Herald-RD. This is exactly what we need for our comparison purpose.

Again the first thing to compare is the number of events which are reconstructed with both methods. As both methods use the same informations coming from the detector now, we expect a rather comparable output. While Offline SD-Olaia ends up with 3003 showers (as stated above), the Herald-RD succeeds with 2854 of these events. Obviously these numbers are biased towards Offline as we just check if events reconstructed with SD-Olaia are also done by Herald-RD and not the other way around. But nevertheless, as we get 95% in both reconstructions we can say that we have compatible data sets. This is also reflected in the core positions, where both reconstructions show the expected pattern (see Fig. 5.7).

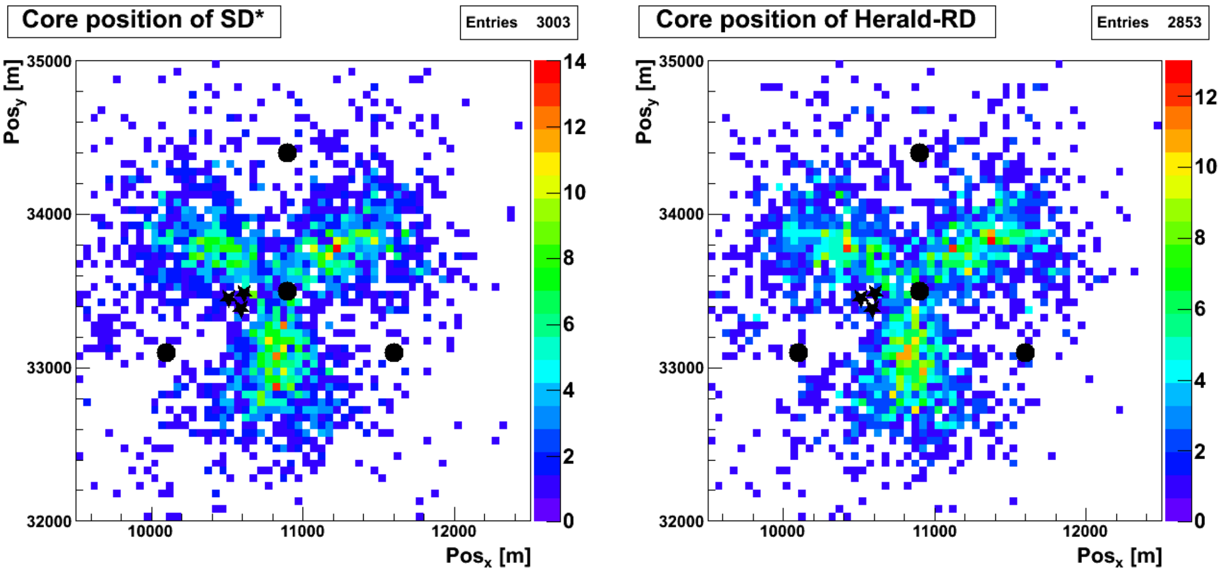

Figure 5.7: Core position for SD-Olaia (left) and Herald-RD (right).

A rather similiar good agreement can be seen in the angular residual as shown in Fig. 5.8. About 95% of all events have an angular reconstruction deviating less than 2°. Due to the increased statistics, the Rayleigh fit works a little better than before, but still the consistence is of such a quality, that the parametrization does not describe the distribution in a good manner. Using the 68% quantile the overall angular resolution can be determined to $\Omega \approx 0.49°$.

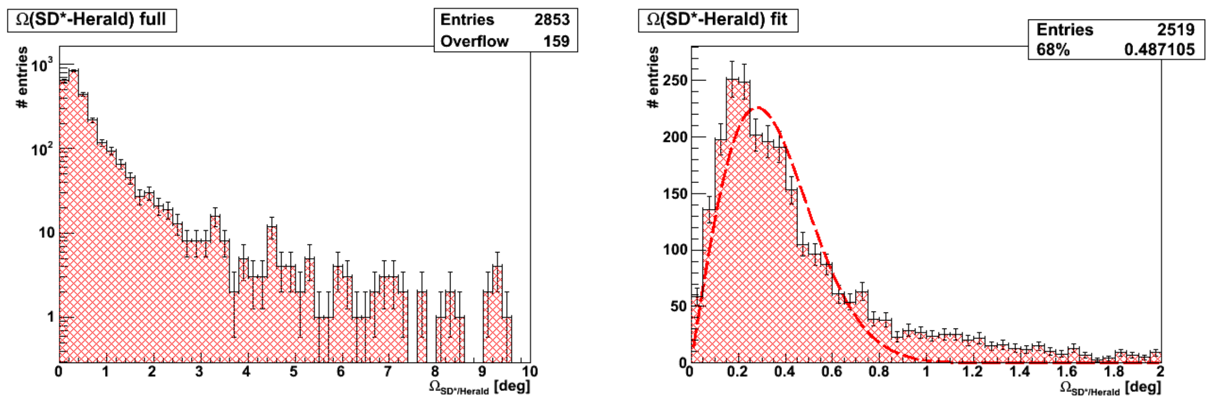

Figure 5.8: Angular residuals between SD-Olaia and Herald-RD for a large Ω range (left) and a zoomed plot with Rayleigh-fit (right).

Also the radial distance shows the same behaviour (see Fig. 5.9). The efficiency is of the order of 100% up to distances of about 2000 m. For larger values the fraction is varying randomly due to poor statistics.

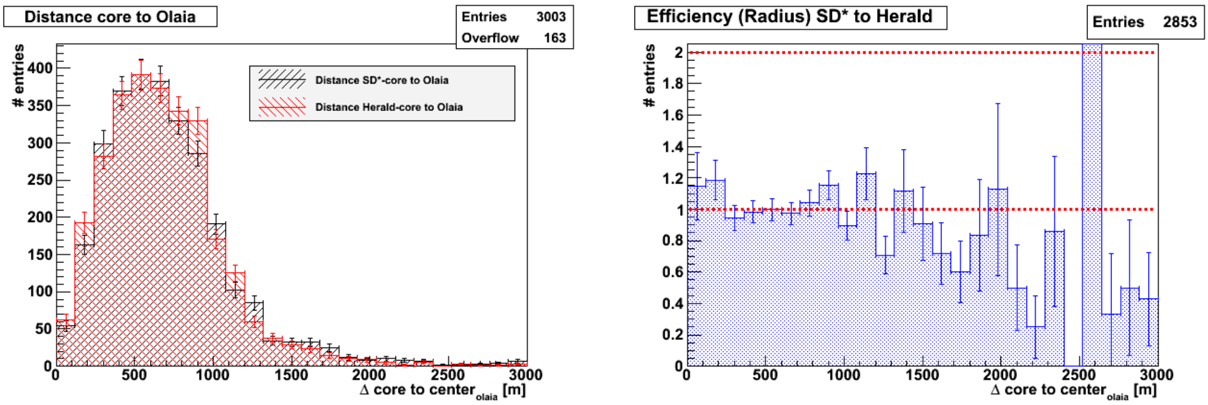

Figure 5.9: Radial distance of the shower core to 'Olaia': Absolute values for SD-Olaia (black) and Herald-RD (red) (left) and efficiency (right).

In contrast to the almost perfect agreement of the considered quantities above, the energy reconstruction yields a large discrepancy. As shown in Fig. 5.10 the absolute values of the reconstructed energy (left side) appear shifted by a non negligable amount. SD-Olaia yields a higher energy than Herald-RD. There are in total four different values for the calculated energy in the Herald reconstruction which use different estimators like the constant intensity cut (CIC) and/or different calibrations. The one used here is calculted by the CIC in connection with the latest FD calibration, which should be the best approach and is used for recent PAO publications, but which is in fact also the lowest one.

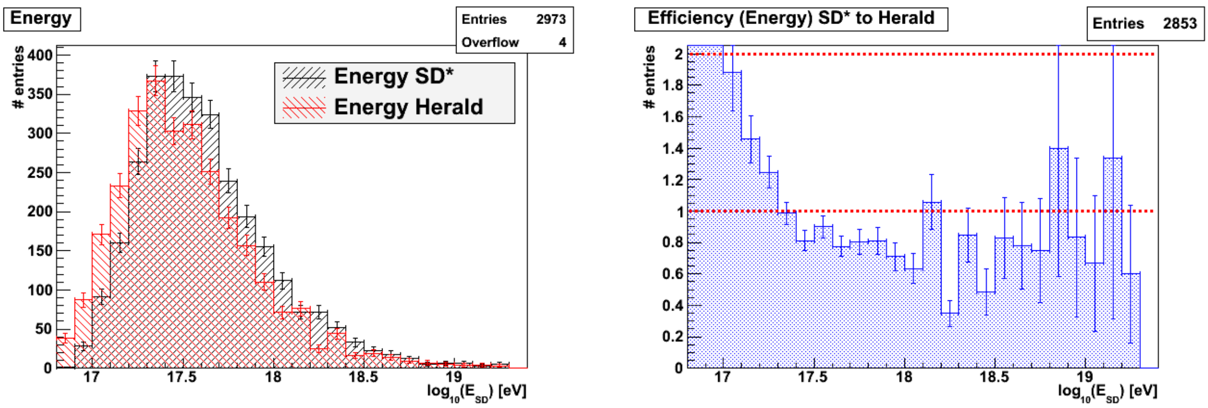

Figure 5.10: Energy (logarithmic) of the shower: Absolute values for SD-Olaia (black) and Herald-RD (red)(left) and efficiency (right).

To get a better feeling for the dimension of the shift we have a look at the relative deviation of the energies reconstructed by the different methods. Including all the events which have an energy value the shift can be determined to be $\Delta E/E \approx 17\%$ using a Gaussian fit. This is even more than an already noted shift of about 8% between Herald and the Offline Hybrid-Reconstruction [Sch07b]. As the Auger correlation paper [Pie10c] was based on

UHE-events we might look a little closer on these events in our dataset, which is depicted on the right side of 5.11. We can see that for these high energies the shift completly vanishes, which was also confirmed in [Sch07a]. This proves also the robustness and independence of the correlation signal to the applied reconstruction.

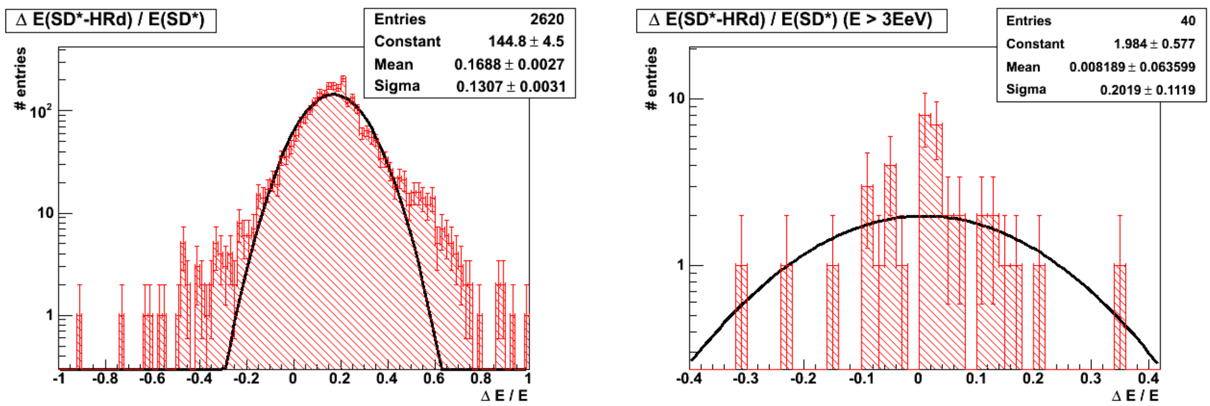

Figure 5.11: Relative deviation between Offline SD-Olaia and Herald-RD: All events (left) and for $E > 3$ EeV (right).

5.4 Coincident SD events using SD-Olaia

We succeeded in improving the Offline SD-reconstruction at least towards a gain in statistics and proved that it is compatible with other reconstruction methods. Now we want to use this tool for adressing the main question of this work, namely the comparison of SD events with radio data. As already mentioned the externally triggered setup was used for coincidence measurements during its year of data taking. The first analysis of these events was done with a Herald reconstruction for the SD data [vdB07]. Therefore, a compatible analysis using Offline is needed for comparing the results.

Hence, we start with a comparison of both Offline reconstructions, SD and SD-Olaia, again, but now restricted on the „coindata“ data set. This data set allows a rather simple selection of the related SD showers from an Offline reconstruction as the list containing all the radio events, 494 in total, was adjusted to have the same Event-ID for radio as used for SD and therefore grants an easy matching. Doing so, one gets 476 events with the improved SD-Olaia reconstruction versus only 148 showers for standard SD. The missing 18 showers for SD-Olaia are not completly lost during reconstruction, but are still recognized as event. Unfortunately, the geometry of the triggered detectors allows no reconstruction of the axis as all stations are more or less on a line (compare Fig. 5.12). This leads to a set of possible axis which can be formed by a 360° rotation around the line. Therefore, these events do not take part in the rest of the analysis. Nevertheless, one can say that the improved

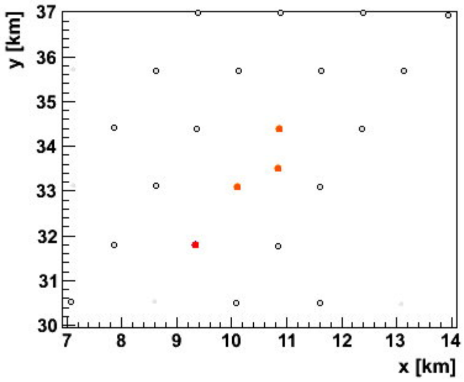

Figure 5.12: Event without reconstructed axis, due to 'on-line' alignment (tanks recoloured for visibility reasons).

SD-Olaia reconstruction yields all the coincident showers, whereas the the standard SD would provide only about 30% of the events.

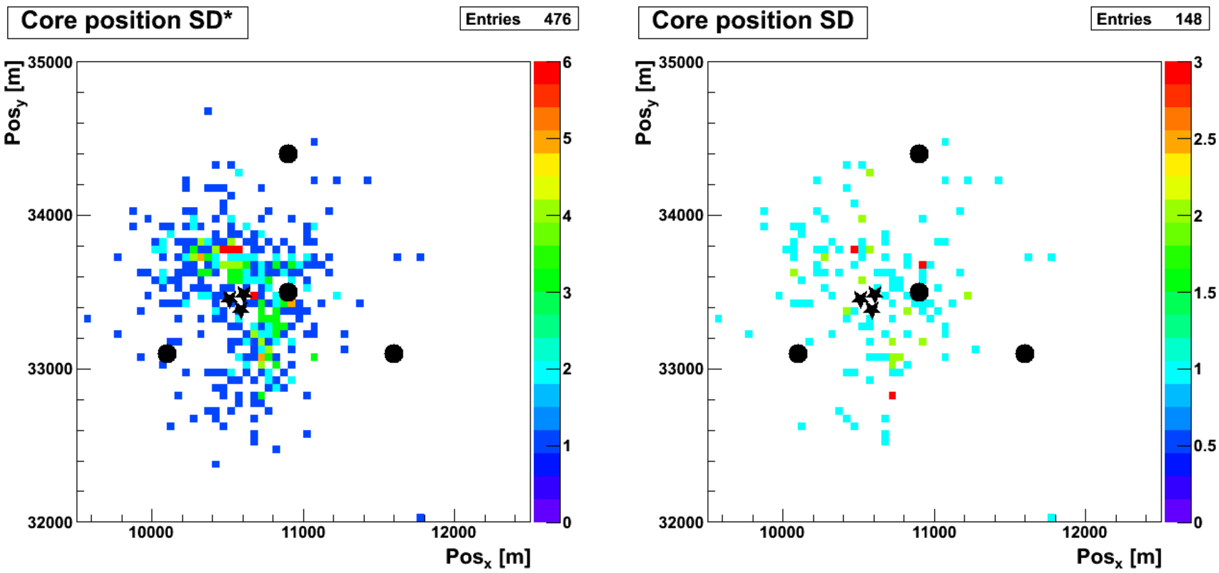

Figure 5.13: Core position for SD-Olaia (left) and SD (right) for coincident events with radio in the area around the 'Olaia'-triangle of SD tanks (black dots) and the externally triggered radio antennas (black stars).

Plotting the core positions of the reconstructed events (see Fig. 5.13) gives no rise for physical interpretation apart from the fact that for SD-Olaia we again achieve a slight appearance of the Mercedes pattern due to the increased efficiency between two SD tanks.

The angular residuals show the same good agreement of SD-Olaia and SD as for the „cointime" data set, all events lay in between a deviation of 8°. Still the Rayleigh function is not fitting very well, so we use the 68% quantile again which leads to an overall angular resolution of $\Omega \approx 0.99°$. As for the total sample discussed in 5.2 we don't gain (or lose) much in accuracy, but a lot in statistics which will be really important for the comparison with the reconstruction of the radio events.

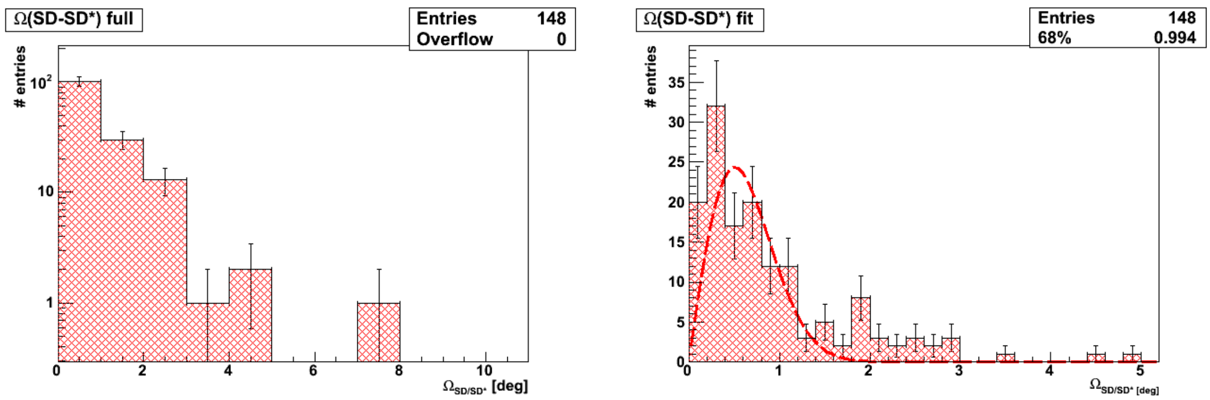

Figure 5.14: Angular residuals between SD-Olaia and SD for a large Ω range (left) and a zoomed plot with Rayleigh-fit (right) for coincident events with radio.

Both, radial distance (Fig. 5.15) and reconstructed energy (Fig. 5.16), show the same behaviour as for the „cointime“ data set. The efficiency for radii in the triangle around 'Olaia' is at a level of 20-30%, for higher distances a slight rise appears again, which is due to the energy correlation on the one hand and also to statistics on the other. Events for SD-Olaia start at an energy of 10^{17} eV, whereas the first SD events start at $10^{17.3}$ eV, leading to an equivalent efficiency at rougly 1 EeV for both reconstructions.

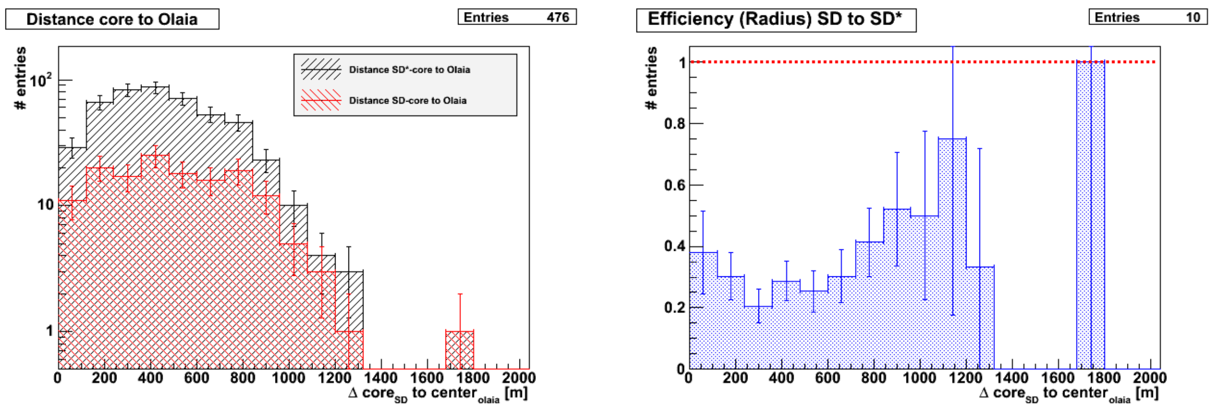

Figure 5.15: Radial distance of the shower core to 'Olaia' for coincident events with radio: Absolute values for SD-Olaia (black) and SD (red) (left) and efficiency (right).

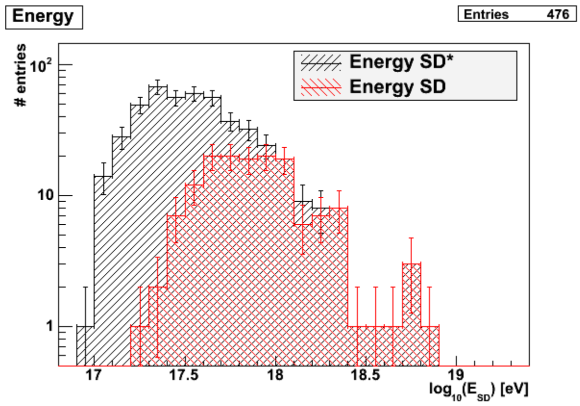

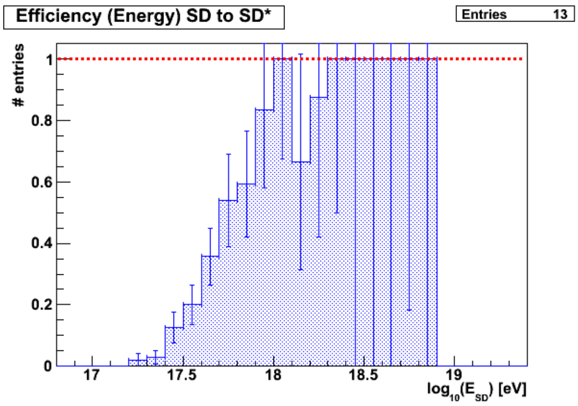

Figure 5.16: Energy (logarithmic) of the shower for coincident events with radio: Absolute values for SD-Olaia (black) and SD (red) (left) and efficiency (right).

5.5 Comparison SD-Olaia/RD

The last section of this chapter deals with the comparison of events reconstructed with SD-Olaia which were also measured with the radio antennas, i.e. successfully reconstructed using the radio functionality in Offline (RD). Note that the reconstructed quantites, except the azimuth and zenith angle, come from the SD, not the RD reconstruction. For this comparison a new selection criteria for RD has to be introduced, namely the signal-to-noise ratio (SNR). This quantity is applied during reconstruction as a quality cut in the event selection. For illustrating purposes we use three different SNR thresholds for the core position analysis, whereas we stick to the lowest one afterwards to have the best statistics. We define the SNR of an event as the ratio between the maximum of the signal in the signal window and the noise of that event. The noise σ is the standard deviation of the voltage values measured in the noise window of the radio trace, which is, again, outside the trigger window. A more detailed overview of the different windows is given in section 6.2, where the SNR itself is subject of the analysis. Tabular 5.5 gives the number of reconstructed events for the different SNRs.

SD-Olaia	476
RD SNR>4	99
RD SNR>5	47
RD SNR>9	15

Table 5.2: Number of events reconstructed with SD-Olaia or RD for the „coindata“ data set with a given SNR.

The first interesting thing is how the distribution of the core positions evolves with increasing SNR. Whereas the pure SD-Olaia reconstruction still includes the Mercedes-pattern as

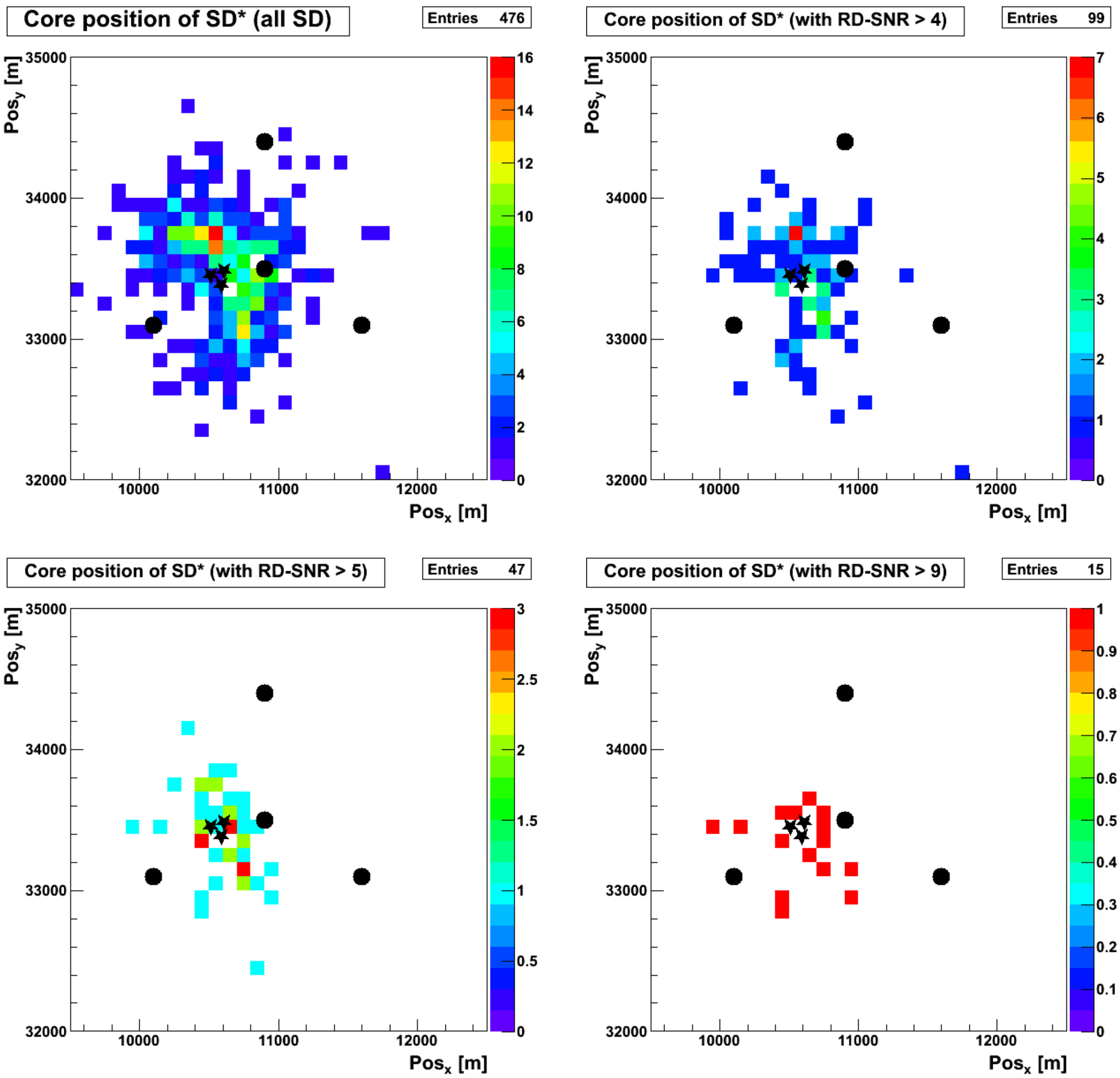

Figure 5.17: Core positions for SD-Olaia reconstruction (top left) and the corresponding events which were also reconstructable from radio data with a SNR $>$ 4 (top right), $>$ 5 (bottom left) and $>$ 9 (bottom right).

mentioned above cutting on the RD events removes this pattern and, as expected, shifts the center of the distribution towards the antenna grid. Increasing the SNR threshold and therefore reducing the number of reconstructed events shrinks the area of core positions to radial distances less than 600 m.

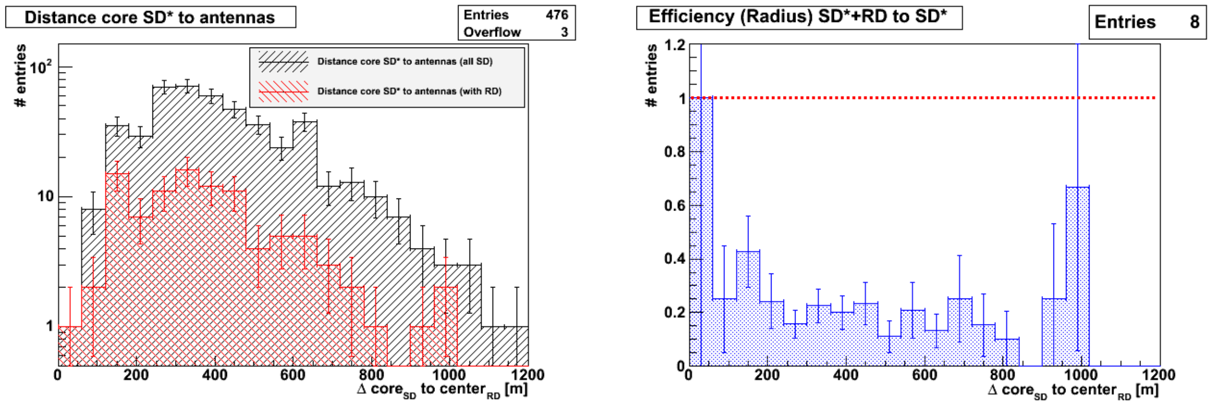

Figure 5.18: Radial distance of the shower core to 'Olaia' for RD events with SNR > 4: Absolute values for SD-Olaia (black) and SD-Olaia + RD (red) (left) and efficiency (right).

Comparing the radial distance of the reconstructed events which also have been measured with RD (Fig. 5.18) shows that there is no obvious cut-off for some distance, but just a slowly dropping efficiency for larger distances as one, of course, would expect. Also for the energy we do not see any detection threshold with RD (Fig. 5.19), but a slight rise in efficiency for higher energies, again rather expected. An interesting fact is that the events with the highest energies were not reconstructable with RD, although one would assume a high SNR for this events.

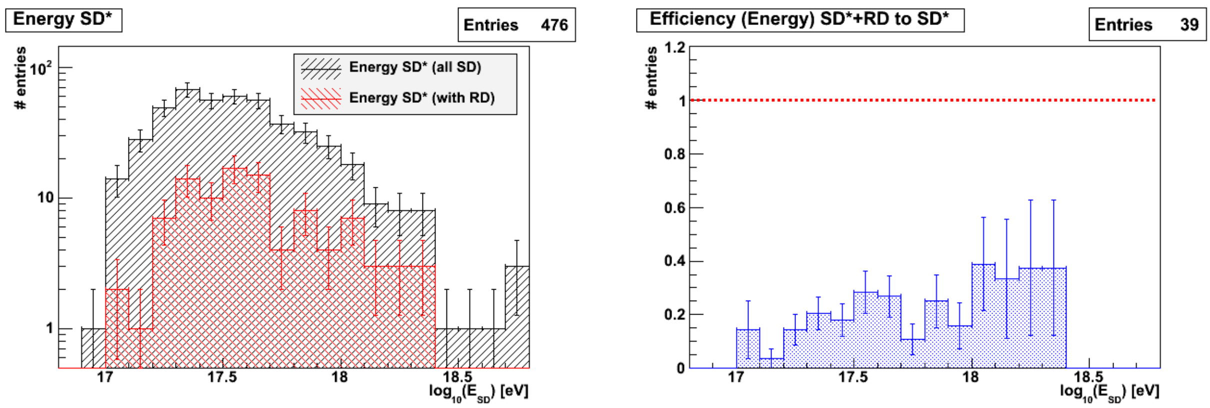

Figure 5.19: Energy (logarithmic) of the shower for RD events with SNR > 4: Absolute values for SD-Olaia (black) and SD-Olaia + RD (red) (left) and efficiency (right).

For the moment the zenith and azimuth angle are the only reliable quantities we can use from the RD reconstruction. Therefore, building the angular residual of the SD-Olaia and the RD can give a first hint on the directional accuracy one can achieve with radio setups, although the quality of the data is relatively poor. Figure 5.20 shows the results of this calculation for radio events with SNR > 4 and now, as the residual is not as good as the ones before, the Rayleigh function fits quite well. So the overall angular resolution can be determined to $\Omega = (9.6 \pm 1.6)^\circ$, which is of the same order as the one published in [EFG10] where an alternative reconstruction was used [Asc08] giving a resolution of $\Omega = (8.5 \pm 0.7)^\circ$. The agreement of the values is also a good cross-check for the consistency of both reconstructions. Going to higher SNR thresholds the resolution can even be reduced to $\Omega = (8.6 \pm 2.4)^\circ$ for SNR > 5 respectively $\Omega = (5.7 \pm 1.0)^\circ$ for SNR > 9. But due to the low number of total events in the data set, we run out of statistics for these cuts, so the values have to be considered with caution. Nevertheless the result is quite promising for even larger radio arrays as the setup at the BLS was of limited quality and triangulation with only three stations yields obviously quite imprecise results.

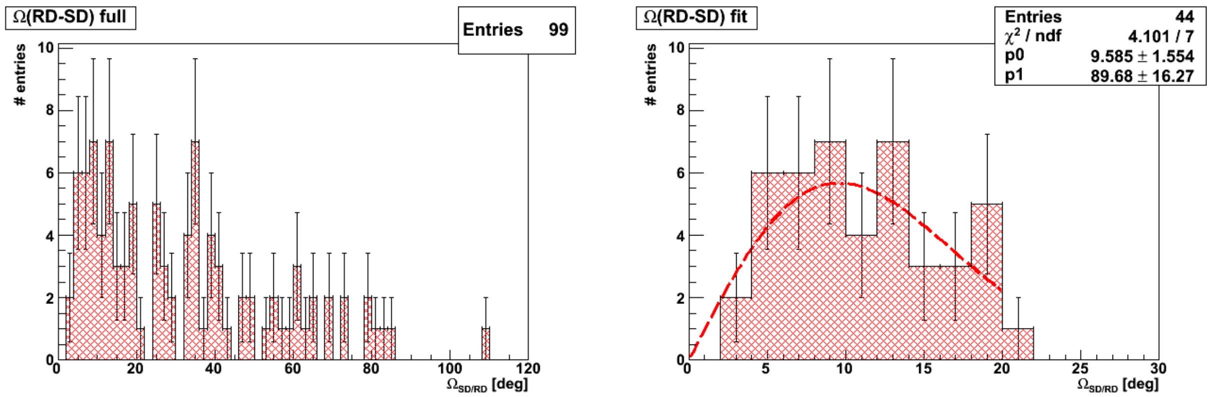

Figure 5.20: Angular residuals between SD-Olaia and RD (SNR > 4) for a large Ω range (left) and a zoomed plot with Rayleigh-fit (right) for coincident events with radio.

As a conclusion for this chapter we can summarize that the implementation of 'Olaia' in the Offline-Framework works really well and delivers as good results as the other considered reconstructions. A big improvement was achieved in statistics, leading to a factor of 3-4 more events reconstructed with SD-Olaia, leading to an almost 100% efficiency for the reconstruction of the coincident events of SD and the wired radio setup at the BLS. Additionally we have seen that the comparison of RD and SD-Olaia reconstruction yields a rather good angular resolution related to the quality of the detector setup. This is quite promising for a hybrid reconstrution of air showers with radio and surface detectors.

Chapter 6

Analysis of radio data

After succeeding with the first measurements of radio emission from CRs at the PAO, several hardware components were exchanged for R&D reasons, e.g. the small aperiodic loaded loop antennas (SALLA) [Krö09] and the digitizing electronics from the LOPES^{STAR} experiment were used. Therefore, also the trigger modus changed from external- to self-triggering. The setup took data in this configuration from October 2008 until August 2009. Then, the antennas have been exchanged to a SALLA of extended size. A set of selected events is used for some basic analysis like angular distribution of arrival directions, etc. and coincidence search.

6.1 Analysis of raw data

The first approach to this data set was done by an analysis of the raw data without any reconstruction. So the only information we get is the timing (GPS-Second and GPS-Nanosecond) of the single RD station triggers. Using these quantites we can perform a rude analysis of the time differences between RD trigger and SD events for the same time period or the time differences of the RD triggers to each other. Figure 6.1, left side, shows the time difference Δt for a RD trigger with all the SD events in between 30 s before and after. Unfortunately, the number of SD events in such a short time period is not very high. Requiring one specific tank to be triggered, we end up with roughly 40 events per day. The almost flat distribution yields no useful information but the RD triggers appear without any correlation around a SD event. The difference between two RD triggers in Fig. 6.1 shows the expected exponential drop off.

Zooming on $\Delta t < 1$ s a periodic structure can be seen on top of the the exponential. (see Fig. 6.2).

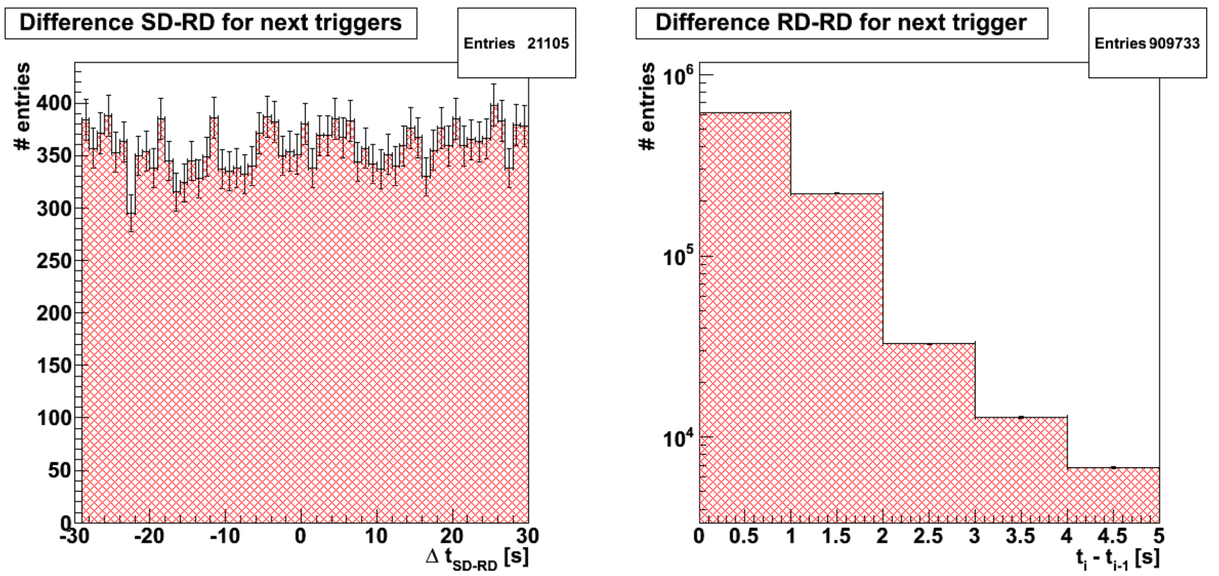

Figure 6.1: Time difference between a RD trigger and the closest SD events (left) and between to neighbouring RD triggers (right).

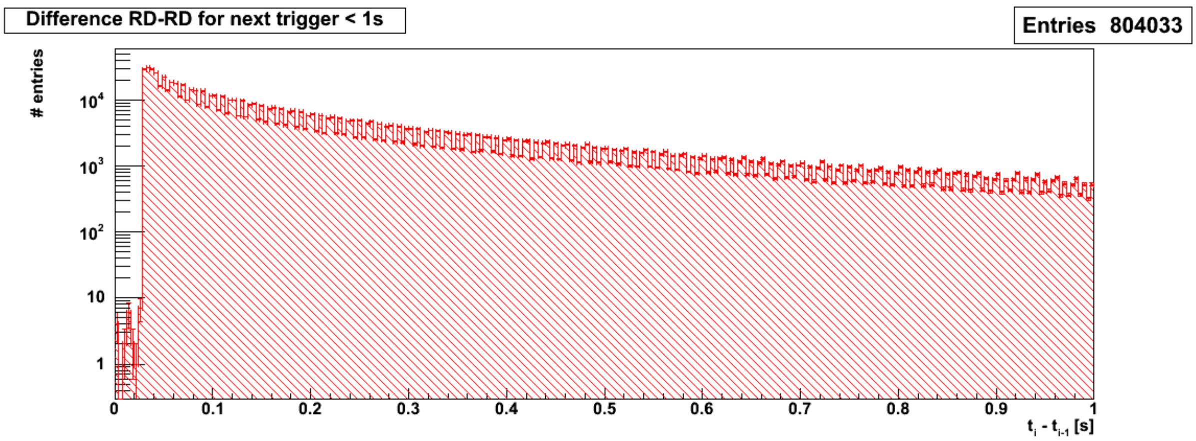

Figure 6.2: Time difference between neighbouring RD triggers for $\Delta t < 1$ s.

Fitting a function of the form

$$f(x, \alpha, \beta, \gamma, T) = \alpha \cdot \exp^{-\beta x} + \gamma \cdot cos^2(\frac{2\pi}{T} \cdot x) \tag{6.1}$$

to the first 100 ms of the distribution yields a time period T of 0.02 s corresponding to a frequency of 50 Hz. This is just the frequency for standard power-lines, which are also deployed in the PAO array and unfortunately one being rather close to the BLS setup.

To confirm the real evidence in the data and maybe to find a possibility to exclude such 'events' from further analysis, one can try to find the phase of the power line by plotting

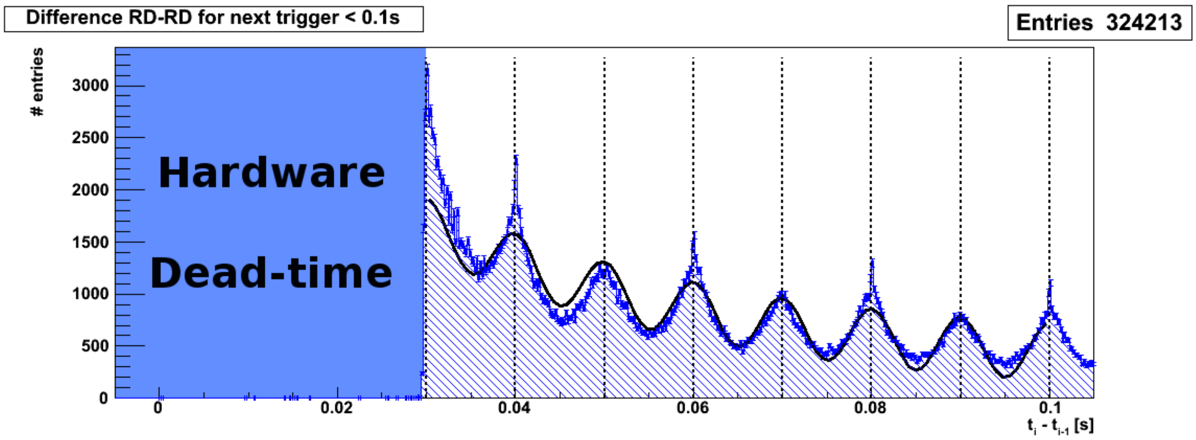

Figure 6.3: Time difference to the preceding RD trigger for $\Delta t < 100$ ms.

the absolute time information of one trigger with a modulo operation of the time period of $T = 0.02$ s. This should lead to a strongly peaked structure in the graph at the value of the phase shift, which is obviously not the case as can be seen in Fig. 6.4.

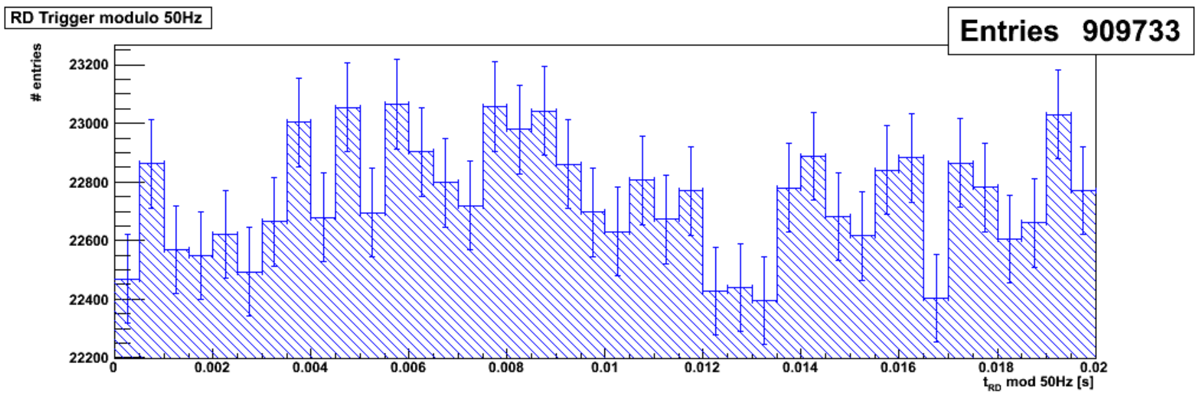

Figure 6.4: Absolute GPS time for raw data modulo $T = 0.02$ s.

As a last approach one could assume that the phase itself is also a time-dependent quantity and not stable even on the order of days. Therefore, the modulo operation is plotted as a function of time. As the number of events is not constant over time the number of entries in each y-bin is normalized by the number of all entries in the corresponding x-bin. The plot can be seen in Fig. 6.5 and is rather uniformly distributed over the whole period. A time dependent phase should appear as a drifting structure in the plot, but apparently it does not. Nevertheless it is quite clear that these signals come from the power line and so different methods for removing them from the sample have to be found. For the coincidence search we need different approaches to get to the selection of EAS-events.

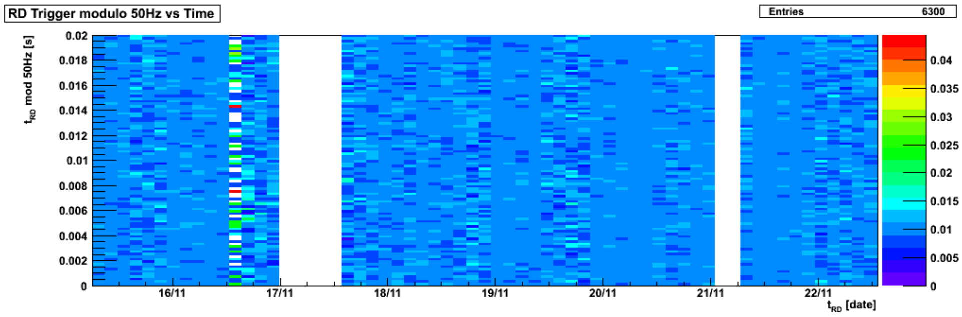

Figure 6.5: Absolute GPS time for raw data modulo $T = 0.02\,\mathrm{s}$ as a function of time.

6.2 Analysis of reconstructed data

First the whole data set is reconstructed as this leads to a natural discrimination for the noise events. Most of them are thrown out by the reconstruction due to the fact that the identified peaks in the trace of each station do not entail a physical arrival direction in the plane fit. E.g. the time difference between the individual station peaks is not consistent with the expected speed of the electromagnetic wave, which is the speed of light c. The obvious criteria to identify a peak in the voltage trace as a signal-pulse maybe originating from a cosmic ray is that the height of that peak has to exceed a given SNR (defined as $\sqrt{\mathrm{Amp}^2_{\mathrm{peak}}/\mathrm{noise}^2}$).

The Offline RD reconstruction offers the user the opportunity to define certain windows for calculation of the needed quantities. In general, the trigger algorithm defines the position of the signal window. Figure 6.6 shows, that most of the traces reach their maximum amplitude at $12.5 \pm 0.3\,\mu$s, therefore the signal window is defined from $11 - 14\,\mu$s [Mel10]. The noise of the respective measurement is determined from the first 4 μs of the voltage trace that are recorded when a trigger has occurred. The origin of the double peak structure is not really understood, but also of minor importance for the following analysis. Scanning the whole voltage trace leads to a greater probability to find stochastically high peaks originating from noise. Thus, the advantage of using a small search window is that the SNR can be reduced. To keep the balance between loss of relevant signals and computing time for the reconstruction the SNR threshold was set to 5 for the following analysis. Up to now a data sample of 17433 events has been reconstructed, which will be used for the following analysis.

The timing itself is also a quantity, which needs to be studied, as we require a good absolute timing as well as time resolution for the reconstruction of the arrival direction. The left side of Fig. 6.7 shows the total distribution of the GPS-Nanosecond for the reconstructed events. We would expect a flat distribution, but we see a excess of higher values. This is also visible in the time-dependent plot in Fig. 6.7, right side, which is rather rather

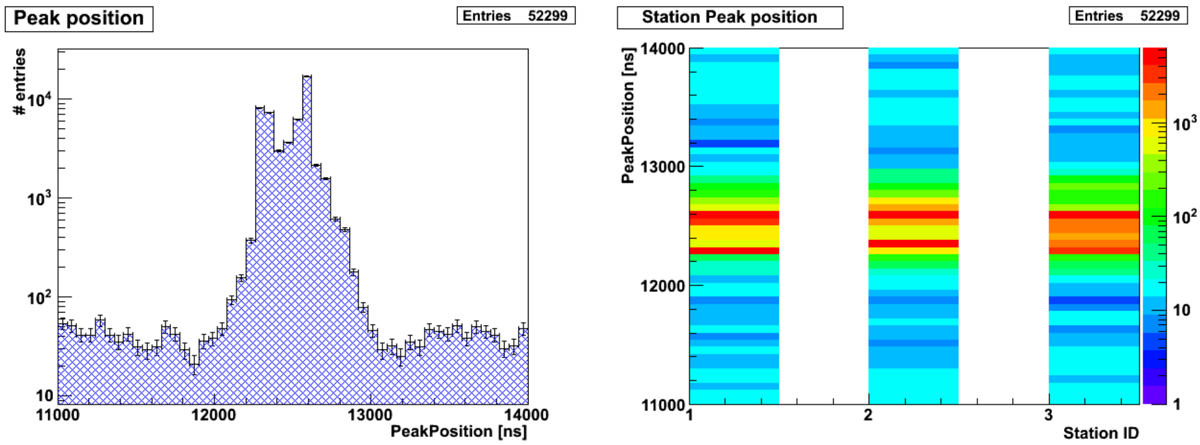

Figure 6.6: Amplitude peak position of reconstructed events. All stations (left) and for the three single station (right).

uniform, but has a large asymmetry at $911.32 \cdot 10^6$ s. We will need more reconstructed data to give a reasonable statement on the origin and duration of this feature. A first guess would be some configuration work on the electronics or some man-made noise source at that period emitting at a frequency of roughly 1 Hz or multiples which would explain the higher population of events if pulsing in the rear part of the GPS-Nanosecond.

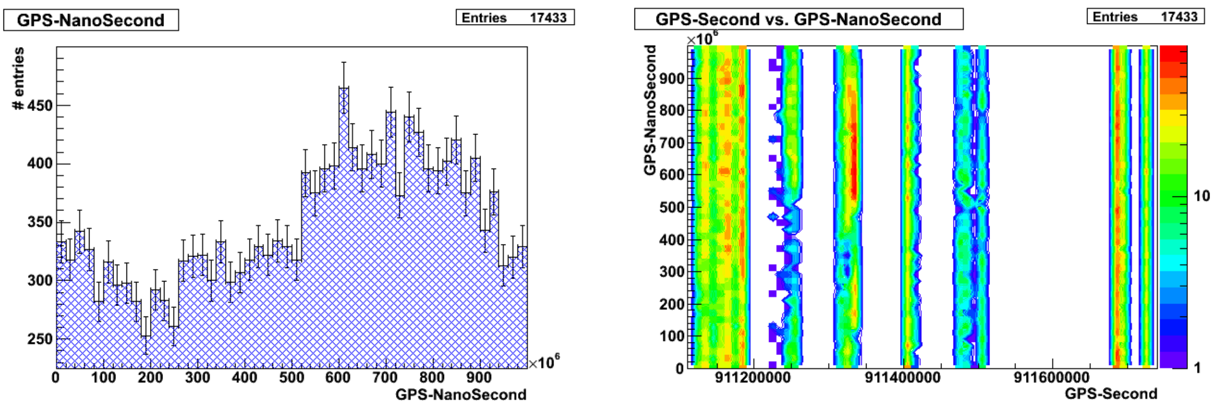

Figure 6.7: Distribution of timing information: GPSNanoSecond total (left) and with respect to time (right).

6.2.1 Delta t

The first thing we want to check with the reconstructed data set is, if the presence of the power line events is remaining in the reconstructed sample. Therefore, we consider the Δt

distribution for values less the 0.1 seconds again. As the statistics are much lower than for the raw data and the distribution is not as smooth as the one above, we again fit it with the superposition of a cos^2-function and an exponential as in equation 6.1, now with a fixed time period of $T = 0.02\,\mathrm{s}$.

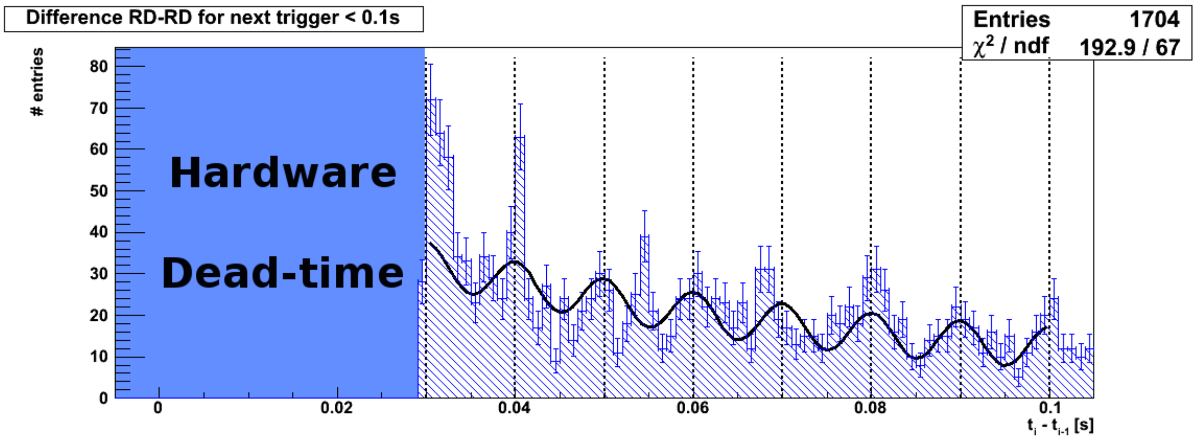

Figure 6.8: Time difference between neighbouring RD events for $\Delta t < 100\,\mathrm{ms}$ in the reconstructed data sample.

As one can see in Fig. 6.8 the fit still works quite well. This leads to the assumption that also a threshold of SNR > 5 might not be enough to completly remove the power line events from the data set just by reconstruction. Additionally, we plot the angular distribution of all events which are in a $\pm 5\%$ window around the 50 Hz peaks. In Fig. 6.9 we see a huge contribution for inclined showers with $\theta > 60°$, which confirms the presence of man-made noise in the data. The hottest spot comes from an azimuthal direction of $\phi \approx 215°$. Unfortunately, up to now there is no known noise source at this direction. Nevertheless, to avoid such events one could think about simply cutting out data from the 50 Hz part in the time domain.

Another possibility is to correlate the timing of these events with their SNR. Therefore, we plot the two-dimensional distribution of the SNR with respect to the event time modulo $T = 0.02\,\mathrm{s}$ (see Fig. 6.10). Whereas the single event distribution yields nothing obviously apparent, the integrated one shows a clear excess at the 50 Hz lines (dotted). This dense population of events stays up to a SNR of about 40, so cutting at this value could reduce the number of 50 Hz events, but would also throw away a lot of useful information. One could refer to this as a quality cut when dealing with higher statistics, but it is not senseful for this basic analysis.

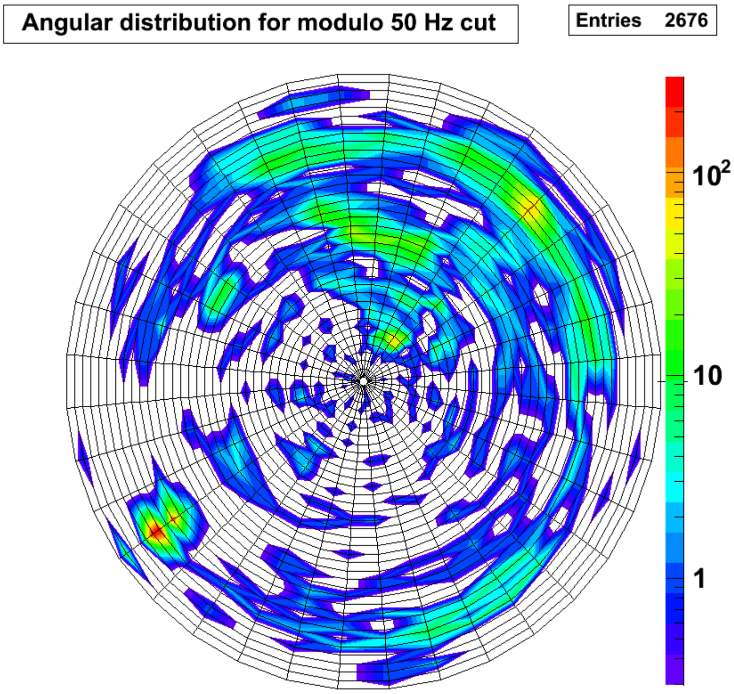

Figure 6.9: Angular distribution of the 50 Hz events with θ on the radial axis and ϕ on the angular axis. East to the right, north to the top, zenith in the center.

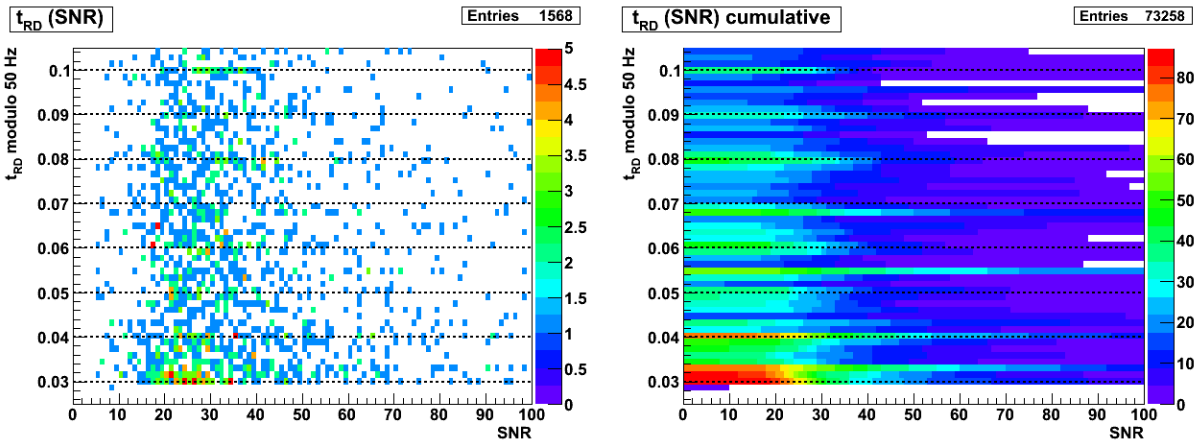

Figure 6.10: Distribution of SNR with respect to event time modulo $T = 0.02\,\mathrm{s}$. All events (left) and cumulative (right).

6.2.2 Signal to noise ratio

To check whether there are possibilities to increase the SNR without losing to many events we have a closer look at its distribution. As it is calculated via the amplitude (AMP) and the noise (RMS) of an event we scan these parameters first. The all station distribution of AMP and RMS (see Fig. 6.11 and 6.12, left side) look quite as expected. The amplitude has a peak at about $50-100\,\mu$V/m, then drops rapidly to a small plateau at $200\,\mu$V/m and vanishes almost completly afterwards. The same can be seen for the noise, which drops exponentially from a peak at 3 μV/m and flattens out for values larger than 15 μV/m.

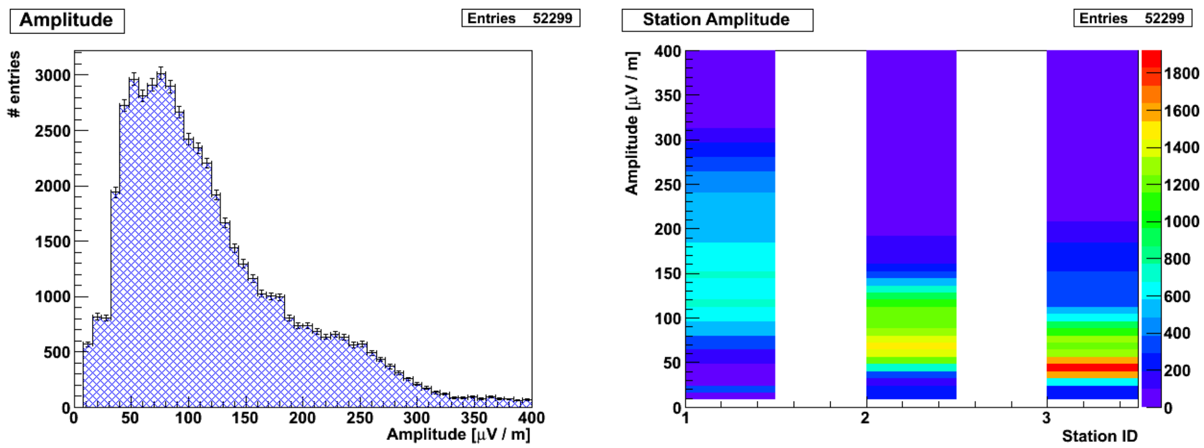

Figure 6.11: Distribution of AMP: All stations (left) and single stations (right).

Looking at the distribution of the individual stations the situation is different (see Fig. 6.11 and 6.12, right side). We see a clear shift in the amplitude of the stations with respect to each other, station 1 having the highest mean and also the widest spread of the values. Station 2 and 3 look more similar, which is also reflected in the noise distribution. Also here we see that station 1 is slightly shifted upwards. We adress this effect to some mismatching in the antenna electronics (maybe the LNA), which results in a differently scaled power spectrum. Unfortunately this shift, if not caused by physics, has also an impact on the reconstruction of the shower geometry.

A two-dimensional combination of the two values is shown in Fig. 6.13, left side. We can see that most of the events are in the noise regime of $2-5$ μV/m with a corresponding amplitude of $30-180\mu$V/m. Also higher amplitudes are reached but mostly in the low noise regime, so cutting above a certain noise level, e.g. 10 μV/m, would decrease the number of events without a general loss of quality. Calculating the SNR now for all stations yields the plot in Fig. 6.13, right side. We see a nice signal peak which can be fitted with a Landau function, leading to a most probable value of SNR $= 25.4\pm0.1$ with $\sigma_{\mathrm{SNR}} = 7.4\pm0.1$. This is quite surprising as one would expect a Gaussian function for the signal of real events on top of the exponential noise drop-off. The reason for the almost perfect agreement of

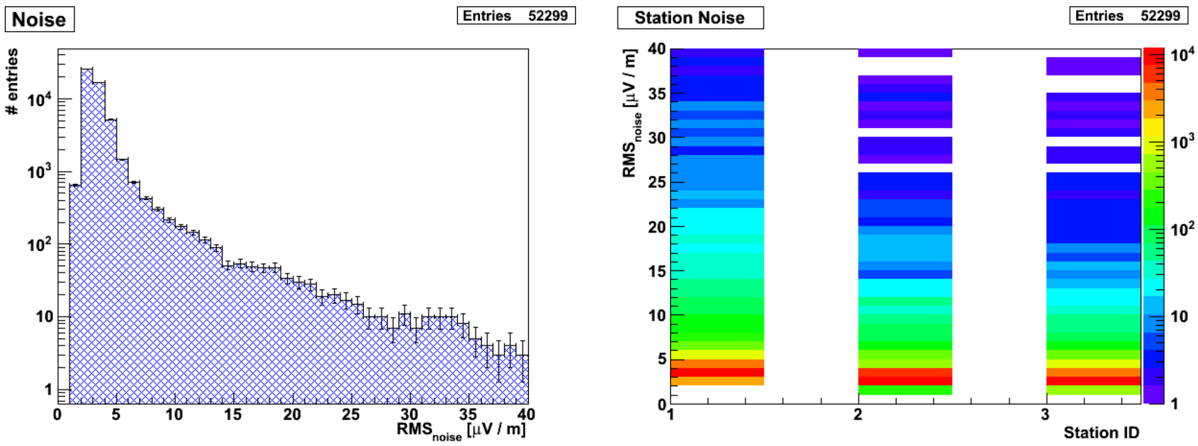

Figure 6.12: Distribution of RMS: All stations (left) and single stations (right).

the Landau function might be the above mentionend scaling in the amplitude and noise spectra, but is still under investigation. The small peak at SNR $= 7$ is adressed to the remaining noise peak which should extend to a high number of entries for lower SNR, but is not in the data as the online trigger in the digital electronics does not select them for data-acquisition. This will be confirmed in section 6.2.5.

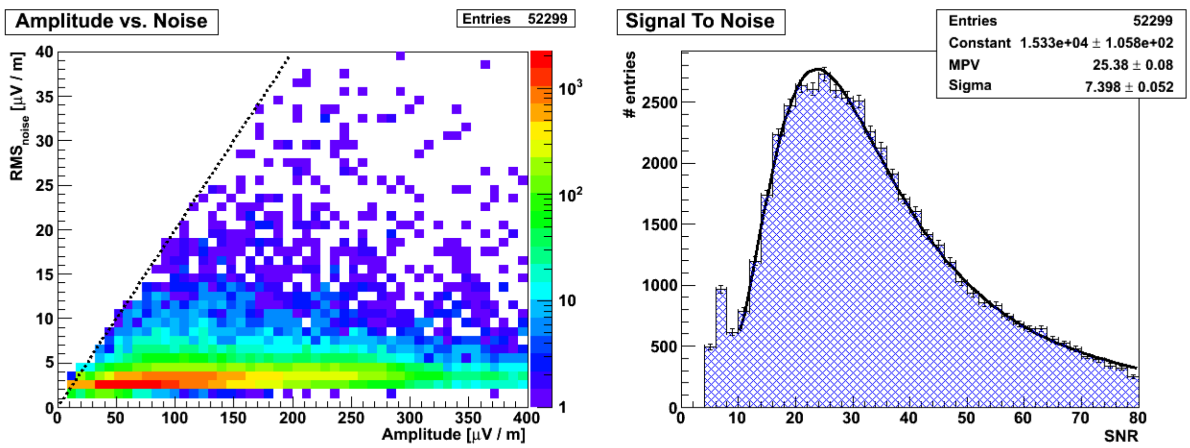

Figure 6.13: Two-dimensional distibution of AMP and RMS for all stations (left) and distribution of SNR for all stations (right) with Landau fit.

Some more interesting features can be seen in the angular dependence of the SNR in zenith as well as in azimuth direction. Figure 6.14, top left, shows the maximal value of the SNR of all three stations in one event. From left to right follow three equidistant partitions in zenith direction, the first ranging from 0° to 30° and so on. It is clearly visible that for SNR between 10 and 80 the inclined events give the major contribution to the whole sample, whereas for really low SNR also lower zenith angles are prefered. For higher SNR the events with a zenith angle below 30° go up to about 50% of the sample, but as one can see in the maximal value distribution, the statistic is very low there.

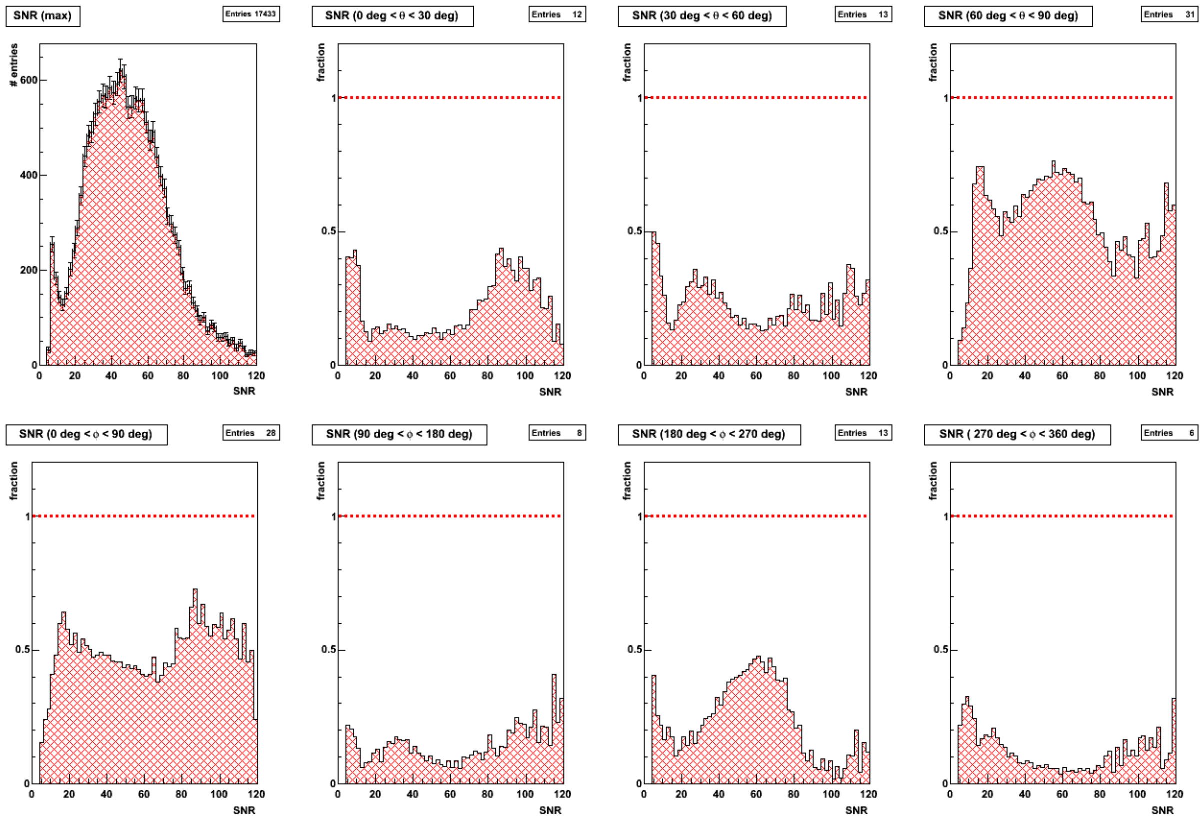

Figure 6.14: Angular dependence of the SNR. Top row: All events and three equidistant zenith partitions from 0° to 90° (left to right), bottom row: four equidistant azimuth partitions from 0° to 360°.

Also the azimuth distribution in Fig. 6.14, bottom row, reveals some substructures. Almost the whole sample is dominated by events coming from 0° to 90° respectively east to north, except a dip ranging from SNR values between 30 and 80. In that regime half of the events come from the opposite direction, meaning 180° to 270°. The other two angular quadrants are populated rather poor. As we don't expect CR events in such a highly directional grade it is most likely to assume a man-made noise source at this position.

6.2.3 Angular distribution

For further investigations of potential noise directions we study the two-dimensional angular distribution while cutting on the SNR. The disappearance or survival of hot-spots with increasing SNR should show the directions of possible man-made events. Figure 6.15, top left, shows the angular distribution for events with a SNR > 5, which means all events. We can see two inclined hot spots, which correspond to the dominant regions of the previous section and can now be adressed more accurately to 50° respectively 215° in azimuth direction, both at a zenith angle of about 70°. Additionally, we get a small increase in the density of events at $60° - 110°$ azimuth and $20° - 50°$ zenith. Plotting this for the lower SNR regime ranging from 5 to 25, the whole distribution becomes more uniform and smoother, except the two hot spots mentioned above, where the one in the north-east ($\phi = 50°$) is more dominant now.

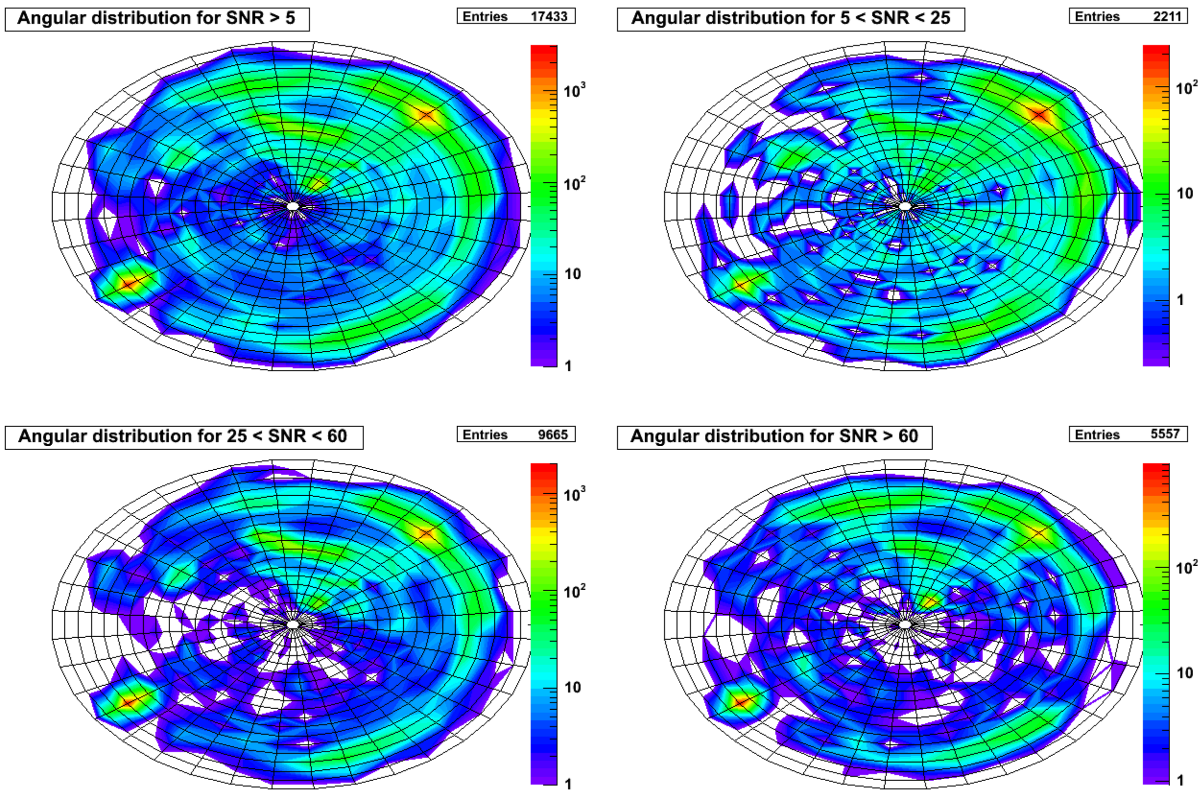

Figure 6.15: Two dimensional angular distribution of reconstructed events with different SNR thresholds: SNR > 5 (top left), $5 >$ SNR > 25 (top right), $25 >$ SNR > 60 (bottom left) and SNR > 60 (right). East to the right, north to the top, zenith in the center.

Going to SNRs between 25 and 60 the source in the south-west ($\phi = 215°$) is more distinct and the higher density for events from the north is present again. Also for the highest SNRs both spots are still visible, additionally a prominent source appears at 55° azimuth and 10° zenith. Whereas this one can not be identified really easily as it has to be something rather stable in the sky (a guess would be some kind of geo-stationary satellite emitting in the radio regime), the very inclined source in the north-east is meanwhile well-known. Several antennas on 'Cerro El Diamante', a nearby hill, produce a constant noise which is recorded by the detectors. A picture of the antenna stations on top of the hill can be seen in Fig. 6.16. For the dominant source in the south-west no candidate origin was revealed up to now.

Figure 6.16: Antennas on top of 'Cerro El Diamante'.

6.2.4 Coincidence search

After showing some basic analysis of the data gained with the self-triggered radio setup at the BLS we want to come back to the second main approach, the coincidence search. As before the most simple attempt is just to calculate the time difference between a SD event and the closest RD events. If the timing of both measurements were completly reliable and accurate, coincidences should appear in an interval close to $\Delta t = 0$ s, the sign depending on the direction of the shower with respect to the position of the antennas and the concerned SD tanks. Unfortunately, without the cross-check to the SD timing the RD GPS timestamp could suffer some shifts due to effects like missing leap seconds or other small-scale uncertainties. Nevertheless, a Δt plot gives a first overview on the situation of timing differences. We end up with the distribution depicted in Fig. 6.17, which is rather uniform, but has also a peak at $\Delta t = 0$ s. When checking the concerning entries we find, that there is one SD event which corresponds to a large number of very fast succeeding RD events, which leads to this peak in the plot.

As we found no coincidences on the small time scales (seconds) we might also want to look on larger scales (hours/days). A reason for such huge time shifts might be a wrong GPS stamp, the calculation at starting time or some leakage / failure while saving these

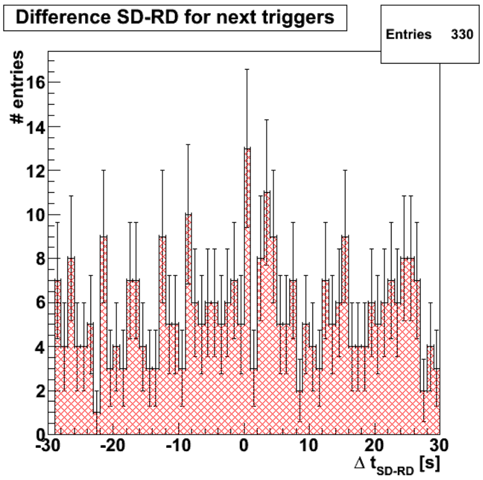

Figure 6.17: Time difference between a RD event and the closest SD events.

informations. Creating Δt plots for such scales would not be very senseful, so another procedure was applied: First of all we compare the angular reconstruction of *every* RD event in the data set with *every* SD event and construct the angular residual $\Omega_{SD/RD}$ and the SNR_{RD} for every combination. Afterwards we create Δt plots while cutting on Ω (decreasing) and SNR (increasing). As the directional matching becomes more and more accurate due to the lower angular residual, the radio events should become more likely to be real CR events with the raise in the SNR. Therefore, we can search for peaks in the time differences for varying combinations of thresholds.

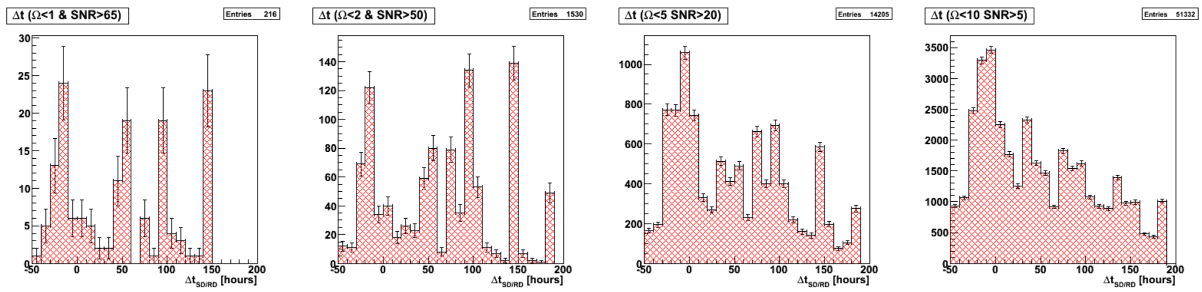

Figure 6.18: Time difference between a RD event and a SD events with cuts on Ω and SNR.

Figure 6.18 shows the time differences for several cut combinations and we obatin very peaky structures. Some peaks are present in several plots, e.g. the ones at $\Delta t = 40$ hours or $\Delta t = 150$ hours, some appear only once. Unfortunately with the current statistics no real interpretation can be done, as the distribution of the RD events in time is not uniform and therefore several events of one radio run belong to one SD event in these plots, leading to such dominant peaks. So far this attempt of coincidence search was not successful, but will be carried on until a reasonable statistic is reached. To get a better imagination

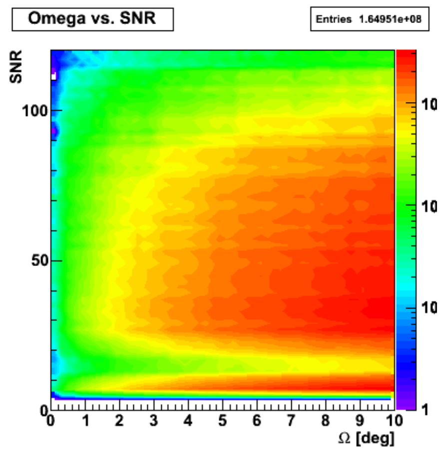

Figure 6.19: Two dimensional distribution of Ω and SNR.

of the distribution of angular residual Ω and SNR, Fig. 6.19 shows the two-dimensional distribution of this quantities in the range, which was considered in the Δt plots before. Going from the lower right to the upper left corner we see that we run out of statistics really soon for strict cuts, whereas most of the events are located at SNRs of 50 and $\Omega \approx 10°$.

6.2.5 Influence of the window selection

At the start of this chapter the possibility for choosing specific regions for calculation of the noise / RMS and finding the signal was described. The most important part here is the signal window as it defines the candidate positions for the peak in the trace. Therefore, defining a false range for this regime should have a huge influence on the results of the reconstruction as the algorithm will only find some minor peaks in the trace, which do not correspond to the triggered signal, or nothing at all. This will of course lead to a wrong arrival time alignment and accordingly a wrong direction reconstruction. Unfortunately, while starting with the reconstruction for this part of the work, a wrong value for the signal window was assumed due to a miss-leading comment in the concerning xml-card. So a lot of statistics was produced which now at least can be used for confirming the statements made above.

First we investigate the SNR respectively the ratio of amplitude to noise. We see a high contribution of values with amplitudes of 10-12 and a corresponding noise of about 2 and from that hot spot decreasing to higher values for both variables along the upper limit (black line). Calculating the SNR from these quantities leads to the distribution shown in Fig. 6.20, right side, with a maximum at SNR $\approx$ 5.5 and a steep drop off afterwards with almost 80% of all events in between the interval from 5 to 7. This is just what we expect, as a lot of „noise“-like events should enter the reconstruction due to the wrong signal window. The signal peak as seen in Fig. 6.13 is completly missing, therefore we can state that, using this window, we are just reconstructing noise.

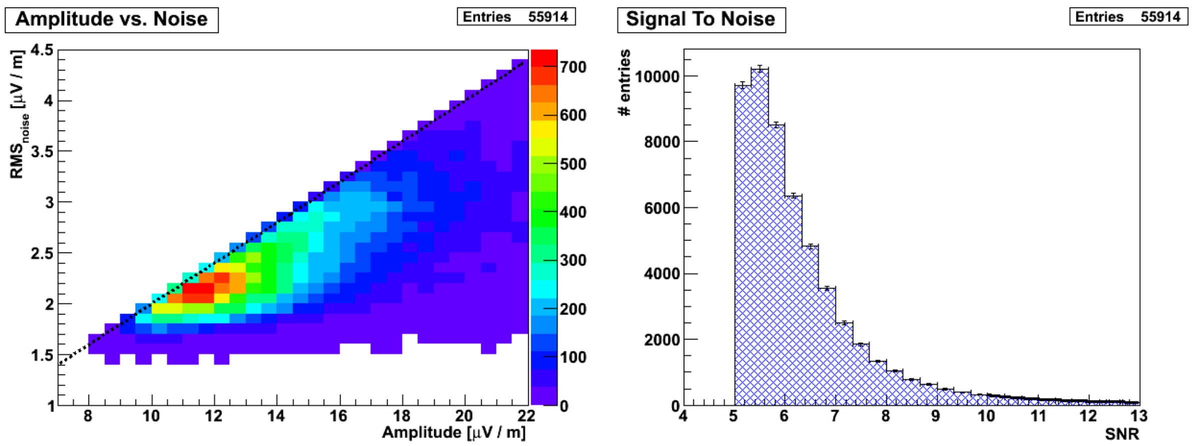

Figure 6.20: Two-dimensional distribution of amplitude and noise for all events (left) and SNR distribution for all events (right), both using a wrong signal window.

Due to this fact we have a look at the power line events again. Figure 6.21 shows the time difference between two neighbouring RD events with $\Delta t < 100$ ms. Already by eye we might be able to see the periodic distribution as found in Fig. 6.3. Fitting the function of equation 6.1 to this data yields a rather good χ^2/ndf of the order of 1. This also confirms our statement that most events which can be reconstructed when using this signal window are due to noise, as this fit shows clearly the remaining evidence of the power line in the data. Moreover it reveals the constant presence of the 50 Hz in the data.

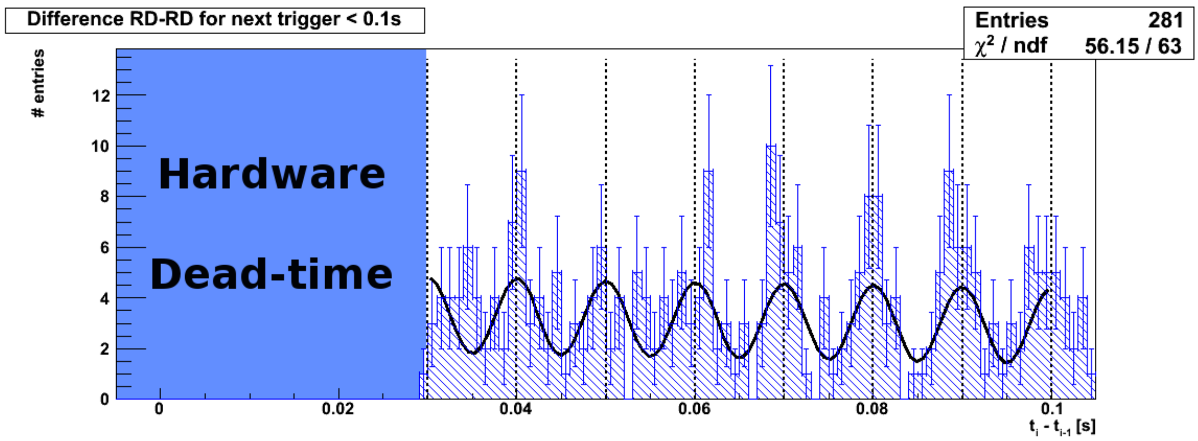

Figure 6.21: Time difference between neighbouring RD events for $\Delta t < 100$ ms in reconstructed data using a wrong signal window.

We now know that our data set is containing rather small numbers of real radio signals which might correspond to EAS, but mostly noise, so one can have a look at the angular distribution of this pulses to find more candidate directions for noise sources. In Fig. 6.22 we show the distributions for events with SNR $>$ 5 and SNR $>$ 20 as the most prominent regions are still visible at the higher threshold and in between nothing interesting appears. We find a hot spot at $\phi \approx 50°$ and $\theta \approx 75°$, which corresponds to 'Cerro El Diamante' again. Additionally we see a non-uniform distribution at $\phi \approx 270°$ and $\theta \approx 10°$, this is not really expected as it is a source almost vertical in the sky. A possible candidate would again be a geo-stationary satellite.

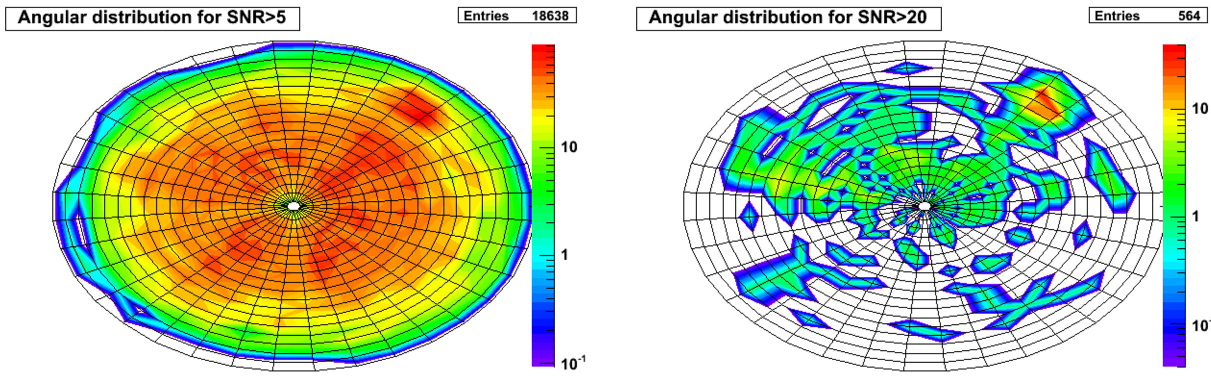

Figure 6.22: Two dimensional angular distribution of reconstructed events with different thresholds using a wrong signal window: SNR $>$ 5 (left) and SNR $>$ 20 (right). East to the right, north to the top, zenith in the center.

As a last quantity we check the angular dependence of the SNR using the same equidistant partitions as above for zenith and azimuth. It is clearly visible in the zenith distribution, top row Fig. 6.22, that for SNR $<$ 12 the inclined showers contribute very rarely as they have only a fraction of about 15% of the total events. For higher values of the SNR they catch up, so that in the tail of the SNR distribution the fraction is roughly 1/3 for each of the partitions.

Also the azimuth distribution in Fig. 6.23, bottom row, reveals some substructures. For SNR $<$ 12 all directions are uniformly distributed having a fraction of 25% each, whereas for higher values, especially between 15 and 20, we have a huge excess of events coming from directions in the first quadrant of 0° to 90° of partly 60% of the total events. Correlation with the angular distribution shown above for different SNR thresholds makes it rather clear that most of this events come from 'Cerro El Diamante'.

As we end up with these results showing the clear and almost pure contribution of noise events for this data set, this section has shown the importance of defining the right windows for the noise and the signal regime.

Closing this section, one can summarize that several approaches for coincident search (beside of direct timing) were applied, but up to now no promising candidate was found.

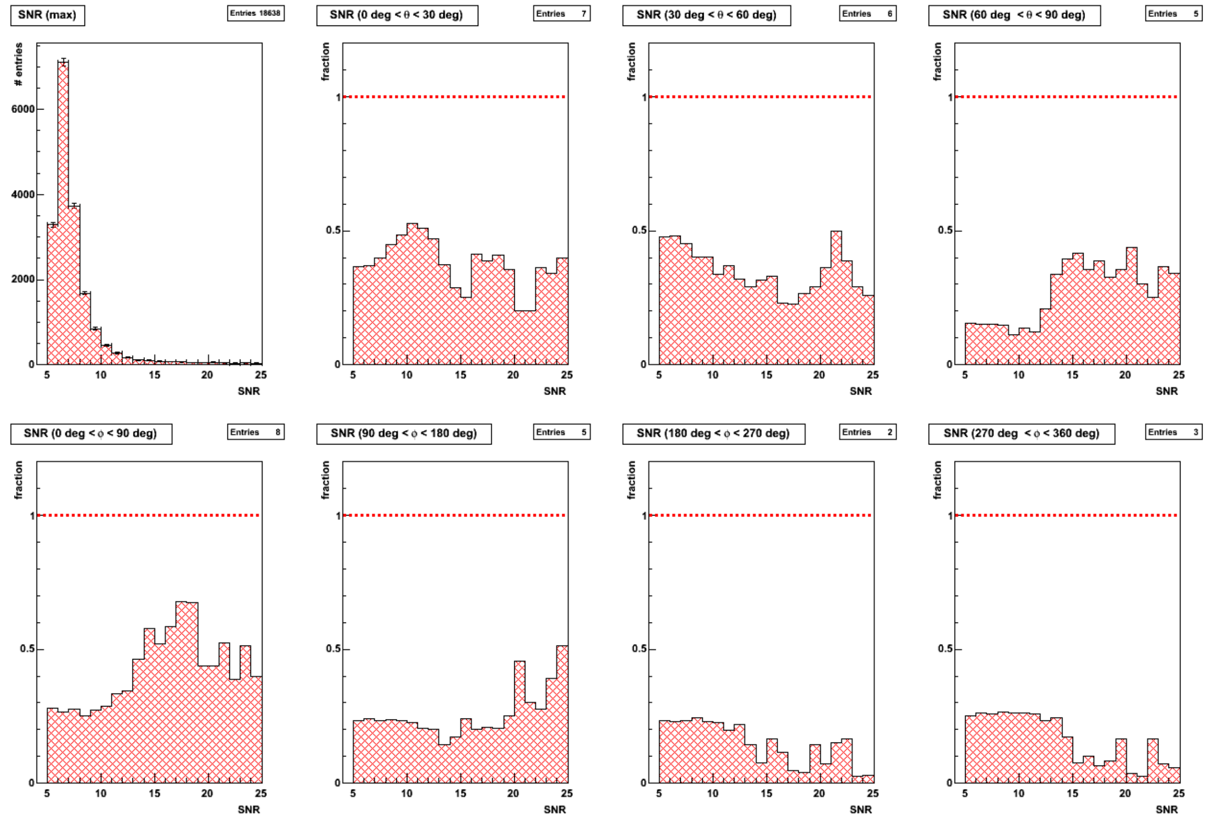

Figure 6.23: Angular dependence of the SNR using a wrong signal window. Top row: All events and three equidistant zenith partitions from 0° to 90° (left to right), bottom row: four equidistant azimuth partitions from 0° to 360°.

This is not surprising as the number of expected coincidences is on the order of a few events per month and the statistic of the completed reconstructions is low. Additionally, the data taken with BLS setup is not of rather high quality as we saw e.g. in the timing accuracy. Nevertheless the analysis in this field will be ongoing.

6.3 First analysis of AERA data

We mentioned before that the first antennas of AERA were deployed in summer/fall 2010 and data taking started in October 2010. Several runs have already been done using these 20 antennas and supplying some first data for checking the setup and the analysis pipeline. As we can easily apply the steps done for the analysis above to this new data, we will show the results of some basic checks here, which are done for parts of run 1408 in November 2010, which were reconstructed with SNR ≥ 3 to get all events (in fact this value is even below the online trigger threshold). In the following we use a sample of 3516 reconstructed events.

We know that the timing accuracy is very important, so we have our first look at the distribution of the GPS-Nanoseconds in Fig. 6.24, left side. We see a huge peak at the lower border of the plot and a rather uniform distribution in the rest of the second half of the time domain. The peak can mostly be adressed to the random trigger data taken at a fixed frequency in parallel to the self-triggering. Therefore, these events should be excluded from analysis as they should contain only noise. But there are additional events which contribute to that peak. The reason for those and the absence of entries in the lower time domain is not clear up to now. Removing them from the data sample reduces the number of events to 473. Nevertheless the remaining part looks quite promising to be real (but not necessarily CR-) events as shown in the distribution of the peak amplitude position in the time trace in Fig. 6.24, right side. For AERA the signal is expected to be somewhere in between the first 500 - 3500 ns. We see a dense distribution of the peak positions at 1500 ns with only single outliers. Considering the same data without the time cut mentioned above the outer regions of the plot are more populated (not shown here).

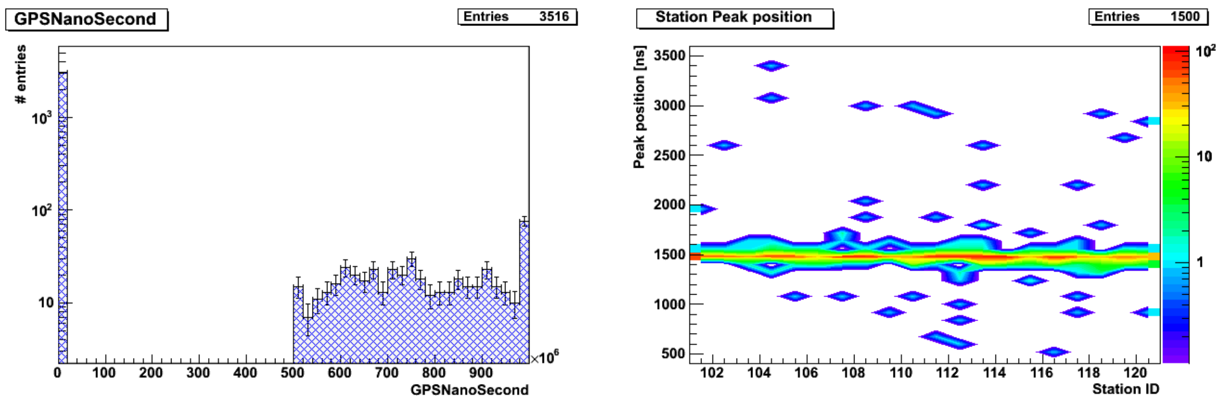

Figure 6.24: Distribution of the GPSCoreNanoSecond for all events (left) and amplitude peak position after the time cut (right).

As we now emanate from real events remaining in the data set we start with the investigation of the pulse parameters. Figure 6.25, left side, shows the two dimensional distribution of the amplitude and the noise. We see a really dense core at amplitudes of about $160 - 200\,\mu$V/m and a corresponding noise of $10 - 20\,\mu$V/m. Several outliers with higher amplitudes are located in a band from $40 - 60\mu$V/m in the noise regime, above these values we have almost no contribution. Unfortunately also the area of high amplitudes and low noise is not populated at all, which would be the region where one would expect CR events. The resulting SNR distribution is shown in Fig. 6.25, right side, and can be fitted with a Gaussian leading to a mean value $\overline{\mathrm{SNR}} = 14.8 \pm 0.6$ and a $\sigma_{\mathrm{SNR}} = 7.6 \pm 0.7$. So for upcoming analysis one should be able to increase the SNR threshold to values of about

7-8 without losing (too much) CR event candidates, which will reduce the time needed for reconstruction.

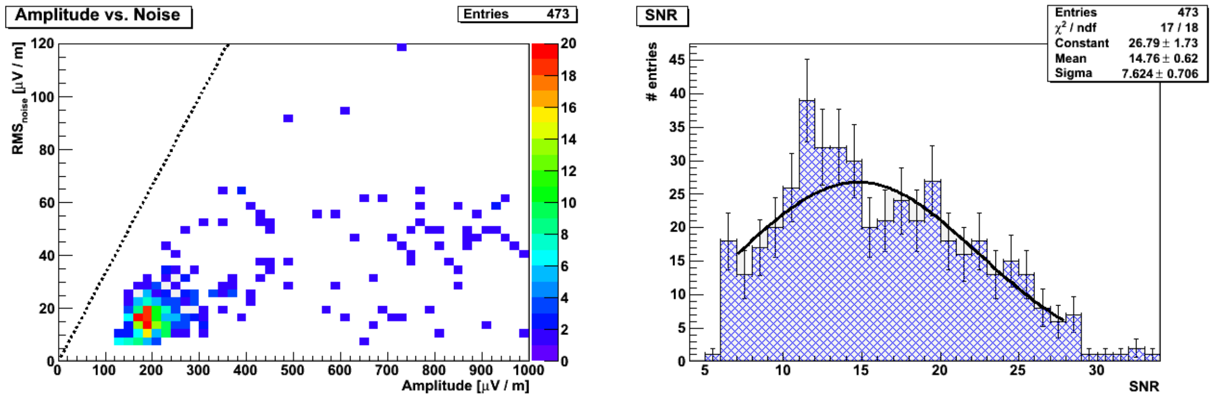

Figure 6.25: Two dimensional distribution of amplitude and noise (left) and resulting SNR (right).

In the analysis of the BLS setup data we saw that the reconstruction accuracy is heavily influenced by the uniformity of the input from the different antennas (which seemed not to be the case there). Therefore, we need to check the distribution of amplitude and noise for the different antennas. The results given in Fig. 6.26 show the consistent calibration for all detectors in the array, so the results gained from these parameters should be much more reliable than before. Looking a little more in detail one might see a slight drift to lower values for higher station IDs, but this has to be checked again with larger statistics.

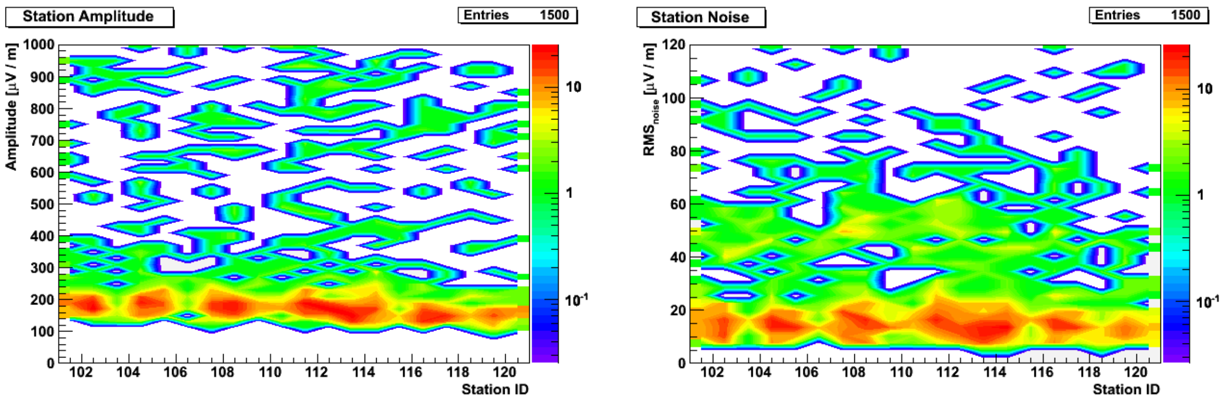

Figure 6.26: Amplitude (left) and noise (right) spectrum for the different detector stations.

Being sure about the quality of our reconstructed data we can finally have a look at the angular distribution of the arrival directions for different SNR thresholds. Figure 6.27, top left, shows the distribution for SNR > 5, containing all events. We see a huge excess for inclined events coming from the north-west at roughly 140° azimuth, which is dominant for all SNR intervals, but gets fainter for higher thresholds. The origin of these pulses is supposed to be the radio station of the police department in 'El Sosneado'.

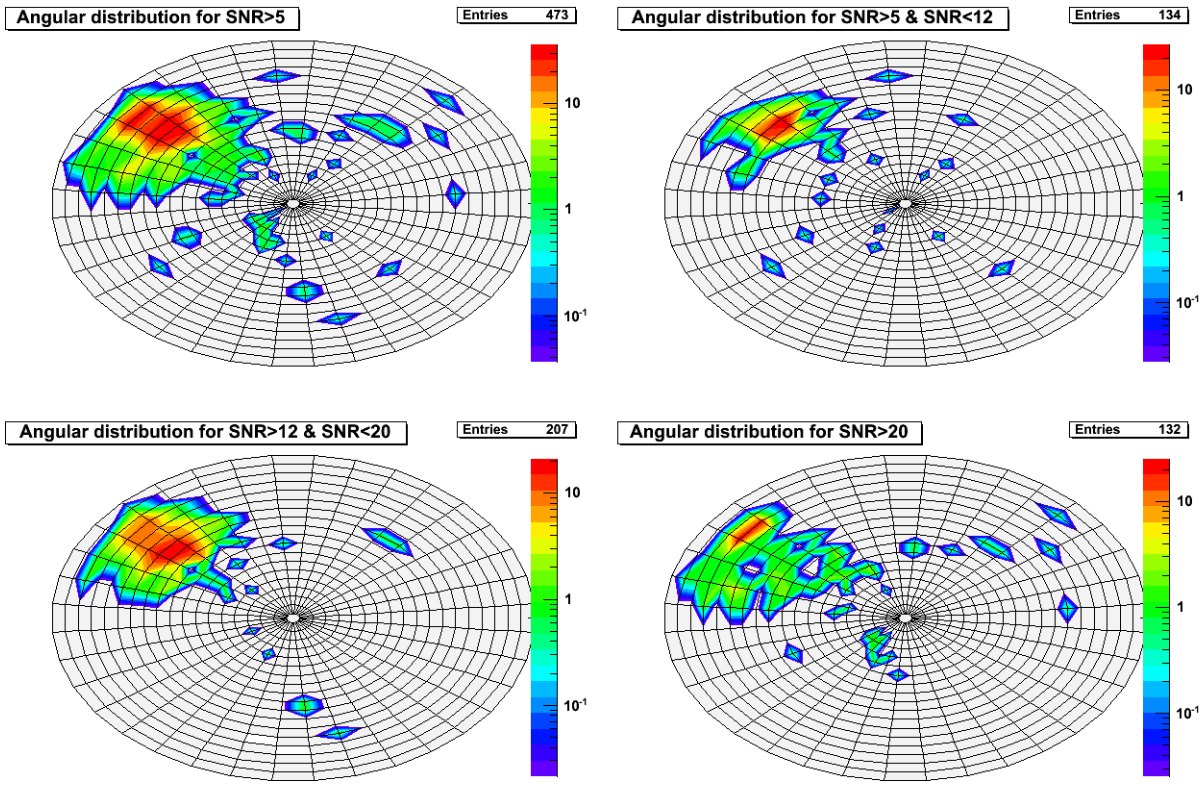

Figure 6.27: Two dimensional angular distribution of reconstructed events with different SNR thresholds: SNR $>$ 5 (top left), 5 $>$ SNR $>$ 12 (top right), 12 $>$ SNR $>$ 20 (bottom left) and SNR $>$ 20 (right). East to the right, north to the top, zenith in the center.

For the highest SNRs we also get several events with low zenith angles, which are of course prominent candidates for CR events. When cutting on SNR > 20, $\theta < 40°$ and using the time cut from above we end up with a list of 17 „golden“ events. Unfortunately, none of them has more than 3 triggered stations, so the angular reconstruction is impossible. Figure 6.28 shows event 11775 of run 1408 in the EventBrowser, which was selected as it has the best discrimination of all golden ones with a SNR = 93.6. We see the typical bipolar pulse in the trace frame at the bottom with an amplitude of about 100 μV/m for both polarizations, so this is really a promising candidate to be a real CR event. Using the reconstructed data (mostly done by M. Melissas, KIT) a coincidence search with SD events in the Infill area was done using the above described algorithms. Up to now no coincident event was found, but the probability naturally increases with larger exposure and therefore the whole procedure will be used for further analysis and (re-)search purposes.

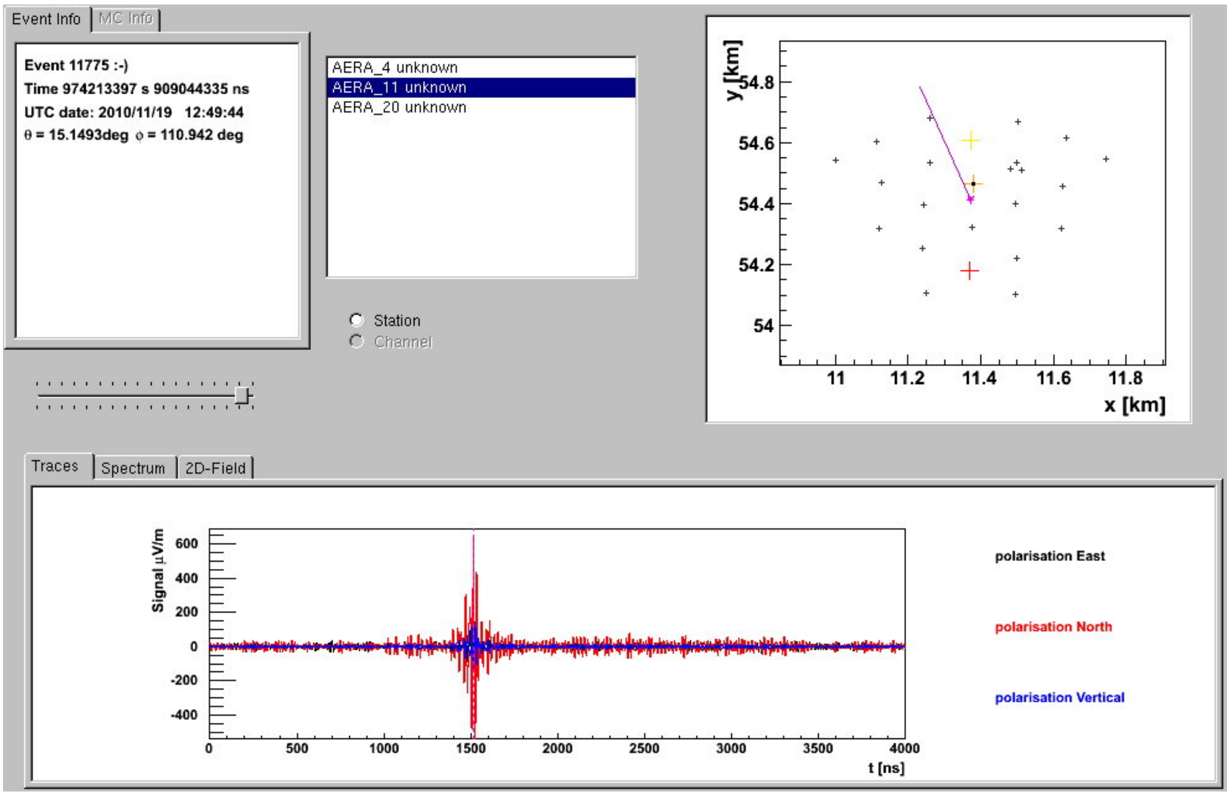

Figure 6.28: Golden AERA event with the highest SNR in the EventBrowser.

Chapter 7

Conclusion and Outlook

This thesis covered several topics concerning with the measurement of radio emission of extensive air showers at the Pierre Auger Observatory. We have investigated data taken by a radio test setup which was located close to the additional deployed surface detector 'Olaia' and improved the Offline code for reconstruction of SD events in this specific region as well as some first results from the actually build Auger Engineering Radio Array.

The aim of the first part of this thesis was to show, that we can gain a lot of statistics in the SD reconstruction through code modification to include 'Olaia' in the normal algorithm. We presented the results of comparing the improved SD-Olaia with the standard SD reconstruction and saw that we can increase the number of successfully reconstructed events by roughly a factor 4. The efficiency for showers to be only reconstructed with SD-Olaia increases for lower energies and small distances between shower core and 'Olaia', whereas the directional accuracy stays at the same level as for SD. Comparing SD-Olaia with the CDAS Herald reconstruction we see that both methods are compatible except a shift in the energy of about 17%. But as this holds only including events below 3 EeV, which is e.g. the threshold for the Auger correlation paper, we also see the robustness and independence of the correlation signal of the applied reconstruction. We compared the results of SD and SD-Olaia for a specific sample of events which have been recorded in coincidence with the radio test setup. We saw that SD-Olaia can reconstruct all 494 events, whereas SD only yields 30% of the sample, while the angular residual is still at the order of $1°$. The efficiencies for energy and distance to the shower core show the same behaviour as for the complete data set. Following we compared the RD to the SD measurement for an increasing selection threshold on the RD-SNR. We saw that the efficiency for the reconstruction of the radio events drops with the distance of the shower core to the antennas and slightly increases with the energy as expected. Finally, we showed that the angular residual between the SD-Olaia and the RD reconstruction is of the order of $10°$ which certainly will be improved for AERA, but is already a quite good result for this limited test setup.

The second part was dedicated to the analysis of the stand-alone radio data of the subsequent test setup and coincidence search. We saw that we have a lot of triggers occuring with a frequency of 50 Hz when using the whole sample without reconstruction. These events can be attributed to a close-by power line even though no phase information could be found in the data. Reconstruction with SNR ≥ 5 we still have clear evidence for 50 Hz. Unfortunately we could not find any candidate source from the directional mapping of these events even using different SNR intervals, so the analysis on this part is still ongoing. Studying the amplitude and noise distributions of the sample we saw a significant difference for the three individual antennas which might be adressed to some technical / calibration problems. Combining both quantities to the SNR we found, that the resulting distribution can be fitted by a Landau function very well, which yields a most probable value of SNR ≈ 25 and a $\sigma_{SNR} \approx 7.5$. Therefore we conclude that for further, more qualitative studies one can increase the SNR threshold to higher values without losing relevant information. Looking at the angular distribution of the reconstructed events we saw a huge access for inclined showers coming from south-west respectively north-east. Both directions are most likely due to located sources of noise and events coming from the north-east can be perfectly aligned with a nearby antenna station. The search for coincident events with the surface detectors was not successful so far, which is not surprising as the expected rate for the considered area is a few events per month. Several approaches to identify coincidences even for wrong timing informations were introduced, which are used for ongoing search. In a last step the influence of the window selection for the signal and noise calculations was discussed, which showed the constant presence of the 50 Hz events if a wrong signal window is selected. As an outlook we presented some first results of AERA using the analysis mentioned above and showed a first candidate for a cosmic ray event.

To summarize, an improved reconstruction for the surface detectors was developed successfully, which is compatible with the existing ones in accuracy, but increases the statistics significantly. This reconstruction method and the experience and knowledge gained from the analysis of the data of the radio test setup will be used for further analysis of the upcoming data from AERA and the search for coincident events with the surface detectors as the combination of both measurements will hopefully lead to a deeper understanding of radio emission from cosmic ray induced air showers and the cosmic rays in general.

Appendix A

Changes in SdEventSelector

Parts of the code added in the the SdEventSelectorOG module in the Auger Analysis Framework Offline (not submitted to svn repository):

Get station ID list from xml-card:

```
topB.GetChild("TankSelection").GetData(fTankSelection);
```

Parameters for reconstruction:

```
case 3:

  INFO("Tank selection mode.");

  kLightningThreshold = 1000;
  kLightningHysteresis = 4;

  kLightCompatibilityTolerance = 200*nanosecond;

  kC1MinDistance   = 500*meter;
  kC1MaxDistance   = 1200*meter;
  kSkewMaxDistance = 1600*meter;

  kSeedTimeDelayEarly = -1000*nanosecond;
  kSeedTimeDelayLate  =  2000*nanosecond;

  kLonelyIfNoneInDistance = 1800*meter;
  kLonelyIfOneInDistance  = 5000*meter;
  break;
```

Station selection algorithm

```
if (fArrayMode == 3 || fArrayMode == 0 || fArrayMode == 1) {
  vector<int>::iterator its=fTankSelection.begin();
  if (*its != 0) {
    int select = 0;
    const SEvent::CandidateStationIterator sEnde = sEvent.CandidateStationsEnd();
    for (SEvent::CandidateStationIterator sCand = sEvent.CandidateStationsBegin();
             sCand != sEnde; ++sCand) {
      int cand = sCand->GetId();
      for (vector<int>::iterator it=fTankSelection.begin();
               it < fTankSelection.end(); ++it) {
        if (sEvent.HasStation(*it) && cand == *it) {
          select++;
        }
      }
    }

    if (select !=0) {
      ostringstream yesid;
      if (select == 1)
        yesid << select << " requested station takes part in this event.";
        if (select > 1)
        yesid << select << " requested stations take part in this event.";
        INFO(yesid);
    }

    if (select == 0) {
      ostringstream noid;
        noid << "None of the requested stations takes part in this event";
        INFO(noid);
        return eContinueLoop;
    }
  }
}
```

Bibliography

[AB09] ALLEKOTTE, I. and X. BERTOU: *Acceptance of generalized Surface Detector Arrays from real data.* GAP 2009-155, 2009.

[AER09] AERA: *Proposal for the construction of the 20 km^2 Auger Engineering Radio Array.* GAP 2009-172, 2009.

[Anc04] ANCHORDOQUI, L.: *The Pierre Auger Observatory: Science Prospects and Performance at First Light.* Proceedings of PASCOS 2004, 2004.

[Asc08] ASCH, T.: *Simulation of an array of antenna detectors.* GAP 2008-177, 2008.

[Ask62] ASKARYAN, G. A.: *Coherent Radio Emmission from Cosmic Showers in Air and in Dense Media.* JETP 14, 441, 1962.

[Aug39] AUGER, P.: *Extensive cosmic-ray showers.* Rev. Mod. Phys. 11, 288-291, 1939.

[Ber04] BEREZINSKY, V.: *Propagation and signatures of Ultra High Energy Cosmic Rays.* Nuclear Physics B Proceedings Supplements 136, 147-158, 2004.

[Bir93] BIRD, D. J.: *Evidence for correlated changes in the spectrum and compostition of cosmic rays at extremeyl high energies.* Phys. Rev. Lett. 71, 3401-3404, 1993.

[BM09] BAULEO, P. and J. R. MARTINO: *The dawn of the particle astronomy era in ultra-high energy cosmic rays.* Nature 458 847-851, 2009.

[BO78] BLANDFORD, R. and J. OSTRIKER: *Particle acceleration by astrophysical shocks.* Astrophys. J. 221, L29-L32, 1978.

[CSG97] CRONIN, J., P. SWORDY and T. GAISSER: *Cosmic rays at the energy frontier.* Sci. Am. 276 32-37, 1997.

[Dal10] DALLIER, R.: *Radio spectrum measurements at Auger, Part 2.* GAP 2010-032, 2010.

[EFG10] Erdmann, M., S. Fliescher and C. Glaser: *Measurement of the lateral distribution function of radio emission from ultra high energy cosmiy ray induced air showers.* GAP 22010-119, 2010.

[EFW09] Etchegoyen, A., U. Fröhlich and B. Wundheiler: *The Pierre Auger Project and Enhancements.* Latin American Symposium on Nuclear Physics and Applications, 2009.

[Erd10] Erdmann, M.: *Antenna alignment for the first 24 stations of AERA.* GAP 2010-083, 2010.

[Fer49] Fermi, E.: *On the Origin of Cosmic Radiation.* Physics Review 75, 1169-1174, 1949.

[FH05] Falcke, H. and T. Huege: *Radio emission from cosmic ray air showers: simulation results and parametrization.* Astropart.Phys. 24, 116-136, 2005.

[Gai90] Gaisser, T. K.: *Cosmic rays and particle physics.* Cambridge University Press, 1990.

[GF03] Gorham, P. and H. Falcke: *Detecting Radio Emission from Cosmic Ray Air Showers and Neutrinos with a Digital Radio Telescope.* Astropart.Phys. 19, 477-494, 2003.

[GH77] Gaisser, T. K. and A. M. Hillas: *Proceedings of the 15th ICRC, pp.353.* 1977.

[Gre66] Greisen, K.: *End to the cosmic-ray spectrum.* Physical Review Letters 16, Nr. 17, 748-750, 1966.

[GS05] Gaisser, T. and T. Stanev: *High-energy cosmic rays.* Nucl. Phys. A Vol. 777 98-110, 2005.

[HAB05] H.Falcke, W. Apel and A. Badea: *Detection and imaging of atmospheric radio flashes from cosmic ray air showers.* Nature 435 313-316, 2005.

[Hau09] Haungs, A.: *Air Shower Measurements with the LOPES Radio Antenna Array.* Nucl. Instrum. Meth. Suppl. A 604, 1-8, 2009.

[Hei44] Heitler, W.: *Quantum theory of radiation.* Oxford University Press, 1944.

[Hes12] Hess, V. F.: *Über Beobachtungen der durchdringenden Strahlung bei sieben Freiballonfahrten.* Physikalische Zeitschrift, 1912.

[HUE07] HUEGE, T., R. ULRICH and R. ENGEL: *REAS2: CORSIKA-based Monte Carlo simulations of geosynchrotron radio emission.* Proceedings of the 30th ICRC, 2007.

[Hue10] HUEGE, T.: *An update on the physics of MHz radio emission.* Auger Collaboration Meeting, Malargue, Session: Radio Physics Results, 2010.

[Jel65] JELLEY, J. V.: *Radio pulses from extensive cosmic-ray air showers.* Nature 205, 327, 1965.

[Kam07] KAMPERT, K.-H.: *Cosmic rays from the knee to the ankle.* Nucl. Phys. Proc. Suppl. 165 294-306, 2007.

[KL66] KAHN, F. D. and I. LERCHE: *Proceedings of the Roy. Soc., Vol. A-289, 206.* 1966.

[Krö09] KRÖMER, O.: *Simulation of antennas proposed for radio detection of UHECRs.* GAP 2009-035, 2009.

[Lau09] LAUTRIDO, P.: *Development of a radio-detection method array for the observation of ultra-high energy neutrino induced showers.* Nucl. Instrum. Meth. Suppl. A 604, 85-87, 2009.

[Mel10] MELISSAS, M.: *Private Communication.* 2010.

[Pie01] PIERRE AUGER COLLABORATION: *The Pierre Auger Observatory Technical Design Report*, 2001.

[Pie05] PIERRE AUGER COLLABORATION : EVENT SELECTION GROUP: *The Official Event Selection as of March 2005.* GAP-2005-023, 2005.

[Pie07a] PIERRE AUGER COLLABORATION: *Correlation of the Highest-Energy Cosmic Rays with Nearby Extragalactic Objects.* Science 318, 938-943, 2007.

[Pie07b] PIERRE AUGER COLLABORATION: *The Offline Software Framework of the Pierre Auger Observatory.* Nucl. Instrum. Meth. Suppl. A 580, 1485-1496, 2007.

[Pie10a] PIERRE AUGER COLLABORATION: *http://www.auger.org.ar/CDAS/Herald/*, 2010.

[Pie10b] PIERRE AUGER COLLABORATION: *Update on the correlation of the Highest-Energy Cosmic Rays with Nearby Extragalactic Matter.* Astropart. Phys. 34, 314-326, 2010.

[Pie10c] PIERRE AUGER COLLABORATION: *Update on the correlation of the highest energy cosmic rays with nearby extragalactic matter.* Astropart.Phys. 34, 314-326, 2010.

[Pie10d] PIERRE AUGER COLLABORATION : RADIO OFFLINE GROUP: *The radio extension of Auger Offline.* GAP 2010-056, 2010.

[Pro99] PROTHEROE, R. J.: *Acceleration and Interaction of Ultra High Energy Cosmic Rays.* arXiv:astro-ph/9812955v1, 1999.

[PW65] PENZIAS, A. A. and R. W. WILSON: *A measurement of excess antenna temperature at 4080-Mc/s.* 1965.

[Sch07a] SCHUESSLER, F.: *Comparison of the AGN-correlation signal derived with Herald and Offline reconstructions.* GAP 2007-115, 2007.

[Sch07b] SCHUESSLER, F.: *Investigation of AGN correlation and composition hypotheses with hybrid and stereo FD data.* GAP 2007-094, 2007.

[Sch10] SCHRÖDER, F. G.: *New method for the time calibration of an interferometric radio antenna array.* Nucl. Instrum. Meth. Suppl. A 615, 277-284, 2010.

[Sok04] SOKOLSKY, P.: *Introduction to Ultra-High Energy Cosmic Ray Physics.* Westwood Press, 2004.

[Ste10] STEPHAN, M.: *Design and test of a low noise amplifier for radio antennas measuring atmospheric showers.* GAP 2010-045, 2010.

[SW09] SCHOLTEN, O. and K. WERNER: *Macroscopic Model of Geomagnetic-Radiation from Air Showers.* Nucl. Instrum. Meth. Suppl. A 604, 24-26, 2009.

[SWR08] SCHOLTEN, O., K. WERNER and F. RUSYDI: *A Macroscopic Description of Coherent Geo-Magnetic Radiation from Cosmic Ray Air Showers.* Astropart. Phys. 29 94-103, 2008.

[Tea10] TEACHER'S WEB CERN: *http://teachers.web.cern.ch/teachers/archiv/HST2000/teaching/exp* 2010.

[Ulr06] ULRICH, R.: *Data Summary Trees and Shower Visualization for Reconstructed Auger Events.* GAP-Note 2006-081, 2006.

[Uni10] UNIVERSITY OF NEW HAMPSHIRE, HIGH ENERGY ASTRO PARTICLE GROUP: *www.gro.unh.edu/neutron_monitors/shower.gif*, 2010.

[vdB07] Berg, A. van den: *First detection of radio signals from cosmic rays at the Pierre Auger Observatory.* GAP 2007-065, 2007.

[VR05] Veberic, D. and M. Roth: *Offline Reference Manual : SD Reconstruction.* GAP 2005-035, 2005.

[ZK66] Zatsepin, G. T. and V. A. Kuzmin: *Upper Limit of the Spectrum of Cosmic Rays.* Journal of Experimental and Theoretical Physics Letters 4, 78-80, 1966.

Acknowledgement

First of all I would like to thank Prof. Karl-Heinz Kampert for giving me the possibility to write my thesis in this very interesting topic. Also I would like to thank him for his continuous support and mentoring all the time.

Additionally I want to thank Prof. Klaus Helbing for the willingness to be the second revisor for this work.

A very special „grazie mille“ goes to Dr. Julian Rautenberg. He was the first adress for my frequent appearing daily questions and never got tired answering them or giving me some new food for thoughts. Moreover I want to thank him for proof-reading this thesis and for all the long and fruitful discussions not only concerning this topic, but on everything else in relation with research business, too.

Thanks also to all my colleagues in the Astroparticle Group in Wuppertal for the help offered whenever needed, for the interesting discussions and of course for all the fun we had beside of the daily work.

Furthermore I am very grateful to all the colleagues from the Pierre Auger Collaboration and especially from the AERA group. Representative I would like to mention Maximilien Melissas which was very helpful in the coding business and afterwards in starting the reconstruction of the AERA data.

Last but definitely not least, I want to thank my family, Anna and all my friends. Without your support and encouragement especially in the final stage, this work would have never been possible.

Eidesstattliche Erklärung

Hiermit versichere ich, die vorliegende Arbeit selbstständig und unter ausschließlicher Verwendung der angegebenen Literatur und Hilfsmittel erstellt zu haben.

Die Arbeit wurde bisher in gleicher oder ähnlicher Form keiner anderen Prüfungsbehörde vorgelegt und auch nicht veröffentlicht.

Wuppertal, den ________________ ____________________

Unterschrift